An evaluation of a design method for

MIXED FLOW FANS

Jacques H du Toit

Thesis presented in partial fulfilment of the requirements for

the degree Master of Science in Engineering (Mechanical)

at the University of Stellenbosch

Thesis supervisors:

Prof. T W von Backström

Prof. A H Basson

Department of Mechanical Engineering

University of Stellenbosch

March 2002

DECLARATION

ii

I, Jacques Hendrik du Toit, hereby declare that this thesis is my own original work. It is being submitted for the Degree of Master of Engineering Science (Mechanical) at the University of Stellenbosch. It has not been submitted, in its entirety or in part, for any degree or examination at any other University.

ABSTRACT

Mixed flow fans find application in an operating region between that of axial flow and centrifugal fans. The candidate investigated the working of these mixed flow fans and formulated a design algorithm. The algorithm was based on work done by previous authors, most of which have tried to modify existing axial flow fan design methods to suit the mixed flow case. A fan was designed, built and tested. Tests showed that the fan did not perform as designed, producing a lower pressure rise at a lower flow rate. A five hole probe was used to measure the exit flow vector and the results showed that most of the work was done by the lower half of the blade. Based on this discrepancy between the designed and actual fan performance, a number of changes to the design procedure were recommended. Amongst other things: the use of numerical blade modelling procedures instead of modified cascade correlations and the disregard of the Coriolis work in the design of the blade shape.

OPSOMMING

Gemengde vloei waaiers bevredig die behoefte aan 'n waaier in 'n spesifieke werksgebied waar aksiaal en sentrifugale waaiers minder effektief is. Die projek ondersoek die werking van gemengde vloei waaiers en formuleer 'n ontwerp-algoritme. Die algoritme is gebaseer op bestaande navorsing, waarvan die meeste 'n poging is om aksiaalvloeiwaaiermetodes aan te pas vir die gemengde vloei geval. 'n Waaier is ontwerp, gebou en getoets. Toetsresultate toon dat die waaier 'n laer drukstyging by 'n laer volume vloei gee as wat die ontwerp voorspel. 'n Vyfgat-anemometer is gebruik om die uitlaatvloei-vektor te meet en die resulate het bewys dat die gedeelte van die rotorlem naaste aan die naaf meeste van die werk doen. Hierdie afwyking van die ontwerptoestand is ondersoek en 'n aantal veranderings aan die ontwerp algoritme is voorgestel, naamlik: die gebruik van numeriese lemprofiel simulasie, instede van die glip- en deviasie- modelle, en die ontwerp van die lemprofiel deur die Coriolis werk te ignoreer.

TABLE OF CONTENTS

vi

LIST OF TABLES

LIST OF FIGURES

NOMENCLATURE

A	coefficient used in matrix through flow method formulation	-
	coefficient used in Lewis transformation	-
A'	coefficient used in Du Toit transformation	-
a	half the length of the short axis of a conical section	m
	distance along chord from leading edge to point of maximum camber expressed as fraction of the chord	-
AR	area ratio	-
b	half the length of the long axis of a conical section	m
C	bellmouth coefficient	-
c	blade chord	m
D	diameter	m
e	eccentricity	-
f	Lewis function in prediction of total-to-total efficiency	-
g	gravitation acceleration	m/s^2
h	perpendicular distance from hub to casing	m
	specific enthalpy	J/kg
	height of fluid as an indication of pressure	m
H	pressure in meters of air	m
m	mass	kg
	coefficient used in Howell's correlation	-
$\overset{o}{m}$	mass flow rate	kg/s
P	static pressure	Pa
P_0	total or stagnation pressure	Pa
P_a	atmospheric pressure	Pa
P_{ft}	fan total pressure	Pa

Q	flow rate	m^3/s
R	nose radius of the MCA blade profile	m
r	radius – measured from rotational axis	m
	inverse of λ	m
R	ideal gas constant	J/kg.K
	outer radius of a radial cascade	m
Re	Reynolds number	-
RR	radius ratio	-
S	source term used in matrix through flow method formulation	-
s	specific entropy	J/kg.K
T	temperature	°C
t	maximum thickness of blade section	m
	blade spacing in a rectangular cascade	m
U	tangential velocity	m/s
V	absolute velocity	m/s
V'	ideal absolute velocity	m/s
V_m	meridional component of absolute velocity	m/s
V_r	radial component of absolute velocity	m/s
V_s	slip velocity	m/s
V_u	tangential component of absolute velocity	m/s
V_u'	ideal tangential component of absolute velocity	m/s
$V_{u,slip}$	tangential component of absolute velocity after slip	m/s
W	relative velocity	m/s
	work rate (power)	J/s
W'	ideal relative velocity	m/s
W_u	tangential component of relative velocity	m/s

$\overline{W}$	specific work	J/kg
x	real component of the complex number describing the conical plane	m
y	imaginary component of the complex number describing the conical plane	m
Z	number of blades	-
z	complex number describing the conical plane	m

Greek symbols

Γ	blade circulation	m²/s
α	absolute flow angle relative to axial direction	°
	non-dimensional inlet efficiency of a bellmouth inlet	-
	sweep angle used in conformal transformation	°
β	relative flow angle relative to axial direction	°
β_m	vector mean relative flow angle	°
δ	angle used in Lewis transformation	°
Δ	angle used in Lewis transformation	°
δ'	angle used in Du Toit transformation	°
Δ'	angle used in Du Toit transformation	°
ϕ	yaw angle of the five hole probe	°
	flow coefficient	-
	sweep angle	°
θ	pitch angle of the five hole probe	°
	blade camber	°
ρ	density	kg/m³
σ	slip factor	-
ω	rotational speed	rad/s
ψ	streamfunction value	kg/m.s

xiv

	head coefficient	-
φ	yaw angle	°
υ	pitch angle	°
δ	deviation	°
	the angle at which a plane cuts a cone	°
λ	parameter used in conformal transformation	m^{-1}
η	imaginary component of the complex number describing the rectangular plane	m
ξ	real component of the complex number describing the rectangular plane	m
	stagger angle	°
ζ	complex number describing the rectangular plane	m
	rotor loss coefficient	-
γ	cone angle	°
	ratio of specific heats of a gas	-
ω	rotational speed	rad/s
X	angle the blade makes with line vertical to meridional direction	°

Subscripts

1	flow property at inlet
2	flow property at exit
B	Busemann
S	Stodola
St	Stanitz
N	north node
S	south node

W   west node

E   east node

P   centre node

Frequently used abbreviations

2D   two-dimensional

3D   three-dimensional

FEM   **Finite Element Method**

MCA   **Multiple Circular Arc**

MFF   **Mixed Flow Fan**

MTFM   **Matrix Through Flow Method**

SCM   **Streamline Curvature Method**

CHAPTER 1

INTRODUCTION

" The mixed flow compressor is rarely used, probably because of the limited experience and data existing for it, although it would seem to have a very natural niche. "

- N A Cumpsty

Many everyday engineering applications require a gas to be supplied at a particular flow rate and pressure. The gas must have enough energy to move at this specified rate and overcome the resistance of the system that contains it. This requires that, somewhere in the system, work must be done on the gas to overcome the losses associated with this resistance. The machines used to do this work in high- and low-pressure applications are classified as compressors and fans respectively. Both are part of the turbomachinery family. Each system containing such a turbomachine, whether it has a high- or low-pressure requirement, has a unique combination of flow rate and resistance and therefore calls for a specific turbomachine to satisfy this requirement. Although there may be countless compressors and fans, each geared for a certain application, they are usually classified as centrifugal (radial) or axial in reference to the average meridional flow direction. In general, industry uses centrifugal turbomachines for the high load (high resistance), low capacity (low flow) applications and axial flow turbomachines for the converse.

Despite the fact that they are designed for different duties, axial and radial machines often compete for the same application, especially in the aircraft industry. Radial machines are able to satisfy pressure requirements with a single stage, but have the disadvantage of a large exit diameter and radial exit flow. Axial flow machines, on the other hand, have similar inlet and exit diameters, but at increased cost due to the higher number of stages needed to satisfy the same pressure requirements as the corresponding radial machine. It follows that the radial component imparted to the flow in centrifugal machines has a great advantage in terms of performance, but at some geometrical disadvantage. The logical solution is a machine that has some of the through flow properties of the axial flow fan with a radial component in the flow to increase its ability to deliver pressure rise.

Figure 1.1 illustrates the different operating ranges for fans using a Cordier (Lewis, 1996) diagram. Pressure rise (the ability to overcome flow resistance) is plotted as a function of flow

rate for optimal fan performance on a non-dimensional set of axes. As discussed, somewhere between the two operating ranges of the centrifugal and axial fans there is an area where neither of these two types of fans works optimally. A third type of fan is needed that would be able to supply a fairly high volume flow and overcome reasonably high resistance. This type of fan is called a mixed flow fan (MFF). Figure 1.1 confirms that this is indeed the case.
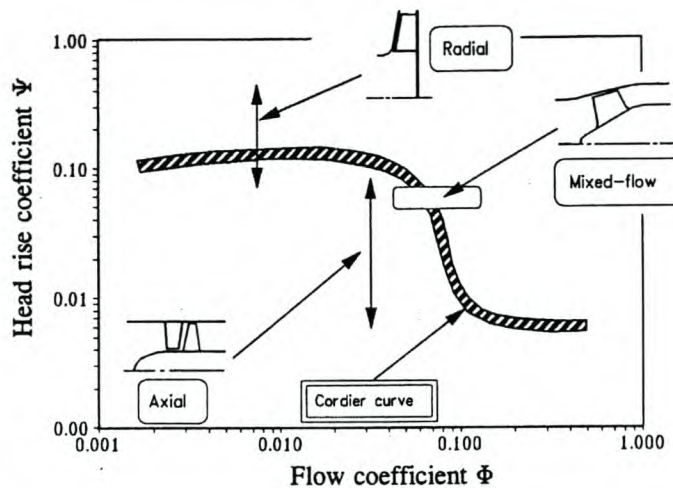
Figure 1.1: Cordier diagram for fans (Lewis, 1996)

Whitfield et al (1990) describes a mixed flow rotor as one in which the inlet flow is not solely in the radial direction, but is inclined to the axis so that the flow entering the rotor has an axial as well as a radial component. Myles (1965) gives a more general definition by defining the mixed flow principle as the one in which the impeller blades are developed along conical or spherical surfaces. This geometry provides this type of turbomachine with its unique ability to satisfy the need for high loads and reasonable air handling capacity. As the name and the operating range indicate, the MFF is a hybrid of the axial and radial machines.

Not only is there a need for a hybrid machine that can operate where radial and axial flow machines do not work well, but the mixing of the two work producing mechanisms seems to be a way of attaining a more efficient machine. This has made it suitable for applications in fields such as gas-cooled nuclear reactors, hovercraft lift fans and locally designed military vehicles such as the *Ratel*. From a academic point of view, if it is possible to fully understand mixed flow fans and develop a comprehensive, accurate method to design them, then surely axial and radial flow fans are just special cases of the same generic turbomachine.

McEwen et al. (1987) designed a mixed flow fan for the National Engineering Laboratory (NEL) because a suitable one could not be found in industry. They ascribed this shortage to

the difficulty of both designing and manufacturing this type of turbomachine. It would seem that the fact that the flow has an important component in the radial direction prevents the designer from making several of the simplifying assumptions usually made in axial flow fan design.

Scope of thesis

The Department of Mechanical Engineering at the University of Stellenbosch has successfully developed axial flow fans and the move to the mixed flow regime is a logical step. Fans of this type are being designed and built commercially around the world, but unfortunately the methods used are not available to outsiders. The main objective of this thesis is to understand the fluid dynamic working of MFFs.

The specific objectives of this thesis are:

➤ to review mixed flow fan design methods;

➤ to investigate one design method in detail;

➤ to derive an algorithm that implements this method;

➤ to design a prototype fan with a coded version of this algorithm;

➤ to build a prototype fan;

➤ to test the performance of the fan and compare the results with the design parameters;

➤ to evaluate the design method based on these experimental findings;

➤ to make recommendations regarding the usefulness of the design method or the investigation of alternative methods.

CHAPTER 2

LITERATURE REVIEW

"However, there still exist some doubts and weaknesses in estimating the appropriate slip factors and the use of stationary cascade data or correlations for evaluating losses, particularly at low flow rates, which initiate errors in the prediction scheme. "

- S Sarkar

The author undertook an extensive search, in the library and on the Internet, for literature around the subject of mixed flow fan design. Unfortunately there are very few publications on the mixed flow fans per se (even less on the design thereof) and consequently information on fringe topics makes up the bulk of this literature review.

2.1 A brief history of fan technology

In the years following the success of the Wright brothers, much effort was put into airplane design to meet the growing military and, to some extent, commercial needs. One of the aspects that was given special attention by men such as Betz, Prantl and Glauert, was propeller design. Van Niekerk (1964) ascribes the advance of fan design techniques to development done on these propellers and also the work done by Keller (1937) on ducted fans. Early methods made use of the well-known Euler expression, but did not contain information on blade loading. According to Myles (1965) this led to inadequate loss estimation and subsequent non-optimum designs.

Mixed flow pumps designed before 1965 were developed by using one of two methods: the aforementioned one dimensional Euler method with suitable slip correlation or by modifying existing designs through careful observation. It was only with the introduction of lift and drag concepts that real progress was made especially in axial flow and later mixed flow fan designs.

These methods are outdated and mostly obsolete and have made way for two groups of modern methods. The first group is based on the method originally developed by Myles (1965) which incorporates modified cascade data; the second group is numerical simulation as developed by among others Zangeneh (1991), Takemura et al. (1996) and Goto et al. (1996).

2.2   Cascade methods

The design of all types of fans is based on the principle that work is done through a change in angular momentum of the gas as it passes through the rotor. The relationship between the change in gas flow vector and the work done, is described by the so-called Euler turbomachinery equation, which is derived in for example Cumpsty (1989). See also section 3.2.1 and Appendix F. In the analysis problem, it is possible in most cases to find the work done, based on the geometry of the machine irrespective of the annulus shape. The design problem, however, poses a challenge. For axial flow fans, where the streamtube radius does not change significantly from inlet to exit and the annulus stays parallel to the axial direction, the design has been well documented. Wallis (1983), Horlock (1978), Cohen et al. (1987), Cumpsty (1989) are examples of well-known books on the design of these axial flow machines. In fact, the problem is mostly two-dimensional (2D). Van der Spuy (1997) notes that Wallis (1983) and Bruneau (1994) considered each blade section as a 2D aerofoil section, neglecting the aerodynamic influence that sections at other radii may have. However, when the annulus is not parallel to the axial direction, the blade design is fully 3D and radial equilibrium has to be taken into account.

Smith (1987) proposes a design method for axial flow fans, which he tries to adapt for the mixed flow case. He mentions the radial shift in streamlines and states that actuator disc theory is not relevant. The author of the publication does not qualify why actuator disc theory is not relevant and probably avoids the issue because it is more difficult to implement than in the axial flow fan case. In order to adapt the axial flow fan design method for the mixed flow case, Smith (1987) had to transform the 2D cascade data to a conical surface. The paper states that, due to the transformation of the 2D cascade to a conical surface, negative camber may occur which negates the use of lift and drag coefficients and the calculation of losses as done in axial flow fans. The paper is not comprehensive and gives no clear design methodology.

In 1965 Myles produced a report for the National Engineering Laboratory (N.E.L.) in which he proposes a method to design mixed flow fans. His method is based on the axial flow design methods of that time; starting with the required duty of the fan, the flow vectors into and out of the rotor are determined, deviation from the blade is calculated and the relevant profiles are chosen. These profiles are then transformed, in general, onto a spherical surface. Deviation of the airflow angles from the blade angles (i.e. ideal vs. real flow) is seen as a combination of slip and the classical deviation found in high solidity compressor cascades.

Saha et al. (1995) designed a mixed flow pump using the method similar to the one presented by Myles (1965) in order to investigate experimentally the 3D characteristics of the flow through the pump. A parallel casing was used with a semi-cone angle of 30°. Blade angles were calculated using the correlations of Stodola (1927) and Lieblein (1960) for the slip and deviation respectively, two-dimensional cascades were selected and a transformation was made to the relevant conical surface. Saha et al. (1995) specifically considered the effect of varying tip clearance on the performance of the pump with specific reference to the change in pressure rise, pitch and yaw angles and losses. It is notable that Saha et al. (1995) also divided the Euler equation into two parts: a Coriolis work term and a blade action work term.

Sarkar (1992) followed a similar approach. He designed a mixed flow impeller with a high specific speed and set out to illustrate a method to analyse the machine and predict its performance. In order to do this, he stayed close to axial flow theory and modified the parameters to take the inclined geometry into account. These expressions were derived in such a way that they reduce to the familiar axial flow theory in the case of a radius ratio of one. The results of the analysis show good correlation with experimental results around the design point, but over-predict the performance at lower flow rates.

2.3   Numerical analysis

At some stage in the design a numerical method has to be used. The first option is a full 3D CFD approach to the problem. Denton (1987), Moore et al. (1987) etc. have written useful codes for turbomachines, but Takemura et al. (1996) believe that their accuracy has still not been verified in enough detail. Even the work done on numerical codes for centrifugal and mixed flow machines by Eckhart (1976) and others has the shortcoming that they were developed for single rotor applications. Takemura (1996) therefore developed a 3D time-averaged numerical code that solved the internal flow of a mixed flow impeller and diffuser combination. The numerical method agreed fairly well with experimental results and it was shown that the modelling of the diffuser-rotor combination gives far superior answers than just modelling the rotor in isolation. An interesting phenomenon was identified, namely that at lower than design mass flows, recirculation flows at the diffuser inlet sometimes interact with the trailing edge of the rotor at the shroud.

All the aforementioned work used the direct approach where a blade geometry was chosen and the resulting flow calculated. Zangeneh (1991) approached the problem from a different perspective (the inverse method) by specifying the flow distribution and computing the

subsequent blade geometry iteratively. In the direct method, the designer has to modify the blade geometry until the required flow is achieved. It is often difficult to know by just how much to change which parameters to attain the desired effect. The indirect method thus has the advantage that the designer can start off with the problem and work toward the solution instead of other way around. Zangeneh et al. (1996) later used this 3D inverse design method to design a mixed flow pump impeller with suppressed secondary flows. Unfortunately the method is complex and computer intensive.

A second approach would be to supplement the conventional design method for mixed flow fans, as described by Myles (1965), with a numerical method that would solve for the meridional flow, based on the assumption that the flow is both inviscid and incompressible. The technique would further simplify the analysis by not modelling the geometry of the blades, but simply simulating their effect by means of a whirl (rV_θ) source.

2.4   Performance of mixed flow impellers

2.4.1   Head flow characteristics

Although mixed flow rotors are similar to their axial and radial flow counterparts, they have certain unique aspects that are worth mentioning. The first is the head vs. flow (when pumping liquids) or pressure vs. flow (when pumping gases) characteristic. Many authors prefer to express head, flow and pressure rise in terms of head, flow and pressure coefficient as shown in table 2.1.

Head coefficient	$\dfrac{gH}{N^2D^2}$
Pressure coefficient	$\dfrac{\Delta p}{\frac{1}{2}\rho V^2}$
Flow coefficient	$\dfrac{Q}{ND^3}$

Table 2.1: Summary of non-dimensional flow characteristic parameters

The performance curve of axial flow rotors tend to rise with a decrease in flow rate up to a point where the angle of attack of the blade section becomes too severe and the blades stall. This causes a drop in performance and can be seen as a dip in the performance curve. The pump designed by Saha et al. (1995) shows a steady rise in the head characteristics as the

flow is throttled and seems stable with no discernible loss in pressure rise at lower values of volume flow rate. See figure 2.1.
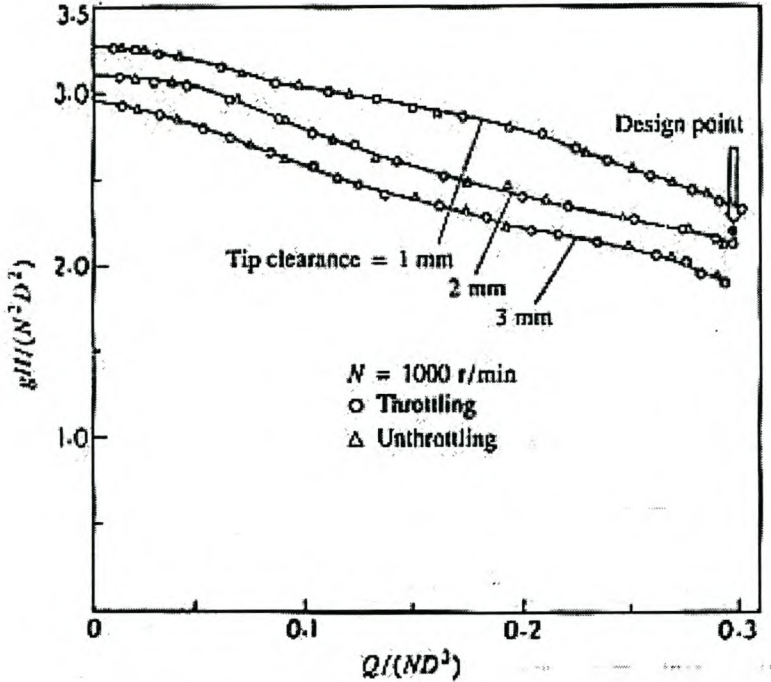
Figure 2.1: Head-flow characteristics for a mixed flow pump with varying tip clearance.
(Saha et al, 1995)

It would appear that that the pump does not stall as one would expect with axial flow machines, but the stable nature of these curves is not necessarily inherent to mixed flow designs. Myles (1965) illustrates this by comparing two machines (figure 2.2) that are designed for the same duty and speed, with only the radius ratio (refer to Appendix E for a definition) varying. The first rotor, corresponding to the lower radius ratio, shows a steady increase in head as the flow is throttled with no indication of stall, where the second rotor, corresponding to the higher radius ratio, does stall at low flow rates.

2.5
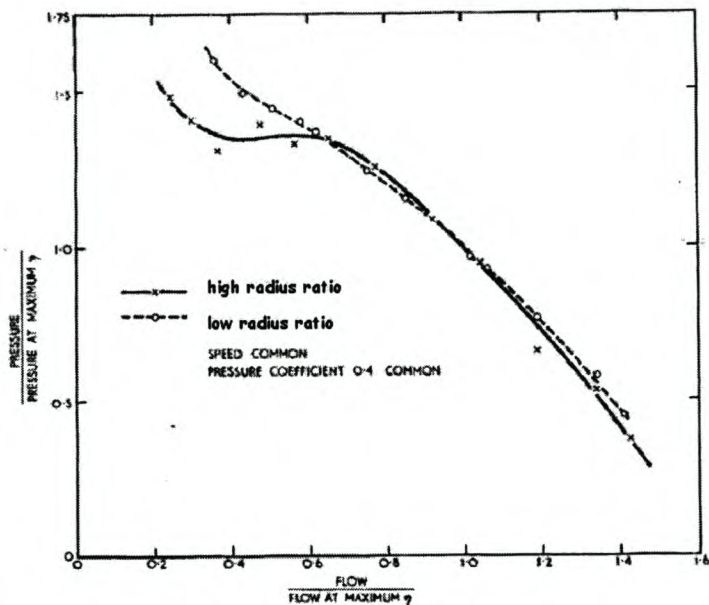
**Figure 2.2: Head-flow characteristics for a mixed flow pump with varying radius ratio.
(Myles, 1965)**

2.4.2   Tip clearance

According to Cumpsty (1989) a decrease in tip clearance of axial flow machines generally causes an increase in pressure rise and a delay in the onset of stall as the flow is throttled. Theoretically, however, the optimum performance is not necessarily associated with the smallest clearance, but a clearance greater than zero. Unfortunately, typical turbomachines cannot be built within the tight tolerances associated with such a minimum non-zero tip clearance, with the result that the gap is always greater than this optimum and therefore the above dictum holds true in most cases. Extrapolating this concept from axial flow rotors to their mixed flow counterparts, it would be reasonable to find a non-zero optimum tip clearance in the latter case also.

However, Saha et al. (1995) investigated this phenomenon extensively and found no evidence of this optimum as the performance only improved with a decrease in clearance. Refer to figure 2.1. In fact, their analysis showed a linear variation of head with tip clearance in the normal operating area. The same was observed for the efficiency. Soundranayagam et al (1996) confirm this.

2.4.3 Recirculation

A reduction in flow rate with an increase in pressure rise could lead to flow reversal in the annulus. Saha et al (1995) noted that this flow phenomenon at low flow rates starts at the inlet side of the tip region (see figure 2.3). With a further decrease in flow rate, the spatial extent of this eddy increases. They believe that this flow reversal has two main influences:

As the reversal eddy increases in size, part of it moves into the impeller space, where it acquires angular momentum and has work done on it. The momentum and energy is transported upstream which leads to a high stagnation pressure in the region in front of the impeller tip. This can be seen in the graph shown in figure 2.3.
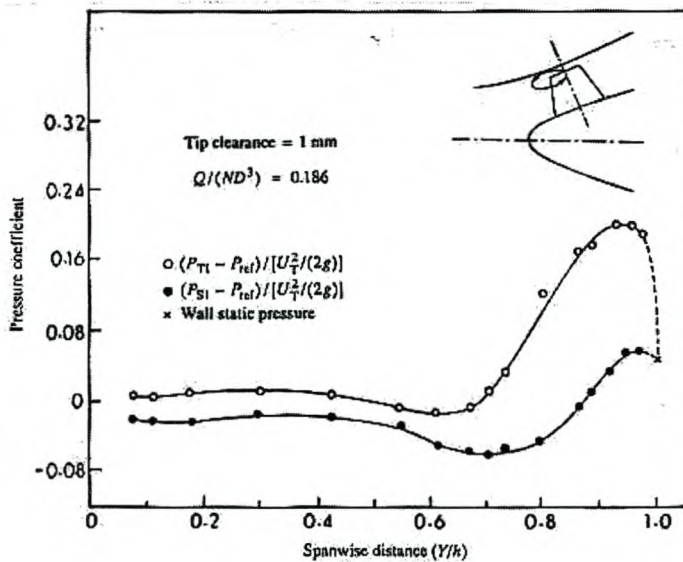
Figure 2.3: Pressure distribution along the span of a mixed flow pump with recirculating flow. (Saha et al, 1995)

The second result of this eddy at the inlet is that the flow angles change. These changes are brought on by the prerotation at the inlet and also the shift in streamlines as the flow is shifted toward the hub at the inlet, and toward the casing at the exit because of the reversal eddy at the hub. The partial blockage of the flow causes a slight increase in the meridional velocity. Saha et al. (1995) notes that the size of the tip clearance does not have a noticeable influence on the flow velocities.

2.5 Conclusion

It is clear that no systematic design methodology is available. No useful, verifiable, quantifiable guidelines are given in terms of geometry. This makes the simulation of a fan difficult, as the designer is not limited in the range of values of the design variables at his or her disposal. Experimental work done is mostly centred on pumps rather than fans or compressors, which leads to some uncertainty in the compressible domain.

CHAPTER 3

AERODYNAMIC DESIGN OF MIXED FLOW FANS

"It is important to recognize that the design of any turbomachine is an interdisciplinary process, involving aerodynamics, thermodynamics, fluid dynamics, stress analysis, vibration analysis, the selection of materials, and the requirements of manufacturing. "

- A Whitfield and NC Baines

In this chapter the problem of designing mixed flow fans is addressed by breaking it down into a number of discrete parts. The aim is to make the investigation more generic, as every design is a culmination of unique choices and does not represent the full array of designs. The implementation and the subsequent look at interfaces will follow separately.

3.1 Aspects of mixed flow fan design

3.1.1 Dimensional analysis

Dimensional analysis has two main applications in the design process: turbomachine classification and the estimation of maximum efficiency.
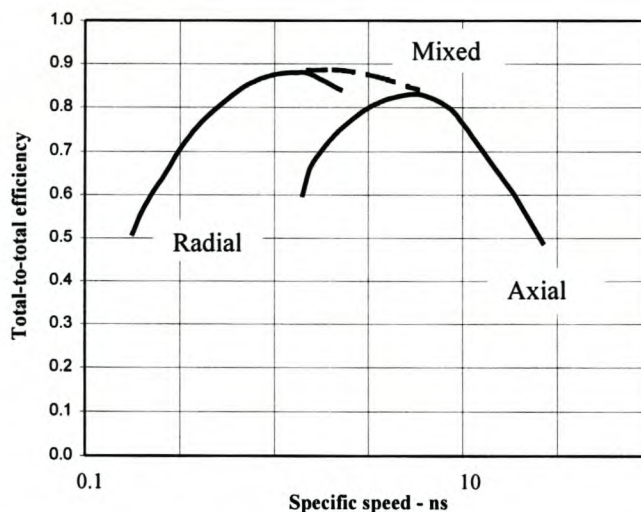
Figure 3.1: Domain of operation for turbomachines (Sayers, 1990)

Knowing which type of turbomachine, i.e. radial, mixed or axial flow, will be best suited for a certain application is important, as each type of turbomachine has its own operating range in terms of specific speed and more importantly, an associated maximum efficiency. Apart from

3.1

working with the right machine, the dimensional analysis has the added advantage of relating maximum efficiency to dimensionless speed. Although these values may not be very accurate, it is a good initial guess and gives the designer a target to aim for. It would seem that the MFF theoretically has the best efficiency, in the range indicated in figure 3.1, of the three types mentioned. Equation 3.1 is a curve fit of the dashed line in figure 3.1, and is therefore a means of finding an approximate, theoretical maximum efficiency of the MFF:

$$\eta = -0.01n_s^2 + 0.018n_s + 0.88 \qquad 1.5 \le n_s \le 5.8 \qquad 3.1$$

where the specific speed is given by equation 3.2.

$$n_s = \frac{NQ^{\frac{1}{2}}}{(gH)^{\frac{3}{4}}} \qquad\qquad 3.2$$

3.1.2   Euler turbomachinery equation and vector analysis

The Euler turbomachinery equation is derived from the conservation of angular momentum along a frictionless streamtube of arbitrary shape. See Cumpsty (1989). The equation is therefore valid for all types of turbomachines independent of geometry and relates the work done by the machine to a change in whirl.

$$\dot{W}/m = \omega(r_2 V_{u2} - r_1 V_{u1}) \qquad\qquad 3.3$$

Equation 3.3 formulates this equation in the most general way. For the purpose of MFF analysis, Soundranayagam et al (1996) wrote this equation in an alternative two-term form:

$$\dot{W}/m = \omega^2(r_2^2 - r_1^2) + \frac{\omega \Gamma Z}{2\pi} \qquad\qquad 3.4$$

The derivation of equation 3.4 from equation 3.3 is given in Appendix F. The first term on the right-hand side of equation 3.4 represents the work done by the Coriolis forces and is independent of the number or geometry of the blades. Cumpsty (1989) notes that this work, which is due to a radial shift in streamlines, is unconnected to the flow processes and subsequently has no loss-generating mechanisms associated with it and therefore also no increase in entropy. Another advantage is that, unlike the work done by the blades, there is no aerodynamic limit to this term. In fact, it is usually material considerations that limit the size and speed of purely radial machines. The second term on the right-hand side contains

information on the number of blades as well as the blade circulation. This hints at the possibility of using existing two-dimensional (2D) cascade data in the design of the MFF.

This consideration of the Euler equation reveals that the work done is a result of a combination of a change in radius of the streamlines and the whirl velocity. In purely axial flows, the radius stays constant and can subsequently be taken out of the brackets, leaving the change in whirl as the only work generating mechanism. Axial flow fan designers can simplify this by assuming an axial inlet velocity profile (i.e. zero inlet whirl), which means that the work done is now directly proportional to the outlet whirl, limited only by the amount that the blade can physically turn the flow. In MFFs, where the flow has both axial and radial components, much of the work is done through a change in radius. In both cases, however, the designer has to calculate the whirl at the inlet and exit, taking into account that, in general, the radii of the streamlines will change through the impeller.

An important consideration is the variation of the work done along the span of the blade. A simple and popular choice is to assume that the work done is constant along the span. From equation 3.3 it evident that for a constant radius (purely axial flow) this distribution requires that the difference between inlet and exit whirl velocities be inversely proportional to radius. This is called a free vortex exit velocity profile. One way of implementing a free vortex velocity profile in a turbomachine where there is a significant change in streamline radius through the blade (for example a MFF) is to design the fan with a zero inlet whirl. This eliminates the second term of equation 3.3, requiring that the outlet whirl be inversely proportional to the exit radius and conveniently allows for a free vortex exit velocity profile in MFFs.

With these considerations in mind, the designer has to solve the inlet and exit velocity triangles. These triangles represent the flow vectors at different stations along the blade span. The number of stations depends on the designer's preference and the amount of detail required. For preliminary investigations, three stations (root, mean and tip) will suffice.

To solve the velocity triangles, the mass or volume flow and the static pressure rise are required. The designer will have to assume an initial meridional velocity distribution for both inlet and exit, which will be refined by a through-flow method of some sort. This will be discussed in detail later in this chapter. In order to simplify the theory in rest of the chapter, a generic (inlet or exit) velocity triangle is presented in figure 3.2; the set of equations necessary to solve all the components is given in table 3.1.

Mixed Flow Fans
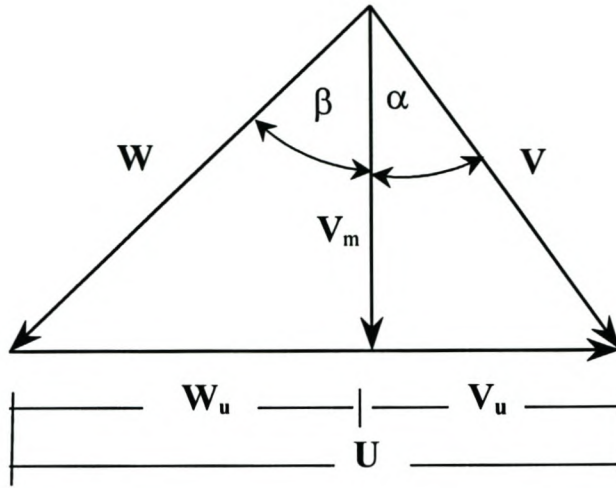
Figure 3.2: Generic velocity triangle for flow through the rotor of a fan

Equation	Number	Comment
$V_m = \dfrac{\overset{\bullet}{m}}{\rho(2\pi h r_{mean})}$	3.5	Assume a uniform meridional velocity distribution
$U = \omega r$	3.6	
$W_u = U - V_m \tan(\alpha)$	3.7	If α is known
$W_u = U - V_u$	3.8	If V_u is known
$\alpha = \tan^{-1}\left(\dfrac{V_u}{V_m}\right)$	3.9	If V_u is known
$\beta = \tan^{-1}\left(\dfrac{U - V_u}{V_m}\right)$	3.10	
$W = \dfrac{V_m}{\cos(\beta)}$	3.11	
$V = \dfrac{V_m}{\cos(\alpha)}$	3.12	

Table 3.1: Equations to solve generic velocity triangle

3.4

The inlet flow can almost be seen as a 'boundary condition' in the solution to the flow, but the exit flow is very much influenced by the design itself. Keep in mind that, according to the Euler equation, the flow has to be turned by a certain amount for the specified work to be done. Theoretically, this turning is done by an infinite number of ideal, extremely thin blades. The flow follows these blades perfectly and the outlet flow triangles can subsequently be derived from the Euler equation as given in equation 3.3. In real fluid flow there is a finite

number of blades with a finite thickness that only turn the flow approximately to the desired angle. The difference between the theoretical and actual flows is mainly due to two effects: slip and deviation. These two effects are so important in MFF design that they will be discussed separately. For the purpose of this paragraph, they will simply be used as terms in equations that are used to solve the exit velocity triangles. Figure 3.3 illustrates the shift in the flow vector caused by them.

From continuity, the exit meridional velocity can be solved. This can either be
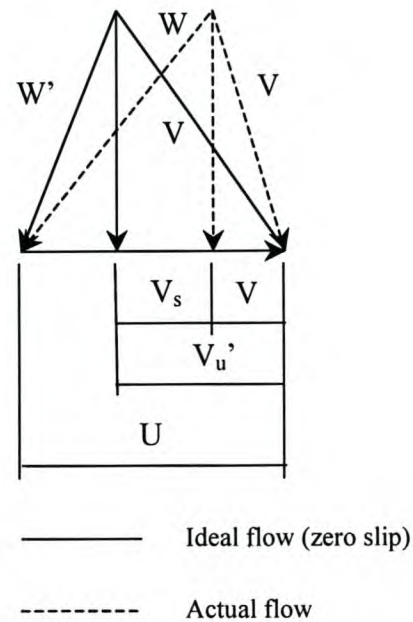
Figure 3.3: Exit velocity triangle

done by using the annulus geometry (see equation 3.5) and doing a hand calculation, or by using a through-flow method of some sort that would solve for the meridional velocity distribution. In this project the matrix through-flow method (MTFM) is used. See chapter 4. Using the specified exit whirl as an input to MTFM, the absolute and relative velocity vectors can be found through numerical simulation. The first problem facing the designer is that due to slip even ideal blades would not be able to turn the flow in such a way that the required change in whirl is produced. In order to explain the implication of this slip term, it may be useful to consider the analysis problem as opposed to the design approach.

The aim of *analysis* is to find the performance given certain known quantities. This may include whirl, rotational speed and volume flow. The slip can then be calculated using some correlation and the fan total pressure is found with equation 3.13.

3.5

$$P_{fl} = \rho[U_2(V_{u2} - V_s) - U_1 V_{u1}]$$ 3.13

Equation 3.14 gives the exit relative flow angle with the effect of slip taken into account. This angle therefore represents the actual relative flow angle that would, because of the effect of slip, be more than the blade relative flow angle.

$$\beta_2 = \tan^{-1}\left(\frac{U_2 - (V_{u2} - V_s)}{V_{m2}}\right)$$ 3.14

The aim of the *design* problem, however, is to find the whirl distribution that would do a specified amount of work after the effect of slip has been taken into account.

$$V_{u2} = \frac{P_{fl}}{\rho U_2} + V_s$$ 3.15

For zero inlet whirl equation 3.13 can be rewritten to express the tangential component of the exit absolute flow velocity in terms of the fan total pressure, density, tangential velocity at the exit and the slip velocity. See equation 3.15. For a given geometry, fluid and fan total pressure, the required value of the exit whirl velocity of a real turbomachine will be more than for a ideal turbomachine where the slip is zero. From a blade design point of view, it is more useful to express these quantities in terms of a change in exit relative flow angle as in equation 3.16.

$$\Delta\beta = \beta_1 - \beta_2$$ 3.16

Substitute equation 3.15 into equation 3.10 to find equation 3.17 - an expression for β_2 as a function of the fan total pressure and the slip velocity. It is apparent that an increase in slip causes a decrease in β_2, which in turn increases $\Delta\beta$ as shown in equation 3.16. Because the change in relative flow angles from inlet to exit is directly related to the camber of the blade, the increase due to slip in $\Delta\beta$ results in an increase in blade camber. Details on blade design are given in section 3.2.

$$\beta_2 = \tan^{-1}\left[\frac{U_2 - \left(\frac{P_{fl}}{\rho U_2} + V_s\right)}{V_{m2}}\right]$$ 3.17

Stodola (1927) proposed a theory that slip is caused by a relative eddy in the blade annulus (see next section). Keeping in mind that this was proposed for a purely radial machine, Sarkar

(1992) approached the problem by postulating that in MFFs only a component of the eddy is in the radial direction and therefore only a component of the calculated slip should be used. Sarkar used the Stodola slip correlation and simply found the relevant slip factor by multiplying the value by the ratio of the component of the eddy vector in the radial direction over the full vector, i.e. the sine of the half-cone angle.

$$V_{s,MFF} = V_s \sin\gamma \qquad\qquad 3.18$$

Myles (1965) also considers slip correlations in the design of MFFs other than Stodola's and therefore equation 3.18 is given in a more general form.

Once the turning of the flow through the blade has been determined, the design process proceeds to the development of the blades. It is important to note that even if the designer could predict the slip precisely and therefore specify the correct amount of change in whirl, and even if the blade were designed to have a difference in inlet and exit angle equal to the specified turning, that this turning would, in general, not be achieved. The difference between the angle through which the blade was supposed to turn the flow and the angle it was really turned is called deviation.

3.1.3 Deviation and slip

Circumferentially averaged flow through a blade row, in general, does not follow the blade surface. In axial flow compressors this deviation of the flow from the blade surface is expressed in terms of the change in the exit relative angle called the deviation angle. When axial flow compressors and fans have a solidity (ratio of the blade chord to the blade pitch at a given radius) of more than 0.8, the blades act collectively to guide the flow. Cumpsty (1989) argues that deviation is a potential flow mechanism and explains it as follows:

The impeller blade experiences a load due to both the rotation of the blade and the fluid flow. This load manifests itself in the form of a high pressure on the one side (pressure surface) and a low pressure on the other side (suction surface) of the blade, causing a net force on the blade in a direction opposite to the rotation. Now consider the channel between two impeller blades. Because of the difference in pressure between the pressure and suction surfaces, the pressure distribution in the channel, going from the one blade to the next, is non-uniform. This results in a force that tries to turn the flow in the direction of rotation and more importantly, does work on the fluid. In an ideal blade passage this pressure difference will be maintained from leading to trailing edge, turning the flow perfectly, i.e. ensuring that it does not depart from

the surface of the blade. In reality the difference in pressure between the pressure and suction surface has to be zero at the trailing edge in accordance with the Kutta condition. This reduction in pressure difference across the blade has to be gradual and will start upstream of the trailing edge, causing a reduction in pressure difference in the blade-to-blade channel. The result is a decrease in the blade's ability to turn the flow at the trailing edge and a subsequent deviation of the flow direction from the blade exit angle.

Sarkar (1992) used Howell's correlation (see equation 3.19 and 3.20) in the design of his mixed flow impeller to calculate the deviation. β'_2 is the nominal fluid outlet angle.

$$\delta = m\theta \frac{1}{\sqrt{\sigma}} \qquad\qquad 3.19$$

$$m = 0.23 + 0.1\left(\frac{\beta'_2}{50}\right) \qquad\qquad 3.20$$

Saha et al. (1995) referred to Horlock (1958) for the calculation of the deviation. The author believes that this implies that they used the Howell correlation as well.

In radial flow compressors the deviation of the flow from the impeller is expressed in terms of the change in the tangential component of the absolute flow velocity and called the slip velocity. Stodola (1927) postulated that a rotation free inviscid fluid entering the radial impeller should remain rotation free as it passes through the blade passage. Due to the fact that the impeller has an angular velocity ω, the fluid must have an angular velocity $-\omega$ relative to the impeller in order to remain rotation free. This rotation manifests itself in the form of a relative eddy that induces at the rotor exit a velocity perpendicular to the radius of the impeller in the opposite direction to the tangential velocity. The size of the resulting whirl velocity vector is reduced because of the slip with a subsequent reduction in Euler work being done. Cumpsty (1989), however, does not distinguish between the mechanisms causing slip and deviation. He postulates that slip happens as a result of the Kutta condition, which, similar to deviation, causes a reduction in pressure difference in to blade passage toward the trailing edge. It is clear that slip is an inviscid phenomenon despite the fact that one could argue that due to the deceleration of the fluid on the suction surface, the subsequent increase in pressure might lead to boundary layer separation. According to Cumpsty (1989) this is seldom the cause of slip. Both deviation and slip happen as a result of inviscid flow mechanisms, but slip is caused by relative rotation, something not seen in axial flow cascades.

In the previous section, it is shown how slip affects the exit velocity profile by reducing the actual outlet whirl. Many empirical correlations exist that try to predict the amount of slip given certain conditions, all of them using a non-dimensional formulation of slip called the slip factor. It is defined as (unless otherwise stated):

$$\sigma = \frac{V_u - V_s}{V_u} \qquad \qquad 3.21$$

In 1927 Stodola introduced the first slip correlation, based on the relative eddy hypothesis that induces the slip velocity between the blades:

$$\sigma_s = 1 - \frac{\pi \sin \beta_2}{Z\left[1 - \left(\dfrac{V_{r2}}{U_2}\right)\cot \beta_2\right]} \qquad \qquad 3.22$$

Empirical studies show that equation 3.22 is most effective in the range $20° < \beta_2 < 30°$. Busemann (1928) did a more thorough theoretical analysis resulting in equation 3.23 that is viewed by Wiesner (1967) as universally the most applicable expression for slip. He states that equation 3.23 seems to work best in the range $30° < \beta_2 < 80°$.

$$\sigma_B = \frac{A - B\left(\dfrac{V_{r2}}{U_2}\right)\cot \beta_2}{1 - \left(\dfrac{V_{r2}}{U_2}\right)\cot \beta_2} \qquad \qquad 3.23$$

A and B are functions of β_2, Z and r_2/r_1. Wiesner (1967) shows that this equation can be reduced to a simpler form as shown in equation 3.24.

$$\sigma_B = 1 - \frac{\sqrt{\sin \beta_2}}{Z^{0.70}} \qquad \qquad 3.24$$

3.1.4 Geometry and blade design

The ideal shape of the hub and casing of a MFF is spherical. The shape has two advantages: it imparts a radial component to the meridional flow and if designed correctly, allows the rotor blades to have an adjustable pitch with a constant (or zero) clearance between the blade base and the hub surface and the blade tip and casing surface. Myles (1965), Sarkar (1992) and Saha et al. (1995), however, chose to design mixed flow rotors with conical hubs and casings. It simplified their design as well as the transformation of the blade data to a rectangular

cascade (discussed in the next paragraph) and made the interpretation of the experimental results easier. In this project both the hub and casing had a conical shape and both cone angles were the same value, resulting in a parallel annulus.

Two parameters are important in describing the annulus geometry: cone angle and radius ratio. The cone angle (γ) and the radius ratio (r_2/r_1) are shown in figure 3.4.
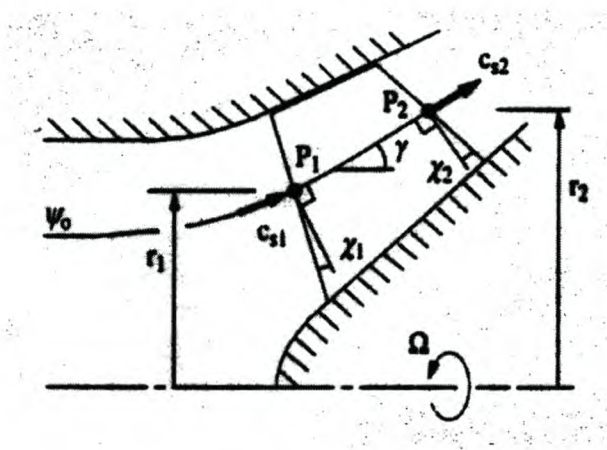
Figure 3.4: Meridional annulus geometry of a MFF (Lewis, 1996).

The radius ratio is coupled to the cone angle in such a way that for a given blade chord, it increases with an increase in cone angle. The values of the cone angle and radius ratio are influenced by the following factors:

➢ The flow has to be turned from the axial direction at the inlet of the rotor to the desired cone angle. An increase in cone angle causes a greater curvature at the inlet to the rotor, which may lead to a non-uniform, peaky meridional velocity distribution.

➢ Maximum overall length of the rotor section.

➢ For a given solidity, an increase in the number of blades leads to an decrease in the chord length of each blade which would lead to a decrease in radius ratio.

Myles (1965) used a limiting radius ratio of 1.2, but did not explain why. Soundranayagam et al. (1996) used their experimental work to break down the work done into its aerodynamic and Coriolis parts. Their blade geometry was such that the radius ratio increased from tip to hub and they were consequently able to investigate the effect radius ratio had on the two work terms. At the tip, where the ratio was low, the aerodynamic work was greater than the Coriolis work. This situation gradually changes until the hub was reached where the radius ratio was much higher with the result that the Coriolis work dominated to such an extent that negative

aerofoil work would be required with a subsequent drop in local pressure rise. Unfortunately these authors gave no limiting value, but it is clear that one must exist.

3.1.5 Conformal transformation

The aim was to transform a rectangular cascade geometry onto a conical surface. If a transformation is conformal it can be shown that the solution to the Laplace equation is invariant under the transformation. This implies that the value of the stream function is the same for both the rectangular and transformed plane at corresponding points. Refer to figures 3.5 and 3.6 for a graphical representation of the transformation.
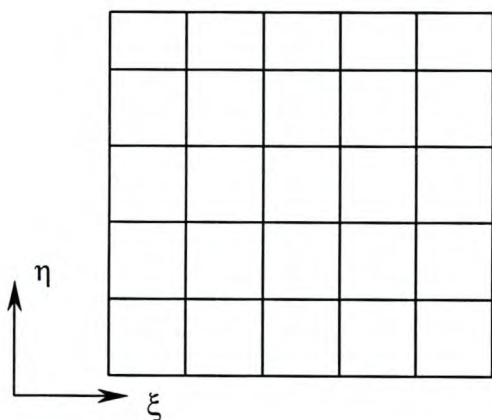
Figure 3.5: Rectangular η - ξ plane   **Figure 3.6: Transformed plane**
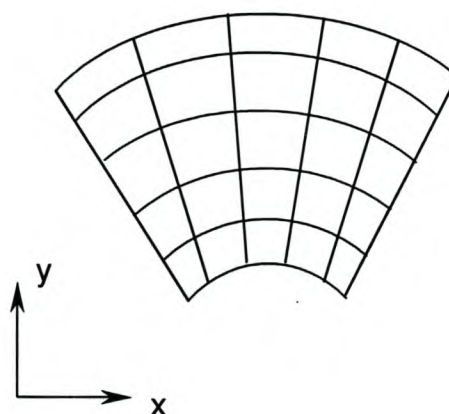
Venter (1993) used the following transformation to transform a rectangular cascade to a radial cascade with outer radius, R.

$$z = x + iy = R\left(e^{\lambda \zeta}\right) \qquad\qquad 3.25$$

$$\zeta = \xi + i\eta \qquad\qquad 3.26$$

$$\lambda = \frac{2\pi}{Zt} \qquad\qquad 3.27$$

Z is the number of blades and t is the spacing between the blades.

Equation 3.25 expresses the complex number z in both the rectangular and polar forms. Using the Euler formula[*], the polar form could be expanded as shown in equation 3.28.

---

[*] See Kreyszig, Erwin, 1988, Advanced Engineering Mathematics, 6th Edition, for further information.

$$z = R.e^{\lambda(\xi+i\eta)} = R.e^{\lambda\xi}[\cos(\lambda\eta) + i\sin(\lambda\eta)] \qquad 3.28$$

From equation 3.25 and 3.28, the values of x and y could be derived.

$$x = \mathrm{Re}^{\lambda\xi}\cos(\lambda\eta) \qquad 3.29$$

$$y = \mathrm{Re}^{\lambda\xi}\sin(\lambda\eta) \qquad 3.30$$

Compare the difference between Venter's transformation (radial) and the conical transformation as shown in figures 3.7 and 3.8.
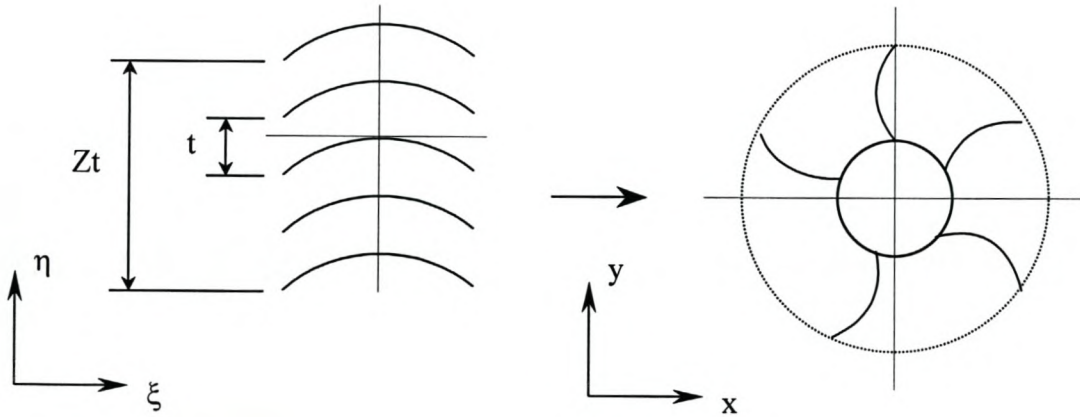
Figure 3.7: Venter's conformal transformation
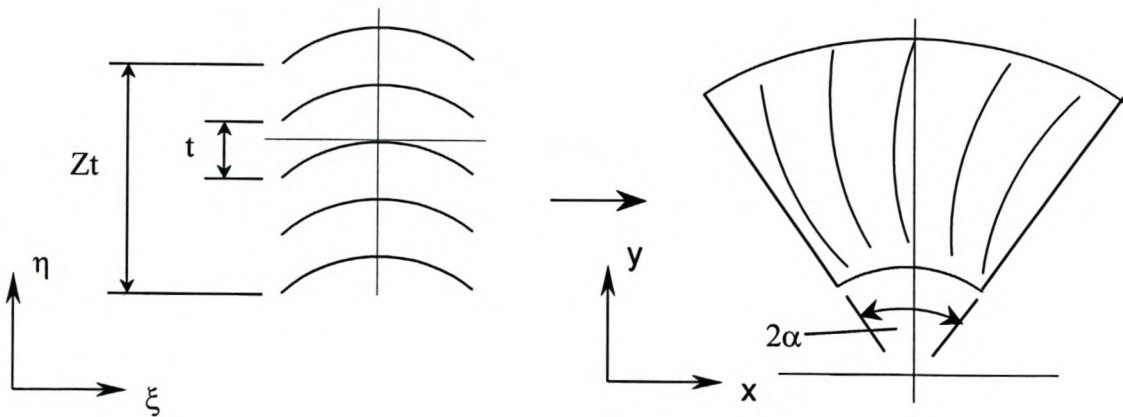
Figure 3.8: Conformal transformation of a rectangular to a developed conical cascade

3.12

To understand the significance of λ, a variable r was defined as its inverse. Equation 3.27 could then be written in the form:

$$2\pi r = Zt \qquad\qquad 3.31$$

The symbol r is the radius of the circle that has a circumference equal to the total height of the rectangular cascade, Zt. From this understanding, the transformation to a conical surface (figure 3.8) could be derived by defining a new variable:

$$\lambda_{cone} = \frac{2\alpha}{Zt} \qquad\qquad 3.32$$

This implies that the inverse of λ_{cone} is the radius of the arc that has the same length as Zt. Note that this is a more general formulation that incorporates the radial transformation $(\alpha = \pi)$. The angle α is related to γ, the cone half-angle, as follows:

$$\alpha = \pi \sin \gamma \qquad\qquad 3.33$$

The transformation was therefore:

$$x = \mathrm{Re}^{\lambda_{cone}\xi} \cos(\lambda_{cone}\eta) \qquad\qquad 3.34$$

$$y = \mathrm{Re}^{\lambda_{cone}\xi} \sin(\lambda_{cone}\eta) \qquad\qquad 3.35$$

From equations 3.34 and 3.35 the transformation could be written in polar form:

$$z_{cone} = \mathrm{Re}^{\lambda_{cone}\varsigma} \qquad\qquad 3.36$$

During the investigation of the transformation, two observations were made.

➢ R was simply a scaling factor and did not influence the shape of the transformed function.

➢ The arguments, λ and η, in equations 3.34 and 3.35 could be described as 2α times the ratio of the distance along the vertical axis of the rectangular cascade and the completed distance, Zt. This implied that these arguments vary between zero and 2α. Travelling along the vertical axis in the rectangular plane corresponded with a change in the so-called sweep angle – the angle that spans the conical cascade.

Appendix G relates the transformation done in this project to one done by Lewis (1996).

3.2 Implementation of design procedure

To investigate all permutations involved in the design of the MFF by hand would have been tedious, especially since there were two instances in the main design algorithm where the solution had to be found iteratively. Subsequently, a computer program was written.

Figure 3.9 shows the design algorithm that is described in the following paragraphs.

A. Get design parameters

Fan performance was quantified in terms of the total pressure rise for a given volume flow. These parameters were constrained by other input parameters like the maximum diameter, maximum radius ratio, rotational speed of the machine and cone angle. Some of the input parameters were fixed (duty point and maximum diameter), but the others were changed throughout the design procedure until a satisfactory solution was found. The final selections for these input values for the fan designed in this project are shown in table 3.2 and were chosen such that the fan had a specific speed of 4.2.

Parameter	Unit	Value	Fixed
Fan total pressure rise	Pa	350	✓
Volume flow	m^3/s	3.1	✓
Maximum diameter	mm	630	✓
Radius ratio (r_2/r_1)	-	1.83	✗
Rotational speed	rpm	960	✗
Cone angle	°	30	✗

Table 3.2: Final input values for mixed flow fan design

B. Calculate velocity triangles

All velocity vector calculations were done at a number of predefined stations. The first step was to get the meridional velocity profile for both inlet and exit. For the first iteration in the design process a uniform distribution was calculated from the mass flow and annulus geometry. The designer had enough information to solve for the inlet flow. In this project a zero inlet whirl was assumed, which meant that the inlet absolute flow velocity equalled the inlet meridional velocity. Using the equation 3.3 (Euler turbomachinery equation) along with

a specified profile, the whirl distribution could be calculated and the exit velocity triangle solved. In this project, a free vortex exit whirl profile was chosen.

C.   Calculate slip and deviation

The calculation of deviation was an iterative procedure: the deviation angle is a function of the camber, which in turn is a function of the deviation angle. As mentioned in section 3.1.2, the camber of the blade was related to the change in relative flow angles and was therefore expressed as an angle. Initially, the camber was taken as just the difference between the relative inlet and exit flow angles. This initial value for the camber was then used to calculate the deviation and the slip. From the slip velocity it was possible to calculate the change in relative exit angle. The incidence, deviation and change in relative angle due to slip was added to the change in flow angles between inlet and exit to find the camber. The incidence is usually taken as negative, but in this project, due to a lack of information, a zero incidence was chosen. The process was repeated until the solution converged.

In section 3.1.2 it is explained that because only a component of the relative eddy in the MFF is in the radial direction, the slip velocity is given by equation 3.18. Deviation is caused by a potential flow mechanism that is taken into account in the conformal transformation.

D.   Test for convergence

The change in deviation is taken as the measure of the convergence. The tolerance used in this project is 10^{-3} degrees.

E.   Through flow analysis

The newly calculated values for the whirl velocity at the various radial stations acted as input to the MTFM, written for this project. After the analysis was done, the determined meridional velocity distribution acted in turn as the new input for the mixed flow fan design algorithm.

A. Get design parameters

B. Calculate triangles

C. Calculate the slip and deviation

No

D. Convergence?

Yes

Whirl

Matrix Through Flow Method

E. Through flow analysis

F. Check blade loading

Meridional Velocity

No

G. Convergence?

Yes

H. Blade profiles and conformal transformation
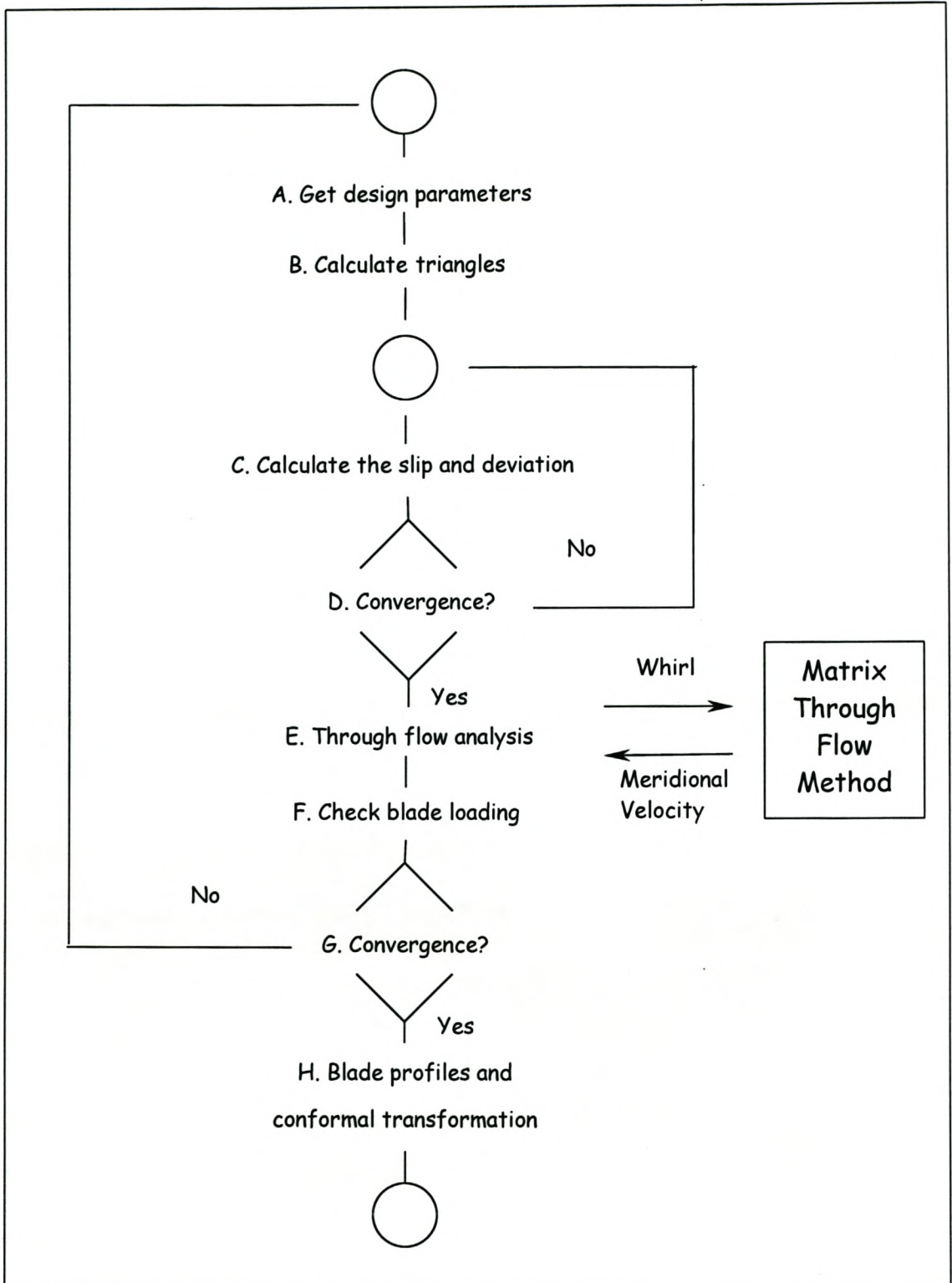
Figure 3.9: Algorithm for the design of a mixed flow fan

F.   Check blade loading

Two well-known quantities associated with blade loading, the de Haller velocity ratio and the diffusion factor (DF) were calculated to check the blade loading. See equations 3.37 and 3.38.
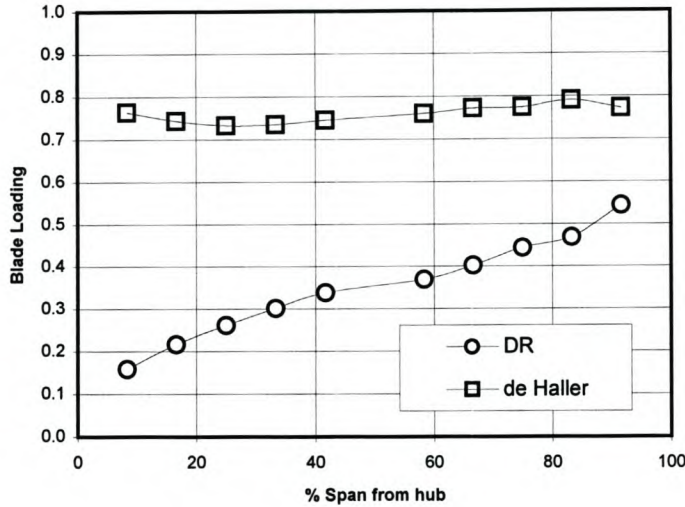
Figure 3.10: Graph of de Haller and DF load factors

$$deHaller = \frac{W_2}{W_1}$$

3.37

$$DF = 1 - \frac{V_2}{V_1} + \frac{(V_{u2} - V_{u1})}{2\sigma V_1}$$

3.38

Cumpsty (1989) notes that the DF should be less than 0.6 and the de Haller ratio more than 0.75. Figure 3.10 shows each of these loading factors as a function of the vertical distance from the hub to the casing, expressed as a percentage of the total span.

G.   Primary convergence

Four complete iterations (from A to G) were done to find the final solution. The meridional velocity distribution after each iteration was compared to the previous one until the maximum change was less than the onvergence tolerance (1.0 m/s).

3.17

H. Blade profile and conformal transformation

Multiple circular arc (MCA) blades were used and were preferred because of their flexibility: it was possible to generate a wide range of profiles from thin supersonic to fat subsonic shapes by manipulating a number of parameters. The parameters needed to generate a profile are blade chord, position of maximum camber (measured from the leading edge as a fraction of the chord), camber, maximum thickness as well as leading and trailing edge radii. See Appendix A. The camber is defined as:

$$\theta = \beta_1 - \beta_2 + \delta + \Delta\beta_{slip} \qquad\qquad 3.39$$

where

$$\Delta\beta_{slip} = \tan^{-1}\left[\frac{U_2 - \dfrac{P_{ft}}{\rho U_2}}{V_{m2}}\right] - \tan^{-1}\left[\frac{U_2 - \left(\dfrac{P_{ft}}{\rho U_2} + V_{s,MFF}\right)}{V_{m2}}\right] \qquad\qquad 3.40$$

Note that the slip velocity used in equation 3.40 is only the component of the slip velocity as described by equation 3.18. Once the profiles had been generated, they were stacked from root to tip, with the inclusion of stagger, along a line perpendicular to the hub and casing to form the blade. This line, the so-called stacking line, ran through the centre of area of each blade section. Because MCA profiles were used, the angle of attack of the profile was simply half the camber angle and therefore the equation for the stagger angle reduced to:

$$\xi = \beta_1 - \frac{\theta}{2} - i \qquad\qquad 3.41$$

This blade had now been defined in a rectangular coordinate system and each section had to be transformed to a conical surface, using equations 3.34 and 3.35. Figure 3.11 shows a comparison between the designed and transformed blade sections as viewed along the stacking line.
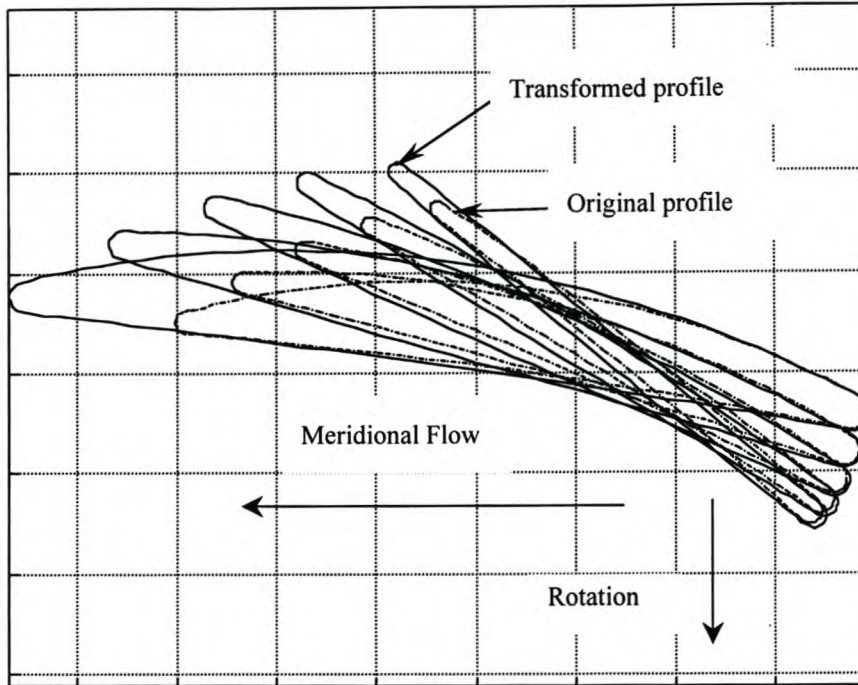
Figure 3.11: Conformal transformation of MFF blade.

3.3 Results of mixed flow fan design

The rotor was divided into ten sections. For each of these sections the design procedure, as described in this chapter and shown figure 3.9, was applied. Tables 3.3 and 3.4 contain the solution of the velocity triangles for each section after the final iteration. Notice that α, the absolute flow angle, was zero for the inlet, as there was no pre-whirl into the rotor. The values for α at the exit were non-zero and ranged from 50° to 43°. Although it was not quite achieved in this design, Von Backström et al. (1996) recommended that the value for α should not exceed 48° to avoid back flow at the hub. Strictly speaking, this rule of thumb should only apply to axial fans, but the author decided to use it because this method tried to cast the mixed flow design methodology into an axial fan design mould. Notice the reduction in average meridional velocity from 19 m/s to 15 m/s through the rotor. This deceleration was as a result of the increase in through flow area.

The information from the inlet and exit velocity triangles at the various rotor sections were used in conjunction with slip and deviation correlations to find the blade shape. Table 3.5 shows the results of the final iteration of the design before conformal transformation. Notice that both the effects of slip and deviation decreased from hub to tip. The last column of table

3.5 shows the stagger angle. Due to the choice of exit whirl distribution, the stagger ranged between 5° and 40°, resulting in a severely twisted blade.

h [m]	V [m/s]	Vm [m/s]	Vu [m/s]	U [m/s]	W [m/s]	Wu [m/s]	α [°]	β [°]
0.01	19.27	19.27	0.00	6.76	20.42	6.76	0.00	19.33
0.02	19.51	19.51	0.00	8.03	21.10	8.03	0.00	22.36
0.03	19.44	19.44	0.00	9.30	21.55	9.30	0.00	25.56
0.04	19.35	19.35	0.00	10.56	22.05	10.56	0.00	28.63
0.05	19.30	19.30	0.00	11.83	22.64	11.83	0.00	31.51
0.07	19.29	19.29	0.00	13.10	23.31	13.10	0.00	34.19
0.08	19.30	19.30	0.00	14.37	24.06	14.37	0.00	36.67
0.09	19.35	19.35	0.00	15.64	24.88	15.64	0.00	38.95
0.10	19.39	19.39	0.00	16.90	25.73	16.90	0.00	41.08
0.11	19.35	19.35	0.00	18.17	26.55	18.17	0.00	43.20

Table 3.3: Summary of the inlet flow calculations

h [m]	V [m/s]	Vm [m/s]	Vu [m/s]	U [m/s]	W [m/s]	Wu [m/s]	α [°]	β [°]
0.01	24.03	15.40	18.44	20.83	15.59	2.39	50.12	8.83
0.02	23.35	15.19	17.74	21.65	15.68	3.91	49.43	14.45
0.03	22.64	14.84	17.09	22.48	15.79	5.39	49.03	19.94
0.04	22.10	14.71	16.49	23.30	16.21	6.81	48.27	24.84
0.05	21.71	14.75	15.93	24.12	16.87	8.19	47.20	29.05
0.07	21.44	14.92	15.40	24.94	17.71	9.54	45.91	32.59
0.08	21.21	15.09	14.91	25.76	18.58	10.85	44.66	35.72
0.09	20.80	14.96	14.45	26.58	19.26	12.13	44.01	39.04
0.10	20.77	15.33	14.02	27.40	20.35	13.38	42.44	41.12
0.11	19.80	14.38	13.61	28.23	20.50	14.62	43.43	45.47

Table 3.4: Summary of the exit flow calculations

h [m]	βm [°]	Vs [m/s]	Δβ$_{slip}$ [°]	δ [°]	θ [°]	σ [-]	c [m]	ξ [°]
0.01	16.85	2.94	10.86	6.30	27.65	1.18	0.14	5.51
0.02	20.30	2.99	10.99	6.19	25.08	1.10	0.14	9.82
0.03	23.96	3.02	10.88	5.99	22.49	1.03	0.13	14.32
0.04	27.48	3.02	10.39	5.68	19.87	0.96	0.13	18.70
0.05	30.71	3.01	9.69	5.34	17.49	0.89	0.12	22.77
0.07	33.64	3.00	8.93	5.04	15.57	0.83	0.12	26.41
0.08	36.33	2.99	8.19	4.76	13.90	0.77	0.11	29.72
0.09	38.98	2.95	7.50	4.22	11.62	0.72	0.11	33.14
0.10	41.09	2.95	6.88	4.21	11.04	0.67	0.10	35.56
0.11	44.11	2.83	6.12	2.64	6.50	0.62	0.10	39.95

Table 3.5: Summary of the blade profile calculations

3.4   Conclusion

The design method outlined in this project was derived from a number of separate ideas found in the literature. One aspect of the method found lacking, was information on how to assess blade loading. Due to a lack of information, the formulations used, as well as the limiting values (see figure 3.10) were borrowed from axial flow theory. Although the design values were within the acceptable range, they do not seem to take radius ratio into account and therefore the designer queries the validity of these values.

CHAPTER 4

THROUGH FLOW ANALYSIS

"No-one can tell you what the Matrix is, you have to see it for yourself"

- Morpheus

From the previous chapters, it is clear that knowledge of the meridional velocity distribution before, through and after the fan is essential in the aerodynamic design of the MFF. In the design of axial flow fans, the designer often calculates the velocity vectors an 'infinite' distance before and after the blade row and then translates these vectors with the help of actuator disc theory until they represent the flow at the rotor inlet and outlet. For axial flow machines this approach works well and is easy to implement (Van der Spuy, 1997). For mixed flow fans, however, the change in geometry through the blade row made this type of analysis complex and unpractical. Subsequently, the designer had to use some numerical method to solve for the through-flow properties.

The designer had a choice of numerical methods. A full Computational Fluid Dynamic (CFD) analysis would be ideal, but this is a specialised and complex field and requires a lot of computing time. Another option was to use one of the so-called through-flow methods. They are well known in the turbomachinery environment and have the main advantage of being simple to implement. Examples of through-flow methods are the Streamline Curvature Method (SCM), Streamline Through-flow Method (STFM) and the Matrix Through-flow Method (MTFM). All these methods have a common aim: to solve for the streamline distribution in a given flow geometry. The difference is the way in which they approach the problem. STFM selects a number of streamlines and finds their position at certain stations in the flow field, i.e. the geometrical variable in the radial direction is solved as a function of the geometrical variable in the axial direction and the stream function value. The SCM also finds the position of the streamlines, by using the cross-flow momentum equation, but it has to satisfy mass concervation in a separate equation. The MTFM, however, has a fixed grid, and the stream function values at every grid point are solved as a function of the two geometric variables. In this project MTFM was used.

4.1 Matrix Through Flow Method

The MTFM finds the stream function value as a function of the space coordinates of the flow region. See equation 4.1.

$$\psi = f(r,z) \qquad\qquad 4.1$$

Such a flow region consists of an infinite number of points where the governing equation needs to be applied to find the solution. A set of discrete points, also known as the grid, represents a simplification of this region. Using initial and boundary conditions, the equation can be solved iteratively along this grid. The MTFM combines the equations of continuity, momentum and energy into a single equation by introducing the stream function and thus ensuring the conservation of mass as an inherent property of the method. In the following section the basic derivation will be given. For more complete information on the algebraic manipulation involved, refer to Bosman et al (1974) and Moore et al (1987).

4.1.1 *Formulation*

From the conservation of momentum in the meridional plane, follows what is commonly called the radial equilibrium equation:

$$V_r \frac{\partial V_r}{\partial r} + V_z \frac{\partial V_z}{\partial z} - \frac{V_u^2}{r} = -\frac{1}{\rho}\frac{\partial p}{\partial r} \qquad\qquad 4.2$$

Conservation of mass is introduced by defining the axial and radial velocity components in terms of some scalar function that has the property that it forms a solution to the continuity equation. This function is called the stream function and is defined by equation 4.3.

$$\psi = \frac{\dot{m}}{2\pi} \qquad\qquad 4.3$$

The velocity components are defined in equations 4.4 and 4.5.

$$V_z = \frac{1}{r\rho}\frac{\partial \psi}{\partial r} \qquad\qquad 4.4$$

$$V_r = -\frac{1}{r\rho}\frac{\partial \psi}{\partial z} \qquad\qquad 4.5$$

The next step is to introduce the first law of thermodynamics in cylindrical coordinates:

$$\frac{1}{\rho}\frac{\partial p}{\partial r} = \frac{\partial h}{\partial r} - T\frac{\partial s}{\partial r} \qquad 4.6$$

To find the first term on the right hand side, differentiate the definition of total enthalpy (in terms of its static and dynamic components) with respect to r.

$$\frac{\partial h_t}{\partial r} = \frac{\partial h}{\partial r} + V_u\frac{\partial V_u}{\partial r} + V_z\frac{\partial V_z}{\partial r} + V_r\frac{\partial V_r}{\partial r} \qquad 4.7$$

Substitute equations 4.6 and 4.7 into equation 4.2 and simplify.

$$\frac{\partial V_z}{\partial r} - \frac{\partial V_r}{\partial z} = \frac{1}{V_z}\left[\frac{\partial h_t}{\partial r} - V_u\frac{\partial V_u}{\partial r} - T\frac{\partial s}{\partial r} - \frac{V_u^2}{r}\right] \qquad 4.8$$

Use the definition of the velocity components in terms of the stream function as given in equations 4.4 and 4.5 to find the final form of the equation:

$$\frac{\partial}{\partial r}\left[\frac{1}{r\rho}\frac{\partial\psi}{\partial r}\right] + \frac{\partial}{\partial z}\left[\frac{1}{r\rho}\frac{\partial\psi}{\partial z}\right] = S \qquad 4.9$$

S is the source term and is given by the right-hand side of equation 4.8. After some numerical experimentation, it was found that the radial components of velocity are large enough to make the formulation by Moore et al (1987) unstable. Subsequently, the formulation of Bosman et al (1974) was used and this led to a change in the source term as given by equation 4.9.

$$S = V_z\frac{\partial}{\partial r}(\rho r) - V_r\frac{\partial}{\partial z}(\rho r) + (\rho r)^2\frac{\partial h_0}{\partial\psi}$$
$$-\frac{\rho r T}{V_m^2}\left[V_z\frac{\partial s}{\partial r} - V_r\frac{\partial s}{\partial z}\right] - \frac{\rho V_u}{V_m^2}\left[V_z\frac{\partial}{\partial r}(rV_u) - V_r\frac{\partial}{\partial z}(rV_u)\right] \qquad 4.10$$

4.1.2 Numerical evaluation

The equations given in the previous sections are exact. If it were possible to solve them as they are, the solution to the axisymmetrical flow problem would be precise. Unfortunately the equation is a two-dimensional partial differential equation and no known closed form solution exists. The only other option is to discretise the equation nd use a computer to find an approximate answer that has the property that the numerical answer would tend toward the exact one, as the grid is refined. The grid approximates the flow field by defining r and z at

discrete points. This implies that each point in the interior, P, has four neighbours, conveniently called N, S, E and W. See figure 4.1.
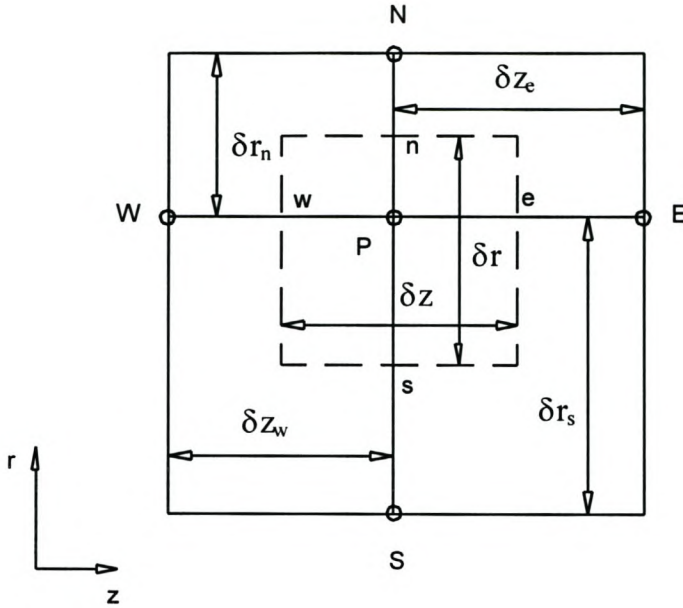
Figure 4.1: Nomenclature for the discretisation grid of Greyvenstein (1981)

First and second order derivatives were calculated with the discretisation method of Greyvenstein (1981). Appendix B gives a summary of the equations used in this method. After some algebraic manipulation, the equation was reduced to the following form.

$$A_P \psi_P = A_N \psi_N + A_S \psi_S + A_E \psi_E + A_W \psi_W + S \qquad 4.11$$

Where the coefficients are given by:

$$A_N = \frac{1}{\delta r_n \delta r} \qquad 4.12$$

$$A_S = \frac{1}{\delta r_s \delta r} \qquad 4.13$$

$$A_E = \frac{1}{\delta z_e \delta z} \qquad 4.14$$

$$A_W = \frac{1}{\delta z_w \delta z} \qquad 4.15$$

$$A_P = A_N + A_S + A_W + A_E \qquad 4.16$$

4.1.3 Interpolation

Although the discretisation method of Greyvensten (1981) shown in section 4.1.2 applies to non-uniform grids, the grid has to be rectangular. To accommodate this restriction, an interpolation method, as given by Harms (1995), was used. It is called the 5-point interpolation scheme and is shown in figure 4.2. The black dots and circles represent the original grid and the interpolated grid respectively. The existing, non-uniform, non-rectangular grid was used in a linear interpolation to find a new, still non-uniform, but rectangular local r-z grid. Harms (1995) has shown that this linear approximation does lead to the exact answer in the limit. It is obvious that this new, modified grid will coincide with the old one when the grid is rectangular.
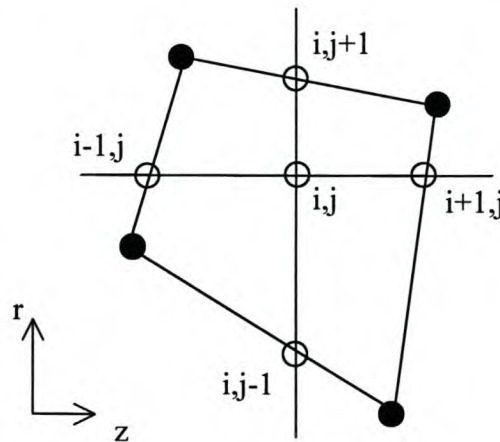
Figure 4.2: Graphical representation of the 5 point interpolation scheme by Harms (1995)

4.1.4 Initial and boundary conditions

The mathematical equation that describes the fluid flow in this turbomachine (equation 4.8) has an infinite number of solutions. In order to find a unique solution to the problem, initial and boundary conditions are specified.

The boundary conditions govern the flow at the top and bottom walls, as well as enforce a certain velocity distribution at the in- and outlet of the grid. From equation 4.3 the stream function value for the top streamline is known as this stream tube represents the full mass flow as given by the user as a design input.

The same principle is true for the bottom streamline, i.e. the stream function value at the bottom streamline is zero. At both the inlet and outlet the streamlines are forced to stay

parallel to the annulus. In terms of velocity components, this implies that the radial velocities at the inlet and outlet are zero.

4.1.5 Programming

The MTFM discussed in this chapter was implemented in a program called *Matrix*. This program was written in Borland Delphi and was compiled as an executable that will run on any Windows 95 based computer. The interface takes the user through the steps of generating a grid, setting initial conditions and running the simulation. To understand what the program does, it is useful to look at the algorithm:

➢ *Generate a grid*. The program, *Matrix*, ran a procedure that generated a grid and the user only had to adjust the number of grid points in different sections. This allowed the user to use rough and finer grids for preliminary and final investigations respectively. This approach not only saved time, but also eliminated useless designs. A simulation that does not work on a rough grid will most probably not work on a fine one.

➢ *Set boundary conditions*. The designer specified the mass flow. This information was sufficient to define the boundary conditions of the simulation: the bottom grid points (defining the lower streamline) represented zero mass flow and were subsequently zero, while the top grid points (defining the upper streamline) represented the full specified mass flow and was calculated from equation 4.3. From this equation, the relationship between the geometry and the stream function values followed: $\psi \propto m \propto A_{streamtube} \propto r^2$. The change in stream function value therefore decreased from the bottom to the top of the grid, as the grid was equally spaced in the vertical direction. Table 4.1 shows typical values of the stream function at the grid points. Notice that the first and last rows, as well as the first and last columns are boundary conditions.

r_{inlet}	Stream function values from inlet to outlet												
1.00	7.958	7.958	7.958	7.958	7.958	7.958	7.958	7.958	7.958	7.958	7.958	7.958	7.958
0.85	5.329	5.329	5.329	5.329	5.329	5.329	5.329	5.329	5.329	5.329	5.329	5.329	5.329
0.70	3.126	3.126	3.126	3.126	3.126	3.126	3.126	3.126	3.126	3.126	3.126	3.126	3.126
0.55	1.350	1.350	1.350	1.350	1.350	1.350	1.350	1.350	1.350	1.350	1.350	1.350	1.350
0.40	0.000	0.000	0.000	0.000	0.000	0.000	0.000	0.000	0.000	0.000	0.000	0.000	0.000

Table 4.1: Typical initial stream function values for flow through a parallel annulus at 50 kg/s with an inner radius of 0.4 m and outer radius of 1.0 m.

> *Set initial conditions.* Initial values for the stream function and enthalpy values were calculated throughout the grid. The non-boundary values shown in table 4.1 were the initial values calculated for this specific simulation.

> *Start loop*

♦ The algorithm checked to see whether the index had reached the blade section or not. When the index has reached the blade, work was done on the fluid by an addition of whirl as defined by the user. This change in whirl was linked to a rise in enthalpy through the Euler turbomachinery equation.

♦ Values for enthalpy and whirl where found through interpolation by using the fact that the stagnation enthalpy and the angular momentum stayed constant along a streamline, except through the rotor, where it increased due to work done on the fluid. This increase was affected through a user-specified addition of whirl. In general, the values of enthalpy and whirl were known at the stations upstream of the point where it was required to interpolate. A simple linear interpolation was used in this program.

♦ The new value of the stream function was found at a grid point by calculating the values of the coefficients. These coefficients are all a function of the geometry of the grid (see equations 4.12 – 4.16) and the source term (equation 4.10) is a function of known velocity values.

♦ Calculate error. Once the new value of the stream function was known, it was compared with the old value and the change expressed as a non-dimensional number:

$$error = \frac{\left|\psi_{old} - \psi_{new}\right|}{\psi_{top}} \qquad 4.17$$

Where ψ_{top} was the stream function value of the top streamline, which stayed constant.

> If the error was less than a certain value, the process was stopped and convergence achieved. If not, the process was repeated from the start of the loop.

> Velocity components were calculated from the final stream function values.

4.2   Test cases

Gannon et al (2000) used a number of test cases to authenticate their STFM code. Two of the test cases for incompressible flow presented in their paper were used to validate the MTFM code *Matrix*.

4.2.1   Test case 1: Non-swirling flow in a parallel annulus

The MTFM code *Matrix* was used to find the solution of incompressible, non-swirling flow of 50 kg/s through a parallel annulus with an inner radius of 0.4 m and an outer radius of 1.0 m. The maximum difference between the resulting axial velocity values and the analytical solution was 0.01 %. It confirmed that the MTFM code satisfied the conservation of mass and produced the correct velocity profile.

4.2.2   Test case 2: Actuator disc

In order to introduce tangential velocities into the flow problem, this test case simulated incompressible, swirling flow through an actuator disc in a parallel annulus with an inner radius of 0.4 m and an outer radius of 1.0 m . The actuator disc was placed in the centre of the flow field, perpendicular to the flow direction. The tangential velocity distributions up- and downstream of the actuator disc are given by equations 4.18 and 4.19 respectively with a = 6.0 s^{-1} and b = 6.0 m^2/s.

$$V_u = ar - \frac{b}{r} \qquad \text{(inlet)} \qquad\qquad 4.18$$

$$V_u = ar + \frac{b}{r} \qquad \text{(outlet)} \qquad\qquad 4.19$$

The axial velocity at the inlet inner wall was 10 m/s. When compared to the analytical solution given by Dixon (1978) the maximum error in the axial velocity profile was 0.88 % for the 2060 cell grid and occurred close to the inner wall on the inlet side. According to Gannon et al (2000) the simple actuator disc theory used to predict the velocity profiles in this test case was inaccurate close to the disc because of its disregard of radial velocities. Special care was therefore taken to set up the grid with sufficiently long inlet and outlet sections so that the velocity profiles shown in figure 4.3 were far upstream and downstream. These axial velocity profiles were also integrated numerically using the simple trapezium rule to find the mass flow rate at the inlet and outlet. The difference between inlet and outlet was 0.24 % and the average mass flow calculated by the MTFM differed from the analytical solution with

0.17 % for the 2060 cell grid. The numerical integration method used, has a global error of the order of the data interval squared, which translates to 0.17 %. These results confirmed that the MTFM solution satisfied the conservation of mass as the errors were within the range of accuracy of the numerical integration method.
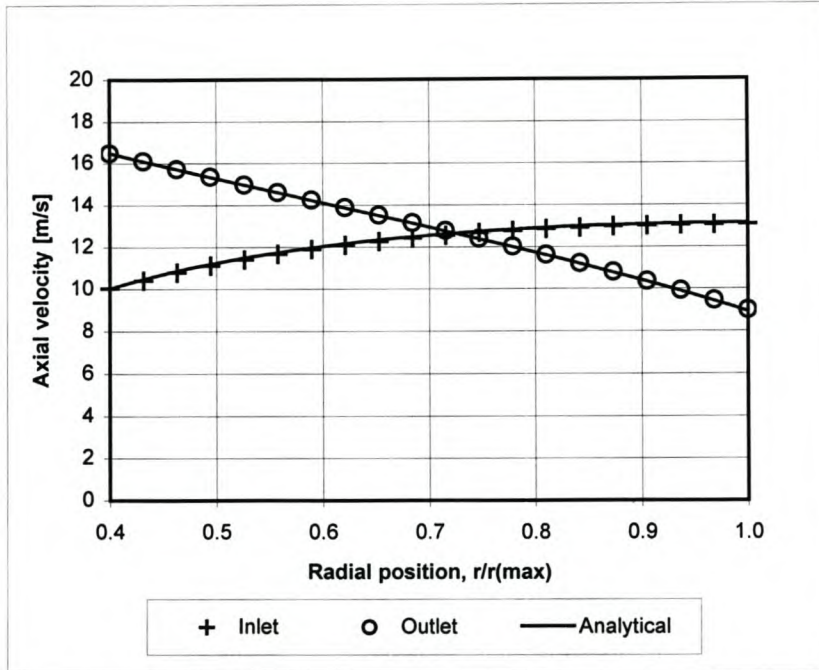
Figure 4.3: Inlet and outlet axial velocity profiles of incompressible flow in a parallel annulus through an actuator disc

To ensure that the numerical solution would converge to the exact analytical one as the grid was refined, three simulations with varying number of grid points were done. Table 4.2 shows how the error decreased from 8.45 % to 0.88 % for the inlet axial velocity profile and from 1.43 % to 0.47 % for the outlet axial velocity profile as the number of grid points increased from 115 to 2060.

#	Number of grid points	Convergence tolerance	Maximum error [%]	
			Inlet	Outlet
1	115 (23 x 5)	1e-6	8.45	1.43
2	945 (63 x 15)	1e-6	1.49	0.66
3	2060 (103 x 20)	1e-6	0.88	0.47

Table 4.2: Maximum error at inlet and outlet of flow through an actuator disc with increasing grid refinement

4.3 MFF simulation with MTFM

The grid shown in figure 4.4 is a schematic of the one used in the numerical analysis of the mixed flow fan. Note that a much finer grid was used in the final calculation. The generic MFF grid had a number of distinct regions:

➢ *Inlet*. The inlet section was the constant diameter part of the grid on the left-hand side where the fluid enters. It had a rectangular, uniform grid. The inlet section was made long enough so that any upstream effects because of the fan can be calculated, without the initial inlet profile being influenced.

➢ *Region before the blade*. In this section, the air is already starting to move radially outward due to the conical shape of the annulus and the nose cone. The aim was to deflect the flow in such a way that the inlet flow to the rotor was uniform. Note that the grid in this region is curvilinear and non-orthogonal.

➢ *Blade*. Up to this point, no work had been done on the flow. The blade section added energy to the flow through the addition of whirl as defined by the designer.

➢ *Region after the blade and outlet*. The exit region was kept a constant diameter to prevent recirculation areas of forming – something this implementation of the MTFM could not handle. The length of the exit of the grid was such that the velocity profiles at the end were not a function of the axial distance.
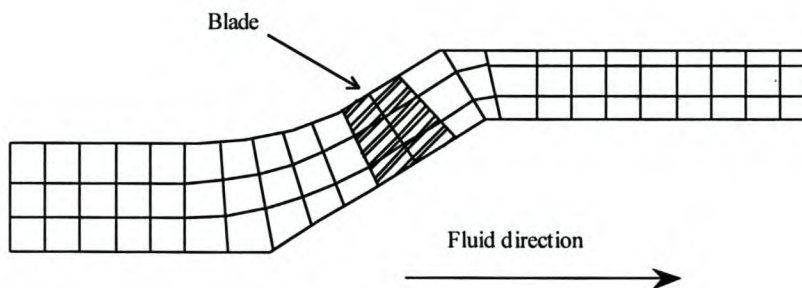
Figure 4.4: Schematic of the mixed flow fan grid

CHAPTER 5

MANUFACTURING

"Those who are enamoured of practice without science are like a pilot who goes into a ship without rudder or compass and never has any certainty where he is going. Practice should always be based upon a sound knowledge of theory."

- Leonardo Da Vinci

The following chapter gives a brief overview of the design and manufacturing of the different components of the MFF. In addition it underlines and explains the influence of the design geometry on the manufacturability and vice versa. It is obvious that the aerodynamic design cannot be contained in its own reality and has to be developed into a physical machine. Knowledge of the processes involved will greatly facilitate this. It has to be mentioned that only one of these fans was made and the manufacturing processes involved were subsequently geared toward this.

5.1 Components of the mixed flow fan assembly

The MFF assembly has two main sub-assemblies: the fan with its components and the casing sections that form part of the fan test tunnel. Each of the components of these two sub-assemblies is discussed separately in the following paragraphs.

5.1.1 Casing sections

All channel sections where made from 1.6 mm sheet metal with 6 mm flanges. The truncated cones were developed onto a flat surface, cut out and arc welded to form the conical sections. The flanges were rolled from 6x50 mm flat mild steel, machined round on the inside and welded to the annuli. The purpose of the flanges was twofold. They connected the various sections as well as provided the stiffness and shape of the channel sections. For the conical section

Figure 5.1: Photo of welded casing section

in which the fan rotated, this was especially important, as the tip clearance had to be minimised.

5.1

5.1.2 Hub

The basic shape of the hub was cast in LM4 aluminium (deemed adequate for this purpose by the expert at the foundry). This led to a great saving on material and reduced the machining time. The casting was machined on a lathe, fastened on an index table and two sets of holes drilled: one set for the fastening screws and the other set was reamed for dowels.
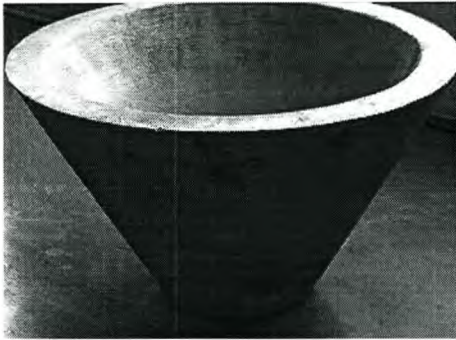
Figure 5.2: Photo of the cast hub

Figure 5.3: Photo of the machining of the MFF hub

These dowel holes were provided for the correct positioning of the blade as well as to prevent the blades from turning during operation. See Appendix C for the FEM analysis on the hub.

5.1.3 Blades

Eleven multiple circular arc (MCA) blades were cut on a CNC milling machine. In the introductory paragraph it was mentioned that this was a one-off design and therefore it was more cost-effective to machine them individually rather than machining a mould with which to cast them. The cutting of the blades can be broken into a number of steps.

➤ *Generate a blade model.* A three-dimensional blade consists of a number of profiles that are stacked from root to tip. These profiles were generated according to the specifications of the aerodynamic design and their shape imported point by point into *AutoCAD*. This drawing was exported to *Pro-Engineer*, where a solid model of the blade was made.

➤ *Generate cutter paths.* Fortunately, modern CAD/CAM technology eliminated most of the tedious work usually associated with programming CNC machines. *Pro-Engineer* has advanced software that generates these paths in pre-set ways, specified by the operator. The generation of these cutting paths required frequent input from an expert operator and therefore a third party operated the software and programmed the CNC machine to cut the blades.

> *Design a jig that would locate the blade on the machine bed.* The block of material from which the blade was cut, was bolted to the jig and held in position by two dowels, while the other side was simply clamped down with the bottom of the block flush with the lathe bed. Figure 5.4 shows the dowels that fit into the blade. A bolt passes through the centre and fastens the blade to the jig (see figure 5.5).
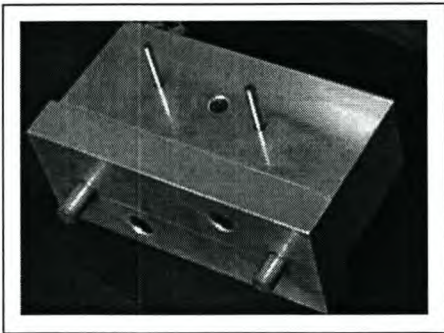
Figure 5.4: Photo of the front view of the jig
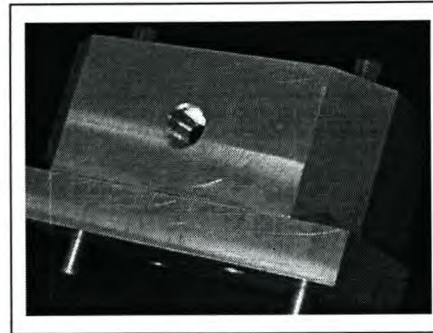
Figure 5.5: Photo of the rear view of the jig

> *Prepare material for machining.* The blades were cut from LM6 aluminium. This material was preferred because of its high degree of machinability, which allowed for a higher feed rate and a better surface finish. The fastening mechanism of the block of material from which the blade was cut had to withstand the forces induced by the machining operation. This was especially relevant when the material was turned around to cut the second surface, as the jig was unable to withstand the downward forces as a cantilever. The raw block of material was subsequently extended to leave material at the end where it could be clamped down. It was important to mill the block to the exact height of the jig to avoid residual stresses while machining. The end surface on the jig side was also milled to be perpendicular to the top and bottom. Three holes, two of which were for the dowels and one for the fastening screw, were drilled on the machined end.

> *Machine the blade.* The blade was cut from a block of material, much of which had to be machined away before reaching the blade shape. The first step was to do a rough-cut, where, at the expense of accuracy, the material was taken away as quickly as possible. This was followed by a finishing cut to provide the accuracy and surface finish required for the final product. The programmer of the CNC path had to specify in the program that runs the cutting process, among other things, what the different cutting and feeding speeds

needed to be. These parameters were not only a function of the operation (rough- or finishing cut), but also the material. In order to check the CNC program, the blade was initially cut from wood. Table 5.1 gives a summary of the CNC lathe settings.

Settings	Wood		Aluminium	
	Rough	Final	Rough	Final
Spindle speed	4000	4000	4000	4000
Feed speed	3600	3600	1500	1500
Side step (mm)	4	0.2	2	0.2
Down step (mm)	4	0.2	2	0.2
Type of path	omni-directional	y-direction	omni-directional	y-direction
Tool	12 mm ball nose cutter			
Machining time	3 hours	3 hours	6 hours	4 hours

Table 5.1: Essential parameters in machining a fan blade on a CNC milling machine

The blades were fastened onto a cone and then mounted inside a conical annulus. Thus, both the root and tip surfaces of the blade had to be curved to fit their position on the cone hub and in the cone annulus. It was therefore necessary to find these curves. When a plane cuts a cone at a certain angle, a curve was formed along the intersection. This curve was a function of the angle at which the plane cuts the cone and can, depending on the eccentricity, be an ellipse, parabola or hyperbola. Eccentricity is defined as:

$$e = \frac{\cos(\delta)}{\cos(\gamma)}$$

5.1

The symbols δ and γ are the angles at which the plane cuts the cone, measured relative to the cone's axis, and the semi-cone angle respectively. It is now possible to classify the type of curve resulting from this cone-plane intersection.

e	δ (γ=30°)	Type	Equation
<1	>30°	ellipse	$\frac{x^2}{a^2} + \frac{y^2}{b^2} = 1$
=1	=30°	parabola	$ax^2 + bx + c = y$
>1	<30°	hyperbola	$\frac{x^2}{a^2} - \frac{y^2}{b^2} = 1$

Table 5.2: Conic section classification based on eccentricity.

Through inspection, it was found that the curve at the root of the blade did not deviate enough from a straight line to justify the effort involved in considering this during machining: the jig would have to be machined to have a convex surface that has to mate with the concave one prepared on the rough material. The gap at the leading and trailing edge of the root was subsequently filled with body putty. The tip, however, had to have a curved surface in order to fit into the annulus. It has been mentioned that the surface cut on the CNC machine at the tip was flat and the curve at the tip needed to be some elliptical curve. There are two methods to attain the desired profile: calculate the curve needed on the blade tip and use a template to file it to the correct shape, or assemble the fan and mount it on a lathe to be machined at the desired cone angle. Although the latter method was used, the curve was still calculated to see how much it deviates from a straight edge.

Due to the blade twist, the tip of the blade was at a 45° angle to the cone axis. This implied that an ellipse was formed, requiring the values of a and b for a solution.
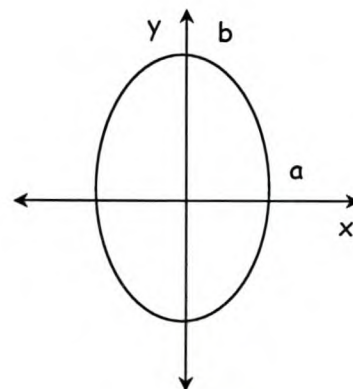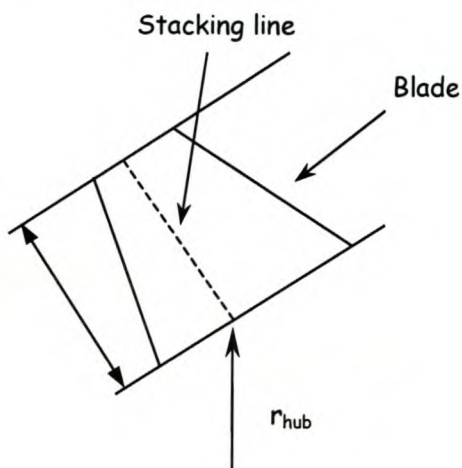
Figure 5.6: Schematic of blade geometry   **Figure 5.7: Conical section**

The variable, b, as shown in Figure 5.7, was known from geometry as the maximum radial distance from the axis of rotation, i.e. the radius of the point on the line around which the blade profiles had been stacked. The eccentricity of an ellipse is also uniquely defined in equation 5.2, leaving a as the single variable to be solved for.

$$b = r_{hub} + h\cos(\gamma)$$ 5.2

$$e = \frac{\sqrt{a^2 - b^2}}{a}$$ 5.3

Rewrite equation 5.3 in terms of b and e.

$$a = b\sqrt{(1 - e^2)}$$ 5.4

With a and b known, the designer simply had to find the applicable set of x-values that would describe the curve formed where the blade cut the annulus.

5.1.4 *Assembly*

The assembly of the fan and annular parts was straightforward. The blades were bolted onto the hub and held in position, at the correct angle, by a dowel. The blade was held to the jig with two dowels and it was one of these dowels that now position it. In order to simplify the machining of the hub, only one of these dowels was used in the location of the blade.

In order to have a small as possible tip clearance, the final assembly of the fan and annular sections, needed to be adjustable in some way. For this reason there was a gap between the conic section in which the fan rotates and the parallel annulus in which the motor was mounted. A wooden ring acted as a spacer, which was custom made according to the final dimensions of the assembly. Another means of adjusting the tip clearance was the use of a spacer, custom made, between the hub and bearing (in front of the torque transducer).

5.2   Design/Manufacturing interface

It is obvious that the design influences the manufacturing, but it is not always recognised that the communication is, and should be in the other direction.

The choice of a conical geometry over a spherical one did not only have aerodynamic implications, but also affected the manufacturing. It was far easier to cast and machine a conical surface, than a spherical one. This simplified the making of the hub significantly.

The blade had to be fixed to the hub in some way. Traditional methods included having a specially designed blade root that was held in place by clamping it between the two halves of the hub. In the MFF the blade was bolted onto the hub. This works quite well, except that there had to be enough space for a hole to be drilled and tapped into the bottom of the blade. The designer had to either add an insert to strengthen the blade or choose a profile that was thick enough to hold the blade. The fan design in this project had blades that were fat enough

to accommodate the bolt. The addition of an extra material on the end of the blade may have lead to machining complications. Another option was to machine the fan, both hub and blades, from one precast block of material. This would have eliminated the problem of blade roots and fastening, but called for more complex machining. The blades used in this project were longer than compressor blades would be and most cutting tools would not be able extend that far into the material. There may also have been stiffness problems while machining.

The designer had to choose a desired exit velocity profile. This choice did have implications on the use of material and machinability. The size of the block of raw material was a function of the twist of the blade, which in itself depended on the outlet velocity profile. Due to the free vortex outlet velocity profile chosen for this blade and the subsequent twist, the ratio of material removed to total raw material was high.

<center>

CHAPTER 6

EXPERIMENTAL WORK

</center>

" I am tired of all the glory, I want to get back to work. "

<div align="right">

- Thomas Alva Edison

</div>

It was imperative to validate the design method through thorough testing. The experimental investigation included a standard fan test and a more in-depth probe evaluation. The first was used to assess the overall performance of the fan in the form of a pressure rise/volume flow and an efficiency/volume flow relationship respectively. This is the information typically required in practice to match the fan with the system in which it is to be used. Throughout the design process, many assumptions about the above-mentioned properties were made, many of them based on empirical studies not relating directly to MFFs. The probe test was useful to compare calculated flow distributions with the measured ones. In this chapter the set-ups needed to make the necessary measurements are explained and a summary of the results are given.

6.1 Basic layout of experimental set-up

Figure 6.1 shows a schematic of the experimental set-up. Air flowed from left to right, entering the ellipse-shaped bellmouth through the small diameter inlet section, expanding into the fan section, and eventually leaving through the constant diameter exit casing.
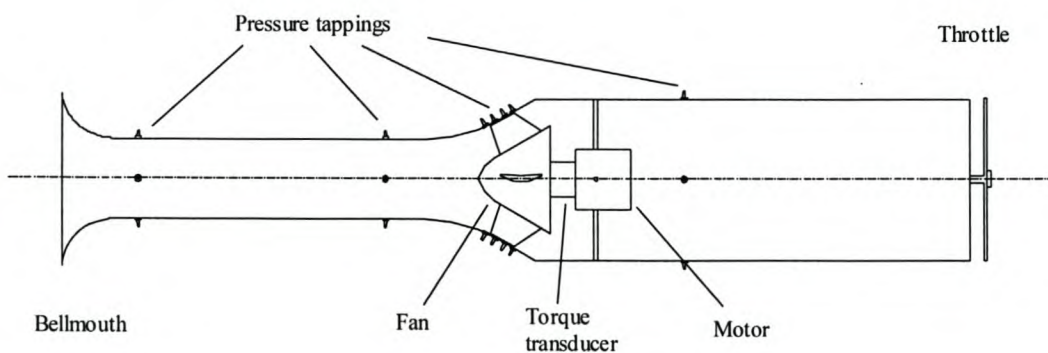
Figure 6.1: Schematic layout of mixed flow fan test set-up.

<center>6.1</center>

A glance at the schematic layout of the test facility shows a number of distinct elements. The first is the shape and size of the inlet section. In accordance with the BS 848 standard, the volume flow rate was calculated as a function of the static pressure just downstream of the inlet and the discharge coefficient associated with the bellmouth. The accuracy with which the volume flow rate could be measured was therefore a function of the accuracy with which the static pressure could be measured. If the difference between the static pressures measured at low flow and the static pressure measured at high flow is small, any errors in data acquisition would have been amplified which would have resulted in a large discrepancy in the volume flow rate calculation. The pressure for a given volume flow rate could be expressed as a function of the annulus diameter (equation 6.1). For a constant value of the coefficient C, it was obvious that in order to increase the sensitivity of the measurement, the diameter had to be decreased.

$$\Delta p = p_{static} = C\left(\frac{Q^2}{D^4}\right), \text{ where}$$

6.1

$$C = \frac{8}{\pi^2 \alpha^2 \rho}$$

The term α was associated with the inlet losses at the bellmouth. According to the BS 848 code, it is defined as shown in equation 6.2. The symbol V is the average velocity of the air in the part of the casing where the static pressure is measured.

$$\alpha^2 = \frac{\left(\frac{1}{2}\rho V^2\right)_{actual}}{\left(\frac{1}{2}\rho V^2\right)_{ideal}}$$

6.2

Table 6.1 shows a comparison between a reference diameter and the one used in this project and it is apparent that the range of pressure measurement is substantially higher for the smaller duct.

Diameter [m]	Δp [Pa]	mm H_2O
0.630	24.7	2.53
0.316	390.2	39.90

Table 6.1: Comparison of measured bellmouth static pressures for two different pipe diameters. (Q = 2.0 m³/s, α = 1.0, ρ = 1.2 kg/m³, g = 9.8 m/s²)

The second feature worth mentioning is the diffuser section leading into the fan. The diffuser casing was designed to merge tangentially with the fan casing, forming a transition from the inlet section. Care was taken to limit the expansion in order to keep the boundary layer from separating. Fortunately, as soon as the flow reached the nose cone, it was accelerated into the rotor, which created a favourable boundary layer pressure gradient. The other elements of the set-up include a torque transducer that connected the fan and the electric motor and a throttle plate that was used to induce a pressure drop in the system, thereby enabling the performance curve to be measured from low (close to zero) to high volume flows.

6.2   Pressure measurement

Apart from the calculation of fan power, all other fan performance properties were monitored through pressure measurement. The following paragraph gives a brief overview of the transducers and other relevant equipment that was used to determine pressure, whether it be static or total.

6.2.1   Transducer

Horowitz et al (1995), define a transducer as a device that converts some physical quantity to some or other (measurable) electrical quantity. The pressure transducers used in this project where all made by Hottinger Baldwin Messtechnik (HBM) The output was a small electrical signal proportional to the difference in pressure between the two pressure tappings on the instrument. See Figure 6.2.
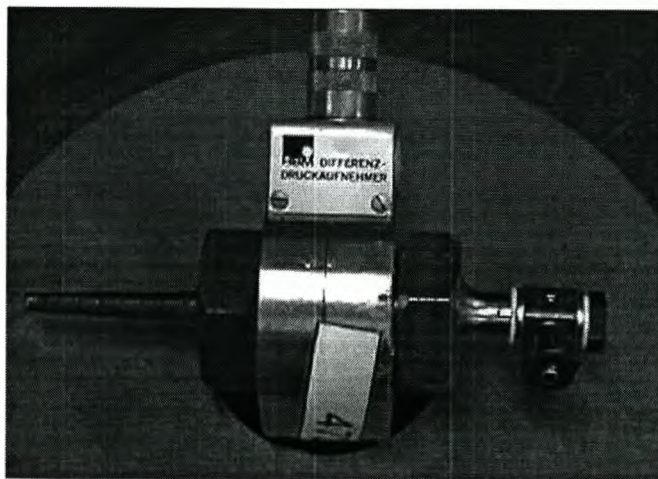
Figure 6.2: HBM pressure transducer

This signal from the transducer was too small for direct use and had to be amplified. Subsequently, the transducer was connected to a bridge amplifier, also made by HBM, that was able to sense small changes in the input signal and enlarge them to the more measurable millivolt range. See Figure 6.3.
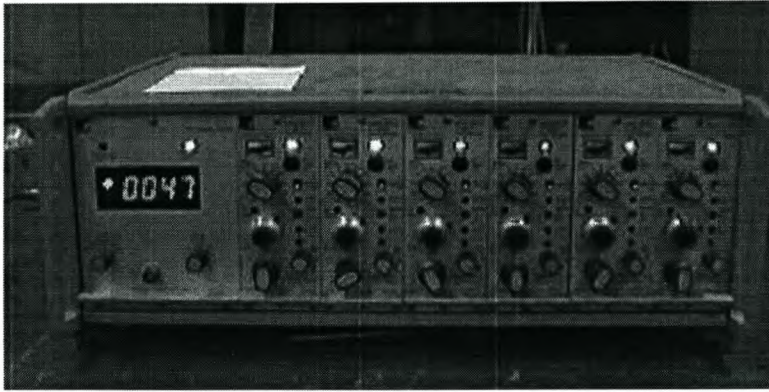
Figure 6.3: HBM bridge amplifier with six channels.

Because the signal from the bridge amplifier was in millivolts, the transducer/amplifier set-up had to be calibrated to find the relationship between measured volts and pressure in Pascal. The reference instrument used was a Betz water manometer.

6.2.2 Pressure selection

The number of pressure tappings usually exceeds the number of available pressure transducers. To overcome this problem, a pressure point selection device was used. The device enabled the operator of the fan test facility to use one transducer by rerouting any one of the input pressures through the same transducer. In this project a Furness FCO 91 MkII Selection Box was used (see Figure 6.4).

Figure 6.4: Furness FCO 91 MkII pressure selection box

This box had a number of operation modes. The first was manual, where the user had to select the channel (pressure point) using switches on the box. The second was the so-called BCD input. This was for remote computer selection. A digital output signal, in the form of a word of data, was generated by the computer and supplied to the selection box via a cable. Data acquisition software was written by this author for this set-up which used this mode of selection to automatically select the channels. More on the computer set-up later. Strohmaier (1997) explained the use of the BCD mode in detail. He also discussed the algorithms needed to change a decimal number to a so-called offset decimal, the numbering system used by BCD data transfer. The other modes of operation of the pressure selection box included remote triggering and timed selection. These modes were not used in this project.

6.3 Torque and speed measurement

In order to measure the power that the fan absorbs, a torque transducer, manufactured by HBM, was mounted between the shaft of the electric motor and the fan. This meant that the transducer senses only the torque needed by the fan and therefore did not take into account other frictional and slip losses in the motor. Fortunately the performance of the motor was of no importance and the reading of the transducer was sufficient. As with the pressure sensing, this transducer also produced a signal directly proportional to the physical property it was monitoring, i.e. torque. Again the signal had to be amplified and again a HBM bridge amplifier was used.

The speed of fan is controlled with a Yaskawa CIMR G3E4011 frequency inverter. This piece of equipment could supply an electrical device, in this case an electrical motor, with power at a given frequency. Although the rotational speed of the motor was a linear function of the input frequency, it could not be accurately calculated due to the fact that there was always some slip in the motor. Using a simple hand-held tachometer, the rotational speed was calibrated as a function of the input frequency. These tests have shown that the correlation between speed and frequency was not noticeably affected by fan loading.

6.4 5-hole probe

It has been mentioned in the introduction that the validation of the design method required more that just the overall fan performance. Knowledge of the velocity profiles into and out of the fan would greatly facilitate the investigation of the method under scrutiny and therefore an instrument was needed that was able to measure the flow vector (size and orientation) at a

point in 3D space. Such instruments can be divided into two categories: the pitot type probes and hot-wire anemometers. The latter are highly sophisticated and are able to make in-time turbulence measurements, but have the disadvantage of requiring advanced hard- and software. A probe of the first type was available and fairly simple to use. In the next few paragraphs the working of this probe and the tests that were carried out to ensure that it was still reliable will be explained.

6.4.1 Measuring with the 5-hole probe

In a medium velocity flow field (Ma < 0.3) the velocity can be derived from the knowledge of the static and stagnation pressures at a point. This simple relationship, often measured with a pitot tube, contains no information on the direction of the flow and the operator of the probe has to be aware of this. For cases where the direction is also an unknown, a probe was devised that is able to indicate both the direction and magnitude of the flow vector. This probe has a centre hole and an array of four holes on the outside drilled at an angle to the axis of symmetry. Figure 6.5 shows a schematic drawing of such a probe and the definition of the orientation of the set of axis relative to which the flow angles are measured. The flow angles are shown in the positive direction. These definitions of the positive angles correspond with the so-called right hand rule.
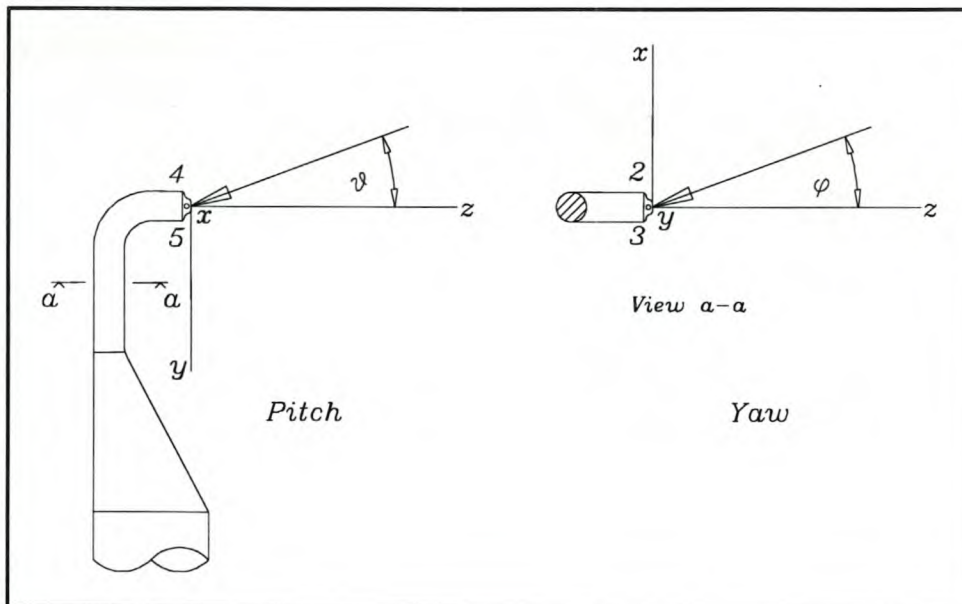
Figure 6.5: Positive pitch and yaw angle conventions. Taken from Strohmaier (1997).

Similar to a pitot tube, where a simple Bernoulli relation is used, the 5-hole probe also relies on some form of relation between static and stagnation conditions to find the flow properties.

But because it is more sensitive to manufacturing errors, it is not possible to find an analytical solution as is the case with a pitot tube, and therefore has to be calibrated. Strohmaier (1997) explains in detail the working of the probe and how it is calibrated. He also supplies the calibration maps with which the flow vector can be solved.

Each of the holes of the 5-hole probe was attached via a plastic tube to a HBM pressure transducer, which was in turn connected to a channel in the HBM bridge amplifier. The readings were monitored by a computer. The pressure values at each of these holes were then used to calculate the pitch and yaw coefficient from which the flow vector could be solved using the calibration maps. Note that the cone of operation of the probe is from $-30°$ to $+30°$ for both pitch and yaw. Whether the probe could still operate beyond this point was not known; Strohmaier's calibration, however, only spaned this range.

6.4.2 Probe verification

The probe is a small, sensitive instrument that is made of stainless steel tubing with a brass tip. Any damage to surfaces in which the holes are drilled, or leakage in the plastic tubes that run from the holes would have rendered the instrument useless. The purpose of the probe verification was to test the probe under controlled conditions to find out if the pre-set angles correlate with the calculated (calibrated) values. Figure 6.6 shows a schematic of the test facility used to test the probe

Air was vented from a 1.4 MPa reservoir through the ejector to atmosphere. The subsequent negative pressure (relative to atmosphere) in the ejector sucked the air in through the stagnation chamber, test section and nozzle, and blew it out through the exit duct. The controlled conditions were achieved because the nozzle was choked, keeping the upstream mass flow constant irrespective of any back pressure fluctuations at the exit of the nozzle. In an incompressible flow domain, the velocity distribution in the test section only depends on the mass flow and the geometry of the test section, both of which stay constant. If the back pressure should change, which does for example happen as the reservoir blows down, the shock simply moves up or down in the nozzle. Obviously there is a limit that should be avoided: when the pressure in the reservoir is not high enough to induce choked flow.
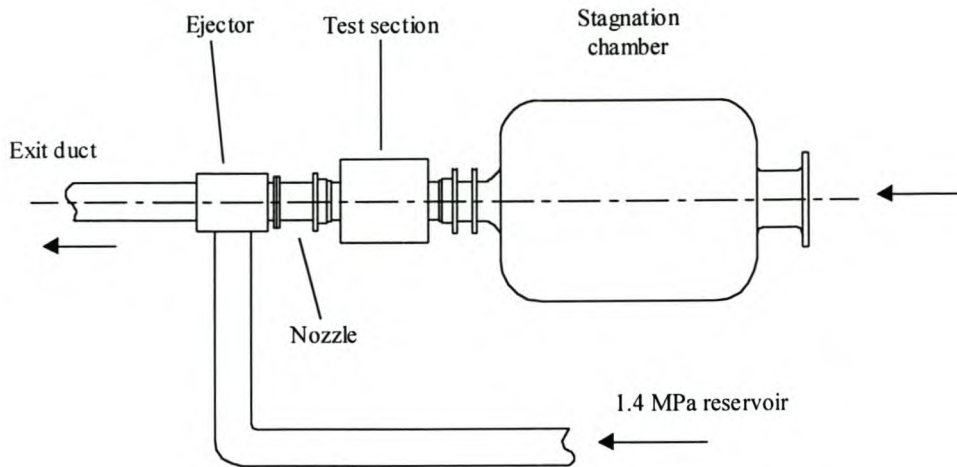
Figure 6.6: Schematic of probe test facility

The gasdynamics laboratory at the University of Stellenbosch has a number of nozzles that are designed to induce a certain Mach number in the test section. For this test a nozzle rated at Ma = 0.115 was used. This translates to a velocity of 39.5 m/s (γ = 1.4, R=287 m^2/s^{2}K, T=293K) as seen by the probe. Both the stagnation chamber and the test section had pressure tappings with which the stagnation and static pressures over a contraction could be measured. The difference between these pressures was used in the Bernoulli equation (flow was incompressible, the transition from stagnation chamber to test section was aerodynamically designed, the flow was accelerating) and the velocity seen by the probe found to be 39.8 m/s (Ma = 0.116). This confirmed the nozzle calibration.

The next step was to set the probe at certain known pitch and yaw angles. On the block containing the test section, surfaces had been machined on which the probe mounting could be fastened to set the probe in a known orientation in space. See figure 6.7. The first problem was to find the probe zero, i.e. zero pitch and zero yaw, and mark this point on the probe mounting. This was an iterative process that started with a visual setting of the probe followed by small adjustments according to the measured values. Once the zero was found, the needle indicating the yaw angle was set to zero and fastened relative to the probe. The probe was now set at different values of pitch and yaw. Table 6.2 and 6.3 shows the results of the probe verification.
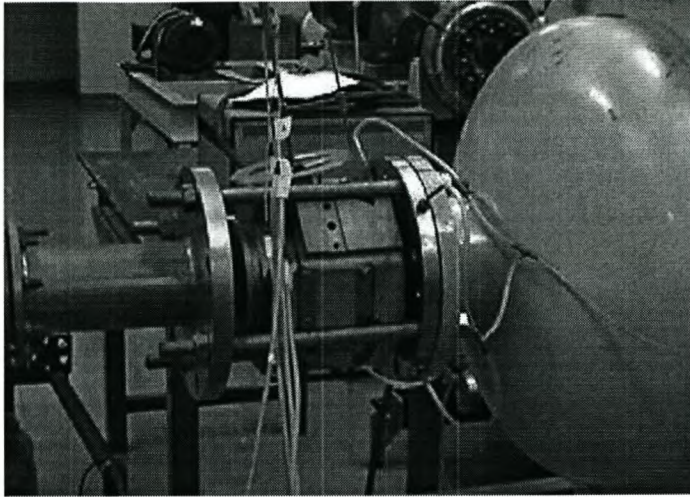
Figure 6.7: Photo of probe in test section

Nominal [°]		Measured [°]		V [m/s]
Pitch	Yaw	Pitch	Yaw	absolute
0	-20	-6.9	-19.2	36.8
0	-10	-6.8	-9.9	40.6
0	0	-6.9	-0.2	40.6
0	10	-7.3	10.4	40.4
0	20	-7.3	19.8	36.4

Table 6.2: Results of probe verification for nominal zero pitch

Nominal [°]		Measured [°]		V [m/s]
Pitch	Yaw	Pitch	Yaw	absolute
10	-20	2.9	-18.6	37.7
10	-10	2.9	-9.6	42.2
10	0	3.0	0.3	41.0
10	10	2.8	10.5	41.2
10	20	2.7	19.7	36.9

Table 6.3: Results of probe verification for 10° nominal pitch

It seems that the probe was able to detect the yaw accurately: the average error was 0.3°. The measurement of pitch showed a consistent 7° error, which would suggest that it was rather an offset than an inaccuracy. This assumption was confirmed with the second set of readings shown in table 6.3. With this offset in mind, the average error was 0.2°. The tables also contain the absolute value of the velocity as measured by the probe. After the velocity was calculated using the calibration maps, the effect of probe blockage had to be taken into account. The calculated value was 4.8 % and would therefore have caused a 4.8 % increase in the value of the velocity due to the presence of the probe. Although the maximum deviation from the actual value (39.5m/s) was 8.0 %, the maximum error in the –10° to 10° band for a zero nominal pitch was only 2.8 % and for the 10° nominal pitch was 6.8 %. The average value of these readings only deviated by 0.3 %.

Although the probe was tested in the velocity range between 30 m/s and 40 m/s and the velocity range in which it was used for the fan test was between 5 m/s and 20 m/s, the performance of the probe should not be effected too much as Strohmaier (1997) did his calibration at a nominal freestream velocity of 15 m/s. In conclusion, it appeared that the probe worked satisfactorily and that Strohmaier's calibration was still valid.

6.5 Experimental procedure

As mentioned before, there were two distinct sets of data associated with the fan. The first set described the overall performance including the pressure rise/volume flow characteristics. These characteristics were calculated using only the static pressure behind the bellmouth, in front of and behind the rotor and also the measured torque. All the pressures were measured with a single transducer using the Furness Selection Box to switch between the various pressure tappings.
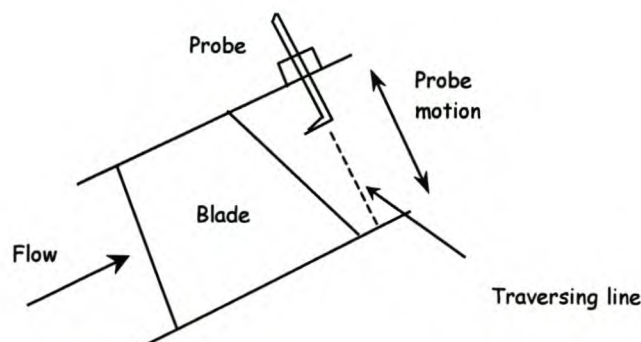
Figure 6.8: Diagram of the experimental set-up showing the probe traversing line.

The second set of data was measured with the 5-hole probe behind the fan. Figure 6.8 shows a diagram of this set-up. The traversing line of the probe was kept perpendicular to the casing and therefore also the passage. In order to measure within the cone of influence of the probe, the yaw angle was set to 40°. For this set of data, five pressure transducers were used. In the next paragraph the algorithm used to test the fan will be discussed.

6.5.1 Data acquisition algorithm

The algorithm used in this experimental evaluation is shown in figure 6.9. At the start of the procedure, a pressure point was selected and a signal sent to the selection box to switch the correct valve. The pressure was monitored until the value stabilised and the relevant average was calculated. This wass done by sampling n values and comparing their average with another set of n sampled values. If the difference between the two averages was sufficiently small, the average of the two averages was taken as the correct pressure reading. If not, the average of a new set of n values was compared to the previous average until stability was reached. The algorithm continued with this loop until the specified number of pressure points had been read. Torque was monitored in a similar manner to the pressure, after which the probe readings could be done if required. In figure 6.9 the *Get pressure reading* and *Get torque reading* are written between brackets to indicate a sub-loop. This whole process could be repeated for any number of throttle settings.

6.5.2 Hard- and software

A personal computer was used in the data acquisition process. The software was written by this author specifically for fan test applications and follows the algorithm mentioned in the previous paragraph. The program, written in Delphi 4.0, was called *FANTEST* and ran as an executable file in a Windows 95 (or equivalent) environment. The hardware used, included a Pentium II 400 MHz personal computer equipped with an Eagle Technologies PC30G data acquisition card. The card had a number of analogue to digital (AD), digital to analogue (DA) and digital input/output channels. The AD channels were used to convert the sampled data to a digital number that was stored on the computer. The digital output channels were used to address the Furness Selection Box.

The integrity of the data obtained by the program strongly depended on the way in which the stability of the monitored property was assessed. The first important factor was error, where error was defined as quantity associated with the change in the monitored value relative to the

previous one. The monitored value in this case is the average of every n values read. The error was often defined as a non-dimensional number as shown in equation 6.3.

$$error = \left| \frac{old - new}{old} \right| \qquad\qquad 6.3$$

The only problem with this formulation was that the strictness of the limiting error imposed by the user did not stay constant over the range of different values read. This problem was most apparent at values close to zero. For this reason an alternative definition of the error quantity was proposed in equation 6.4.

$$error = \left| old - new \right| \qquad\qquad 6.4$$

Because this definition of error had a dimension, it makes sense to calculate it in the SI-unit of the property that was monitored. In this way, the convergence accuracy was not a function of the read value and the user could specify a tolerance that makes sense in terms of the property measured. The second important factor was the sampling frequency. As explained earlier in this chapter, the relevant property (e.g. pressure or torque) was monitored by a transducer which in turn sent a continuous analogue signal (in millivolts) to a data acquisition card in the personal computer, where it was converted from an analogue to a digital signal at a given frequency called the sampling frequency. The digital signal was therefore not continuous, but merely represented a sample of the original analogue signal. In the second event in the algorithm shown in figure 6.9, n consecutively sampled values were averaged and compared to the previously calculated average of n values. When the sampling frequency was very quick relative to the general frequency with which the signal changes, the averages calculated did not represent the real average of the signal and the two values, when compared, may even be close enough to indicate a stable signal. Either a slower sampling rate or a larger value for n was used to solve this problem, but unfortunately both increased the time required to take a reading. The sampling rate, sample size (valueof n) and limiting error were user options in *FANTEST.*
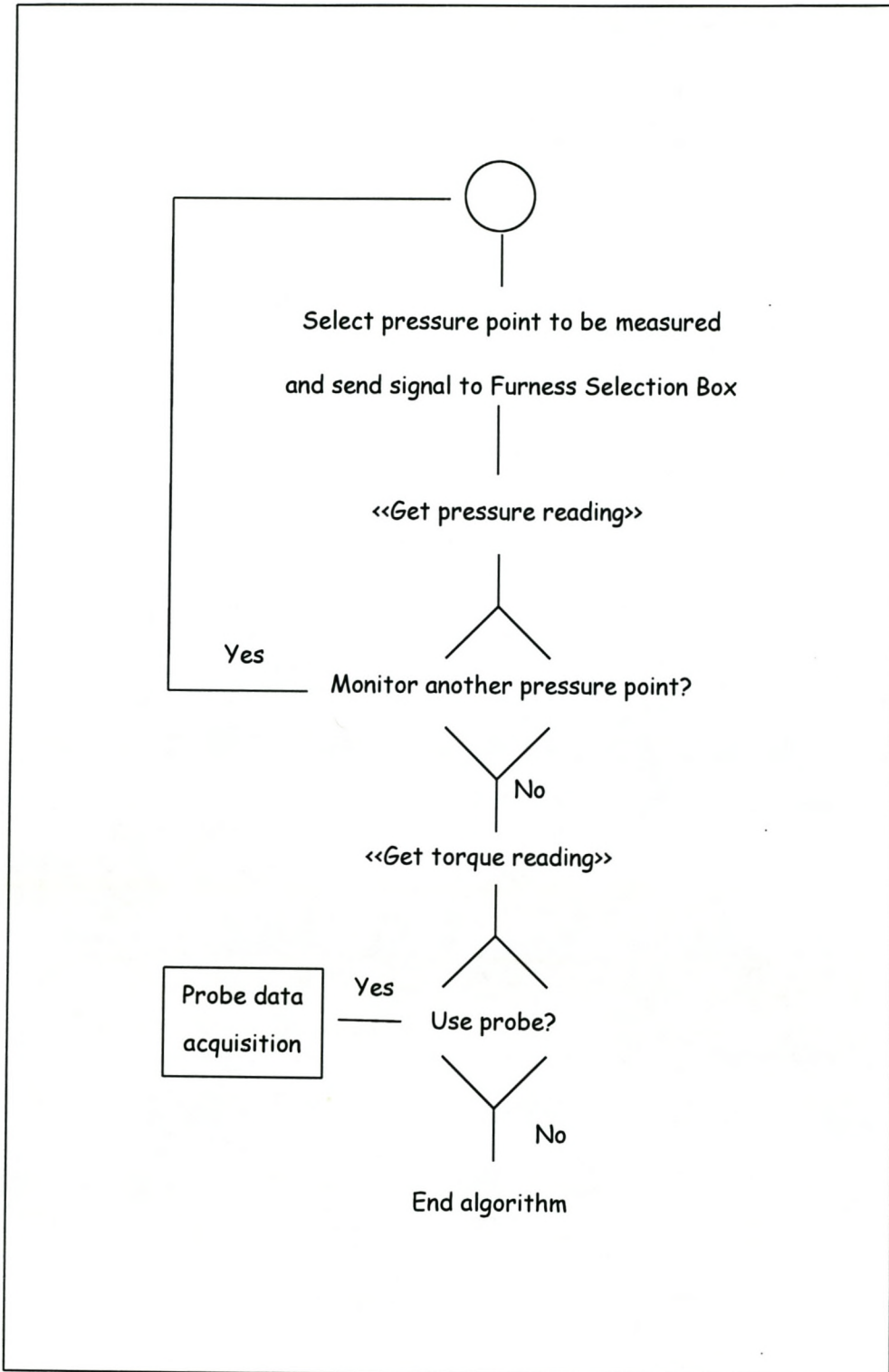
Figure 6.9: Flow chart of data acquisition algorithm

6.6   Experimental results

6.6.1   Overall characteristics

The overall characteristics are the most useful indication of a fan's performance from a practical point of view. They contain information on the flow resistance the fan can overcome as a function of volume flow rate as well as how efficiently the fan can do this. Usually the ability of the fan to overcome this resistance is quantified in terms of a change in static pressure across the fan. Because the mixed flow fan has different inlet and discharge areas and therefore different dynamic pressures at the inlet and discharge, it was difficult to relate the change in static pressure over the fan to its performance. Another method of expressing the performance of the fan is to monitor the change in total pressure across the fan. The total pressure is the sum of the static and dynamic pressures at a point in the flow field. Because the flow into the rotor only has a meridional component, it is possible to calculate the inlet dynamic pressure and therefore the inlet total pressure. At the discharge of the rotor, the dynamic pressure has two components: meridional and tangential. In the BS 848 code for testing fans, the latter is discarded in the calculation of the total pressure as it is deemed useless. Therefore, in an effort to conform to generally accepted standards, the same definition of total pressure is used here and the fan's performance assessed in terms of the total-to-total pressure rise.
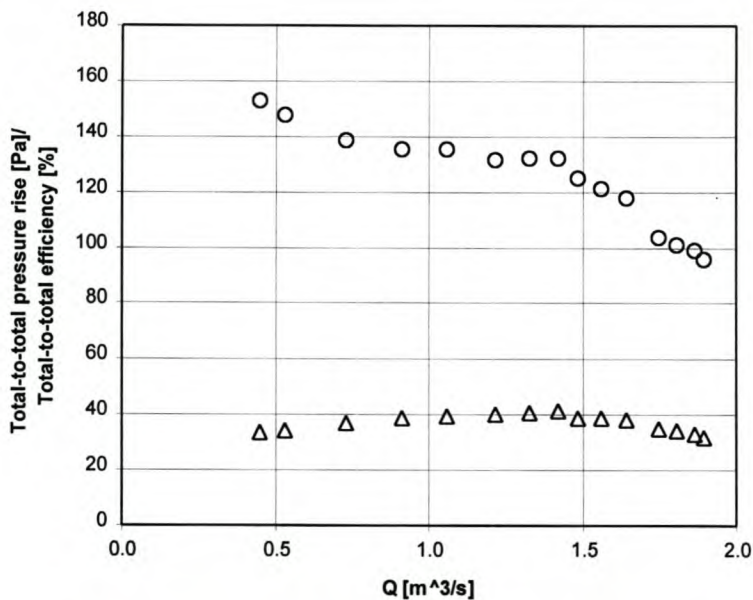
Figure 6.10: Performance of the mixed flow fan at 960 rpm ($\rho = 1.2$ kg/m³)

6.14

The fan was tested in the test facility shown in figure 6.1. At the start of the test, the throttle was opened to allow the flow to travel through the tunnel at a high rate with low resistance. As the throttle was closed up, the resistance in the tunnel increased and the flow rate decreased. Each point on the graph in figure 6.10 represents throttle setting at which the fan performance was calculated. See Appendix D for sample calculations. The pressure curve shown in figure 6.10 has a constant gradient as the flow is throttled from 1.8 m^3/s to 1.4 m^3/s, after which it flattens out between 1.4 m^3/s and 0.8m^3/s. One reason for the degeneration of fan performance at 1.4 m^3/s was that the fan blade started to stall at the tip. As the volume flow rate reduced, the value of the relative inlet angle increased along with the angle of attack of the blade element. At the a flow rate of about 1.4 m^3/s the angle of attack was large enough to induce stall in that section of the blade, which resulted in a drop in performance. This phenomenon is also descibed by Saha et al (1995). Refer to section 2.4.3.

6.6.2 *Five hole probe experimental results*

A five hole probe was inserted immediately downstream of the rotor to measure the size and orientation of the exit flow velocity vector. This measurement was done at two duty points: high and low mass flow as shown in Figures 6.11 to 6.14. Strohmaier (1997) calibrated the five hole probe and therefore his pitch and yaw angle convention is used (figure 6.5). Note that these measurements were only done downstream of the rotor. The flow into the rotor was accelerating and subsequently easily and accurately modelled. Although the physical size of the probe tip inhibits flow measurement at the edge of the casing and hub, in some cases (Figures 6.11 and 6.12) the results are limited to an even smaller region than the probe can normally operate. The five hole probe has a slow response and only senses the average flow vector. In the case of low velocity or recirculating flow, it is often unable to take a stable reading in its domain of operation.

HIGH MASS FLOW
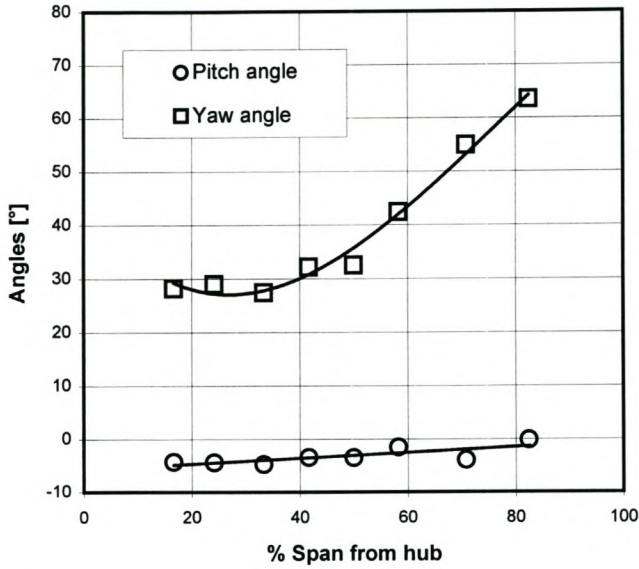
Figure 6.11: Pitch and yaw angles measured by the probe for Q=1.83m^3/s
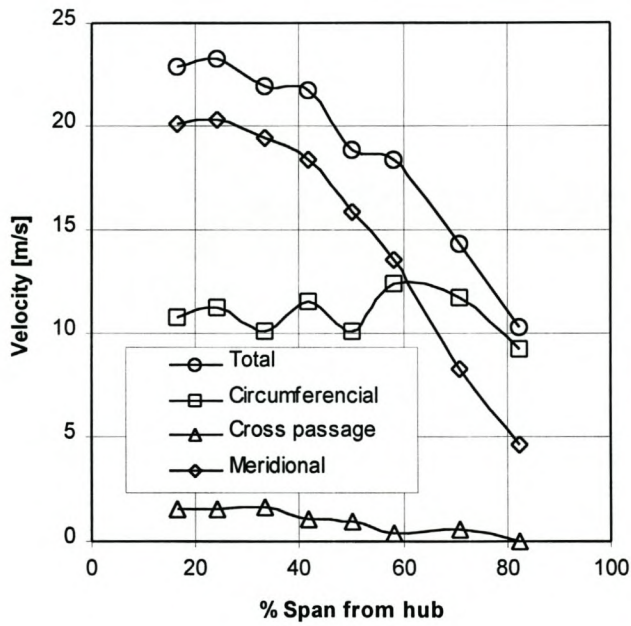
Figure 6.12: Velocity components of the exit flow vector for Q=1.83m^3/s

LOW MASS FLOW
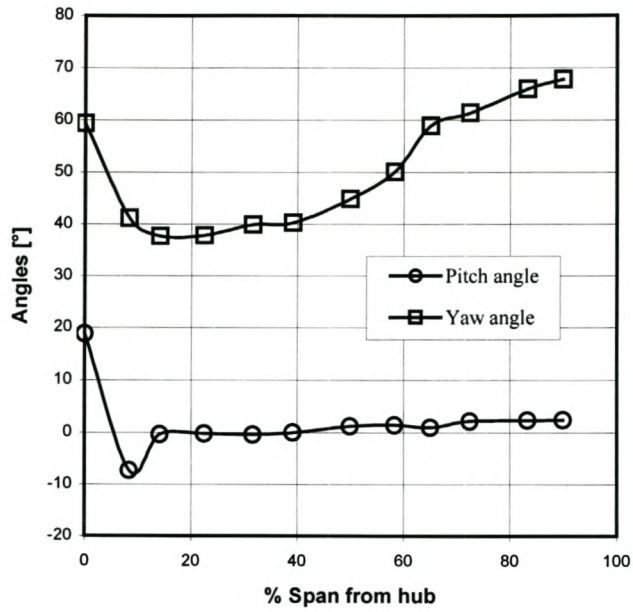
Figure 6.13: Pitch and yaw angles as measure by the probe for Q=1.18m^3/s
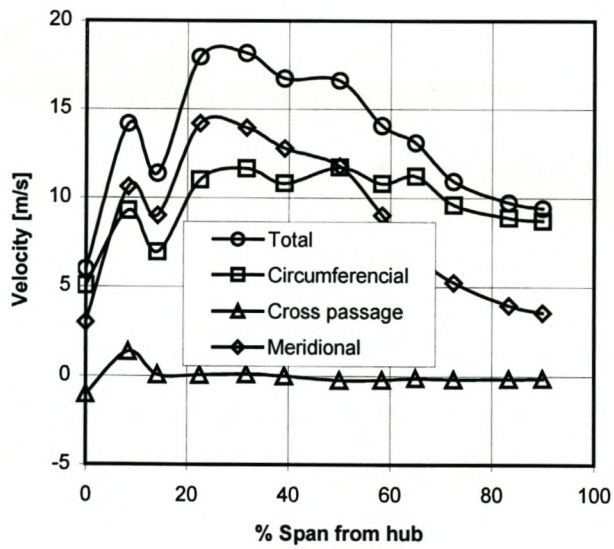
Figure 6.14: Velocity components of the exit flow vector for Q=1.18m^3/s

6.7   Discussion of experimental results

The mixed flow fan does not perform as expected as seen from the results of the overall performance test in Figure 6.10. It is noted that the total pressure rise curve is flat and peaks at a value far below expectation and that the efficiency is low as well. The purpose of this section is to find out whether it is the rotor that is under performing or the annulus geometry that is a source of losses or both.

6.7.1   Rotor performance

One way of accessing the rotor performance was to calculate the rotor efficiency. Cumpsty (1989) defined total-to-total rotor efficiency as follows:

$$\eta_{rotor} = \frac{\Delta P_{total} Q}{W_{in}} \qquad\qquad 6.3$$

The change in total pressure across the rotor was calculated from knowledge of the total pressure at the inlet and the value derived from the probe measurements at the exit. The inlet total pressure was the sum of the measured static and the dynamic pressures as shown in equation 6.4.

$$P_{total,in} = P_{static} + \frac{8\rho Q^2}{\pi^2 D^4} \qquad\qquad 6.4$$

For the exit total pressure, the stagnation pressure as measured by the 5-hole probe was averaged according to volume flow. This implies that, effectively, the average total pressure was such that it would, given a uniform volume flow, do the same work as the sum of the incremental work. From this assumption equation 6.5 followed.

$$\bar{P}_{total} = \frac{\int P_{total}.V_m.r dr}{\int V_m.r dr} \qquad\qquad 6.5$$

In order to use discrete experimental results, equation 6.5 was written in a different form as shown in equation 6.6.

$$\bar{P}_{total} = \frac{\sum P_{total} V_m.r \delta r}{\sum V_m.r \delta r} \qquad\qquad 6.6$$

6.18

The results are presented in table 6.4.

	$P_{total, in}$ [Pa]	$P_{total, out}$ [Pa]	ΔP_{total} [Pa]	Power$_{out}$ [W]	Power$_{in}$ [W]	η_{rotor} [%]
High	-42.1	167.0	209.1	382.7	520.4	74%
Low	-18.9	190.6	209.5	247.2	355.9	70%

Table 6.4: Rotor efficiencies as measured for $Q_{HIGH}=1.83m^3/s$ and $Q_{LOW}=1.18m^3/s$.

The total-to-total rotor efficiency for the higher of the two volume flows was 74% which meant that the rotor was performing better than was indicated by the total-to-total efficiency at the same flow rate. Although better than expected, this figure was still below an acceptable value of around 85%.

A comparison between the design and measured meridional velocity profiles is shown in figure 6.15. The large difference in the shape of the profiles indicate that the reason for the under performance of the rotor lies in its through-flow properties.
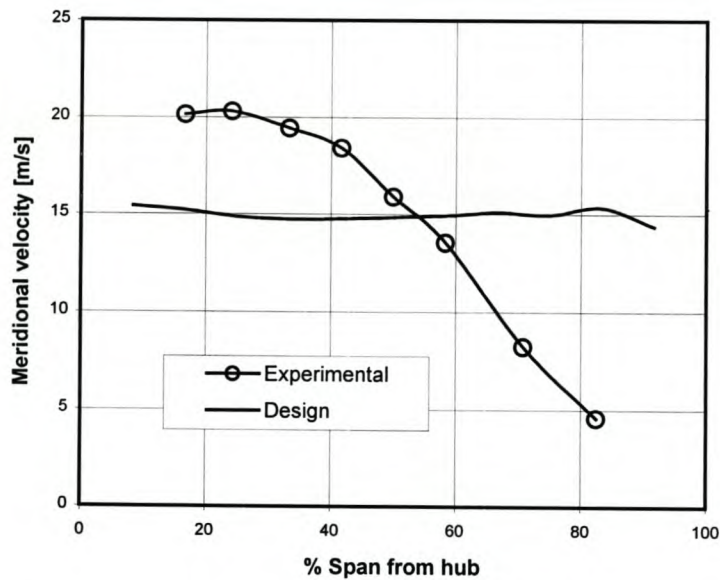
Figure 6.15: Comparison between experimental, design and simulation results

The mass flow measured with the bellmouth inlet at the duty point shown in figure 6.15 was 2.13 kg/s, where the corresponding value calculated by integrating the meridional velocity, measured with the probe, across the rotor span was 2.05 kg/s. This discrepency was because

the probe has a tendency to under predict the velocity if the yaw angle is outside the −10° to +10° band, as illustrated in section 6.4. The probe was set at a nominal yaw of 40° and from figure 6.11 it is clear that the yaw angle in the top 30 % of the rotor (towards the tip) was outside this accurate measuring band of the probe.

The experimental meridional velocity curve had the tendency to fall away toward the tip (refer to figure 6.15), which was in steep contrast with the design curve. It follows that the velocity at the hub increases as flow accelerates to try to satisfy continuity. The blade-flow interaction is akin to the chicken and egg scenario - it is difficult to say which of these two effects initiated the cycle that led to the degradation of the rotor performance. One argument would be that if, for some reason, the blade was doing too much work at the hub, this would lead to accelerated flow close to the hub and a subsequent reduction in velocity in the tip region, causing the streamlines to contract toward the hub.

The first consequence of the contracting streamlines was a change in the angle with which the flow entered the rotor. This change in angle could be broken into two components: a change in incidence angle and a change in angle with which the flow enters the rotor in the meridional plane. A large increase in incidence angle causes increased losses due to partial or complete separation of the flow on the suction side of the rotor blade. The effects of the latter component, however, are secondary. The air travels over a different section of the blade and this new path is longer with an increase in boundary layer thickness and a subsequent increase in losses. The flow also sees a different shape that has a lower camber and is not able to turn the flow as much as it should to do the necessary work.

How does this theory tie up the experimental results, i.e. what is the value of the exit flow angle, especially at the tip of the rotor, based one the above postulate? The meridional flow velocity decreased while the tangential velocity stayed constant and because the work done was less, i.e. the Euler head decreases, the tangential component of the absolute velocity decreased which implied that the tangential component of the relative velocity increased – causing the relative exit angle to increase. Figure 6.16 confirms that this was indeed the case.
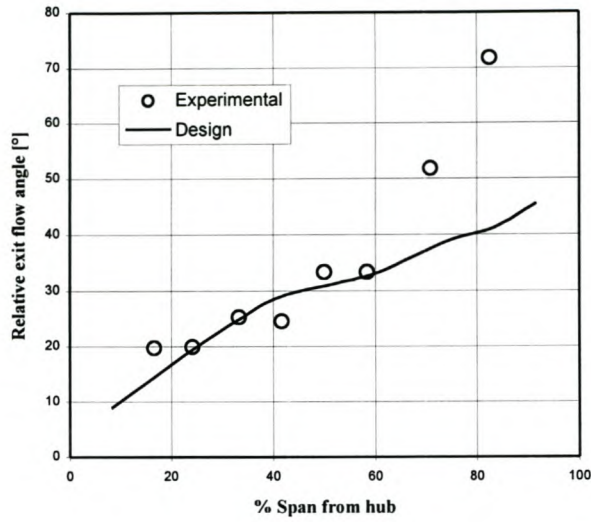
Figure 6.16: Comparison between the experimental and design values of the exit relative flow of the MFF.

A second consequence of the contracting streamlines was a reduction in the radius ratio over the span of the blade as shown in figure 6.17. The amount of Coriolis work (refer to equation 3.4) the rotor did, was directly related to the radius ratio and therefore, irrespective of the aerodynamic performance of the blade, it could be deduced that the performance diminished due to this effect.
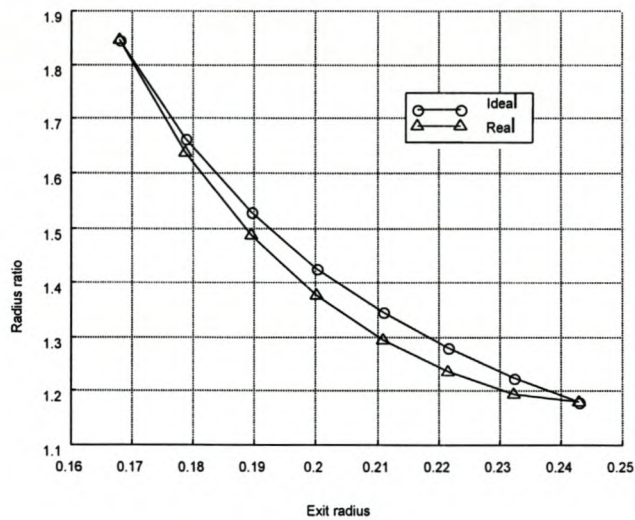
Figure 6.17: Comparison between the design and actual radius ratios over the span of the blade.

Earlier in this section, an average value for the rotor efficiency was calculated. Some authors calculate the rotor efficiency as a function of the span; this author prefers to look at a non-dimensional distribution of work along the span. Soundranayagam et al (1996) split the specific work into two terms, namely the Coriolis and aerodynamic work. This ties in with the effect that radius ratio has on the performance, as the Coriolis term is a function of the square of the radius ratio. Figure 6.18 shows this non-dimensional distribution for the high mass flow case. Refer to Appendix D for a sample calculation.
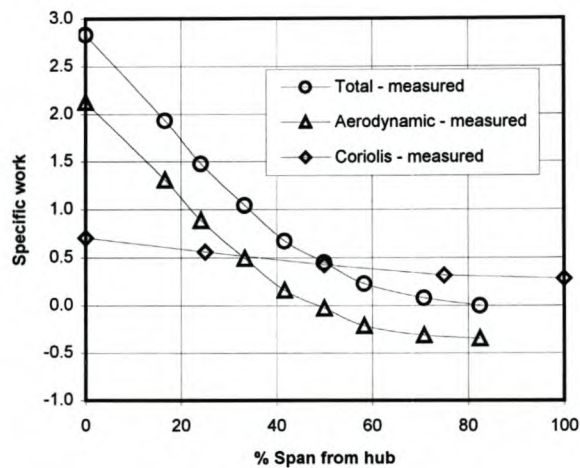
Figure 6.18: Specific work distribution for Q = 1.83 m³/s

Figure 6.18 indicates that negative aerodynamic work was done for the top half of the blade. The tip region of the blade was therefore acting as a turbine, negating the effect of the aerofoil shape. This result is confirmed by looking at a comparison between the design and experimental values of the de Haller load factor as shown in figure 6.19. Cumpsty (1989) recommends that the value of the de Haller load factor should not be less than 0.75 for satisfactory fan performance. It is clear that more than half of the blade towards the tip does not comply with this rule and that the ratio of discharge relative velocity to inlet relative velocity becomes too small. This implies that the relative flow decelerates at a rapid pace through the blade row.
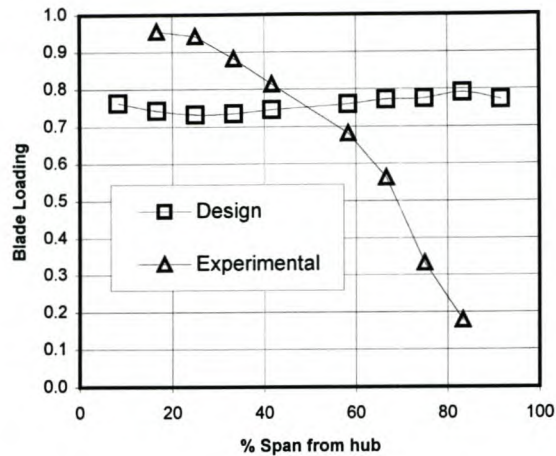
Figure 6.19: Comparison between the design and experimental values for the deHaller load factor

6.7.2 *Annulus performance*

The annulus geometry of mixed flow fans influences the fan performance more than is the case with their axial flow counterparts. Two aspects of this geometry will be discussed.

➤ *The shape of the annulus.* A straight, parallel annulus, as used in this project, was easier to manufacture and simplifies the conformal transformation. Unfortunately the flow was decelerated as it passes through the rotor (area increased), which may have caused flow separation at the annulus walls or even on the blade suction surface. A possible modification would have been to have different cone angles for the inner and outer walls such that the average meridional velocity stayed constant. One advantage would have been the potential of a more even meridional velocity distribution ensuring that positive work was done at the tip.

➤ *Discharge after the rotor.* The flow that passes through the rotor and has to turn after the hub in order to discharge axially into a larger area after the motor. As seen from the difference in the total-to-total efficiency and the rotor efficiency, substantial losses were associated with this flow diffusion. The exit flow vector also had a large tangential component. Stator blades would have recovered the pressure more efficiently by assisting to turn the flow.

6.8   Conclusion

Experimental results showed that the tip section of the rotor was doing too little work relative to the hub. This effect manifested itself in the form of decreased through flow in the tip region of the rotor. Considering a general exit velocity triangle showed that the exit relative flow angle increased with a decrease in pressure rise for a given blade section. This implied that a blade designed to deliver a high pressure rise will have a small blade stagger angle (measured relative to the axial direction). From this it is possible to deduce that the stagger angle of the experimental fan blade at the tip was too large. A possible solution was to design the blade to do only the aerodynamic work associated with the duty, i.e. the Coriolis work was subtracted from the overall work at each radial station, resulting in the following expression for the aerodynamic pressure rise across the rotor (refer to equation 3.4):

$$P_{ft,Aero} = P_{ft} - \rho \omega^2 \left(r_2^2 - r_1^2 \right) \qquad\qquad 6.7$$

To find the first order effect of subtracting the Coriolis work on the design of the blade, the author redesigned the fan blade shape based only on the aerodynamic work. It was decided to keep the work distribution over the span of the rotor constant as was the case with the original design (recall that this led to the choice of a free vortex exit velocity distribution), such that the average aerodynamic work done was still the same as the total pressure of the original design.
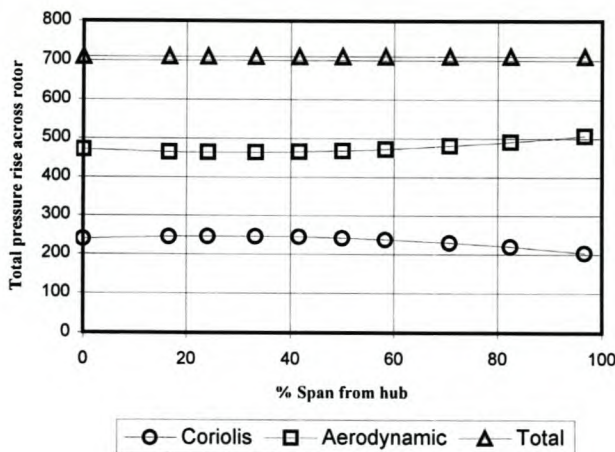
Figure 6.20: The Aerodynamic and Coriolis components of the total pressure rise across the rotor of the fan.

Because the work done along the span is related to the pressure rise across the rotor, figure 6.20 gives an indication of the new work distribution required. This new information was used in the MFF design program along with the MTFM program *Matrix* to find the new blade shape.
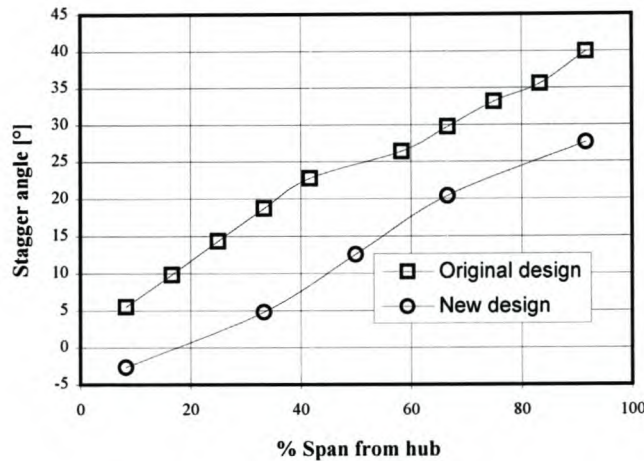
Figure 6.21: A comparison of the stagger angle distributions of the original and new designs.

The Coriolis work term was largest at the hub and decreased toward the tip (refer to figure 6.20) and therefore the aerodynamic work increased from hub to tip. Figure 6.21 illustrates the effect of this work distribution on the stagger angle. Apart from the fact that the stagger angle distribution had decreased across the whole span, the difference between the minimum and maximum stagger angles (i.e. blade twist) had also reduced from 35° to 30°. The new design achieved a reduction in the stagger angle in the tip region of the rotor and it could be expected that the this design would therefore do more work in this region. Bear in mind that viscous effects along the annulus boundary and on the blade shape were not taken into account. Although the blade design was done using only the aerodynamic work requirement, the boundary layer would have seen the full pressure gradient across the rotor and viscous effects would therefore have been an important consideration.

Subtracting the Coriolis work from the total work to find the work distribution required, did have an effect on the blade design and may solve some of the problems associated with the MFF designed in this project. However, it would seem that the adverse pressure gradient caused by the parallel annulus and subsequent increase in area poses the largest problem and therefore this author believes that these streamlines will tend to collapse toward the hub due to

the diffusion effect of the annulus not predicted by this inviscid solution. An improved design would have a hub that has a larger cone angle than the casing, such that the area and subsequently the meridional velocity remains constant through the rotor.

CHAPTER 7

CONCLUSION

"And you run and you run to catch up with the sun, but it's sinking
And racing around to come up behind you again
The sun is the same in a relative way, but it's older
Shorter of breath and one day closer to death"

- Mason, Waters, Wright, Gilmour

The thesis set out to investigate the working of mixed flow fans. The aim of the investigation was to formulate a new design algorithm, compiled from a number of cascade-based methods that would enable the designer to design a mixed flow fan (MFF) without the use of complex 3D computational fluid dynamics. The first part of the algorithm enables the designer to find a whirl velocity distribution based on certain input design parameters. The second part uses this whirl velocity distribution as an input to the matrix through flow method (MTFM) to find the flow distribution through the rotor. Both algorithms were coded in Delphi by the author. Multiple Circular Arc blade profiles were generated using an explicit formulation derived during this project, from the design solution and conformally transformed onto a conical plane. Blades were cut from aluminium blocks on a CNC milling machine and a fan constructed. This fan was tested at the Department of Mechanical Engineering's (University of Stellenbosch) fan test facility to find both the overall performance and the exit velocity profiles. A five-hole probe measured the latter.

Design values were compared to experimental results for both overall and probe measurements and it was found that the fan does not perform as designed. A comparison between the designed and experimental flow vectors confirms this. Most of the work is done at the hub region with a resulting increase in local meridional velocity and a subsequent reduction at the tip. This phenomenon is due to an incorrect assessment of the work that has to be done by the blade, resulting in stagger angles that are too large at the tip. A new design was done using only the aerodynamic component of the total work distribution. The result was a decrease in stagger angle over the span of the rotor blades and a decrease in blade twist.

A method by Lewis (1996) was found after the project was complete and is discussed in Appendix E. It contains a number of useful ideas, the most important being a way to predict the total-to-total efficiency. This made it possible to formulate geometric limits, enabling the

designer to calculate optimum radius and area ratios early in the design phase and start off with a basic design that is inherently efficient.

Although the MFF designed in this project did not perform as expected and only had a total-to-total efficiency of 41 %, it does compete well with existing industrial mixed flow fans. A student at the University of Stellenbosch tested an *Elta** MFF, of similar size, in the same fan test facility as the one presented in this project and found that in the absence of exit stator vanes, the commercial fan had a total-to-total efficiency of 34 %.

The original design method proposed in this thesis has obvious shortcomings. The use of deviation and slip is artificial: many authors use them, but without a complete understanding of the exact 'mixed flow' mechanism. One way to avoid these blade correlations is to use a numerical method that simulates the performance of blades in a general flow field. Lewis (1991) published such a method and it has been used, subsequent to this project, with success at the University of Stellenbosch.

Most of the cascade methods referred to in this project try to cast mixed flow fan design from an axial flow fan design mould. From the information gathered during this project it is clear that, contrary to axial flow fans, the geometry of the annulus has a marked influence on the fan performance. This effect is described by two additional parameters: radius and area ratio, and has to be taken into account during the design process, emphasising the importance of a through flow method such as MTFM. In fact, the geometry of the annulus (parallel walls and cone angle) proved to have a significant influence on the fan performance. Another effect of the MFF geometry is that the flow is often required to return to an axial flow pattern after the rotor. For this reason stator blades are essential to optimise the pressure recovery. It is also mentioned that better results are achieved if the rotor and stator are modelled together.

The insight gained into mixed flow fans is now used to adjust the design method. A brief version of a modified algorithm would be as follows:

➢ Use the Lewis method to find an efficient basic design. This initial design will give the designer a fan geometry to start with.

➢ Subtract the Coriolis term at each radial station from the overall work to find the aerodynamic work, as this is the amount that the blade profiles have to deliver.

---

* Elta Fans Ltd.

➢ Find an exit whirl distribution that will enable the fan to operate at the specified duty and use it in the MTFM program to solve for the flow through the rotor.

➢ Use the calculated flow angles to generate blade profiles and simulate these profiles using a numerical method by Lewis (1991). The result of the simulation is the actual gas angles in the transformed plane.

➢ Return to the MTFM and use the known gas angles as an input to the program to simulate the flow. The amount the blades are able to turn the flow would in most cases be less than the blade camber and therefore the amount of work done would be less than expected.

➢ It is possible that the exit velocity vector may differ from the initial one. The blade angles can now be adjusted to compensate for this discrepancy and remodelled. Also keep in mind that most of the design relationships apply along a streamline and any calculations can now be redone with the updated streamline positions. One important example is the Coriolis work term, which will have different values as the streamlines shift, influencing the amount of work to be done by the blade profiles.

The original design method proposed, has mainly two inherent problems. The first being its inability to guide the designer towards finding a satisfactory annulus geometry. This pertains to the shape and orientation of the annulus, as well as the position of the rotor. The second problem is the failure of the deviation and slip correlations to correctly model the blade flow. Both problems are addressed in the method proposed by Lewis (1996) and is discussed in Appendix E. Based on the findings of this investigation, the recommendation is to avoid the use of empirical correlations used for the design of axial flow turbomachines and implement numerical methods by authors like Lewis (1996) and Moore et al. (1987). The design should include a stator and the numerical methods should model the stator and rotor as a unit.

The main objectives set out in the beginning of this project were achieved.

➢ Mixed flow fans, along with a design method were investigated.

➢ User-friendly programs were written by the author to implement the design algorithm.

➢ A prototype fan was designed and built.

➢ This fan was thoroughly tested and the results compared with the design values.

➢ Most of the discrepancies were explained and the new insight used to modify the existing design procedure.

CHAPTER 8

REFERENCES

Bosman, C, Marsh, H, 1974, An Improved Method for Calculating the Flow in Turbo-Machines, Including a Consistent Loss Model, Journal of Mechanical Engineering Science, vol. 16, no. 1, pp 25-31.

British Standards Institution, Fans for general purpose, Part 1, Methods of Testing Performance, BS 848, 1980

Bruneau, P R P, 1994, The design of a single rotor axial flow fan for a cooling tower application, Master of Engineering thesis, University of Stellenbosch, Stellenbosch, South Africa.

Busemann, A, 1928, Das Förderhöhenverhältniss radialer Kreiselpumpen mit logarithmisch-spiraligen Schaufeln, Zeitschrift fur Angewandte Mathematik und Mechanik, p371-384

Cohen, H, Rogers, G F C, Saravanamuttoo, H I H, 1987, Gas Turbine Theory. Fourth Edition., Addison Wesley Longman Limited, England.

Cumpsty, N A, 1989, Compressor Aerodynamics, 1st Edition, Longman

Denton, J D, Cumpsty, N A, 1987, Loss Mechanisms in turbomachines, Inst. of Mechanical Engineers

Dixon, S L, 1978, Fluid Mechanics-Thermodynamics of Turbomachines, 3rd edition, William Clowes Ltd, Great Britian

Eckhart, D, 1976, Detailed flow investigation within a high speed centrifugal compressor impeller., Trans ASME Journal of Fluids Engineering

Gannon, A J, Von Backström, T W, 2000, Comparison of Streamline and Throughflow and Streamline Curvature Methods, International Journal of Turbo and Jet Engines, Vol 17, pp 161-170.

Goto, A, Takemura, T and Zangeneh, M, 1996, Suppression of Secondary Flows in a Mixed-Flow Pump Impeller by Application of Three-Dimensional Inverse Design Method: Part 2 – Experimental Validation, Transactions of the ASME. Volume 118.

Greyvenstein, G P, 1981, Snelheidsdruk Numeriese Metode vir die Berekening van Tweedimensionele Elliptiese Vloei (Velocity-pressure Numerical Method for the Computation of Two-dimensional Elliptic Flow), Masters Thesis, University of Stellenbosch, Stellenbosch, South Africa

Harms, T M, 1995, A finite volume method for the analysis of flow fields with complex boundaries, Ph.D. Thesis, University of Stellenbosch, Stellenbosch, South Africa

Horlock, J H, 1978, Actuator Disk Theory, 1st Edition, McGraw-Hill Book Company

Horowitz, Paul, Hill, Winfield, 1995, The art of electronics, 2nd edition, Cambridge University Press

Keller, C, 1937, The Theory and Performance of Axial Flow Fans, McGraw-Hill Book Company, Inc.

Lewis, R I, 1991, A Method for Inverse Aerofoil and Cascade Design by Surface Vorticity, ASME Paper No. 82-GT-154.

Lewis, R I, 1996, Turbomchinery Performance Analysis, 1st edition, Arnold London.

Lieblein, S, 1960, Incidence and deviation-angle correlations for compressor cascades, Trans. ASME Journal of Basic Engineering 82: 575-87

McEwen, D, Wilson, G and Neal, A N, 1987, The design of a mixed flow fan of simple blade geometry, Industrial Fans – Aerodynamic Design, Seminar, Mechanical Engineering Publications Limited for The Institute of Mechanical Engineers, London.

Moore, M J, Sieverding, C H, 1987, Aerothermodynamics of Low Pressure Steam Turbines and Condensers, A von Karman Institute Book, Hemisphere Publishing Corporation.

Myles, D J, 1965, A Design Method for Mixed Flow Fans and Pumps, NEL Report No 177, Department of Scientific and Industrial Research

Saha, T K and Soundranayagam, S, 1995, Performance of a Mixed Flow Pump with Varying Tip Clearance Part 1, Proc. Instn Mech Engrs Volume 210

Sarkar, S, 1992, Performance prediction of a mixed flow impeller, Proc. Instn. Mech. Engrs Volume 206

Sayers, A T, 1990, Hydraulic and Compressible Flow Turbomachines, 1st Edition, McGraw-Hill Book Company

Smith, T W, 1987, A practical approach to the design of axial and mixed flow fans, Conference paper, Institution of Mechanical Engineers, London.

Soundranayagam, S and Saha, T K, 1996, Performance of a Mixed Flow Pump with Varying Tip Clearance Part 2, Proc. Instn Mech Engrs Volume 210

Stodola, A, 1927, Steam and Gas Turbines, McGraw-Hill, New York

Strohmaier, Christian K, 1997, An evaluation of a scale modal Medium Speed Wind Tunnel, Masters thesis, University of Stellenbosch, Stellenbosch, South Africa

Takemura, T and Goto A, 1996, Experimental and Numerical Study of Three-Dimensional Flows in a Mixed-Flow Pump Stage, Transactions of the ASME. Volume 118.

Van der Spuy, Johan S, 1997, The design of a low-noise rotor-only axial flow fan series, Masters thesis, University of Stellenbosch, Stellenbosch, South Africa

Van Niekerk, C G, 1964, Ontwerp van waaier met hoë rendement en lae lawaai-intensiteit, D.Sc. thesis, University of Pretoria, Pretoria, South Africa.

Venter, A A, 1993, The Flow Around Torque Converter Turbine Blades, Masters thesis, University of Stellenbosch, Stellenbosch, South Africa

Von Backström, T W, Buys, J D and Stinnes, W H, 1996, Minimisation of the Exit Loss of a Rotor-only, Axial Fan, Eng. Opt., Vol. 26

Wallis, R A, 1983, Axial Flow Fans and Ducts, 1st Edition, John Wiley & Sons

Whitfield, A and Simmons, N C, 1990, Design of Radial Turbomachines, 1st Edition, Longman Scientific & Technical

Wiesner, F J, 1967, A Review of Slip Factors for Centrifugal Impellers, Journal of Engineering for Power

Zangeneh, M, 1991, A Compressible Three-Dimensional Design Method for Radial and Mixed Flow Turbomachinery Blades, Int. Jnl. of Num. Meth. in Fluids. Volume 13. p 599-624

Zangeneh, M, Goto, A and Takemura, T, 1996, Suppression of Secondary Flows in a Mixed-Flow Pump Impeller by Application of Three-Dimensional Inverse Design Method: Part 1 – Design and Numerical Validation, Transactions of the ASME. Volume 118.

APPENDIX A

MULTIPLE CIRCULAR ARC PROFILES

Multiple circular arc (MCA) profiles consist of six circular arcs that are composed to form the suction, pressure, leading edge (LE) and trailing edge (TE) surfaces of a blade section. The six surfaces are shown in Figure A.1. The horizontal line is the chord of the profile while the vertical line divides the upper surface into arcs 1 and 3 and the lower surface into arcs 2 and 4. This line coincides with the position along the chord of maximum camber. It is customary in compressor design to define the camber line as the locus of the centres of the inscribed circles, as shown in Figure A.1. Subsequently the chord is defined as the line that connects the extremities of this camber line. The blade profile is described in a Cartesian co-ordinate system that originates at the LE side of the profile where the camber line and chord line meet.
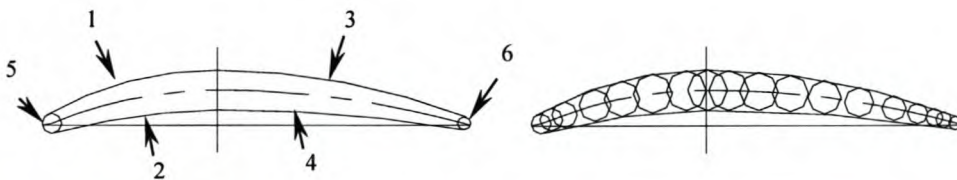
Figure A.1: Multiple Circular Arc blade profile

By adjusting these arcs, it is possible to compose a profile of desired chord, thickness, camber and shape – thus creating a whole family of blade sections. A special case of the MCA blades is the double circular arc (DCA) family of sections, where the profile is symmetrical about the vertical line shown in Figure A.1.

In order to calculate the necessary arc parameters, the profile is split along the vertical line passing through the point of maximum thickness (see Figure A.1). In this analysis it is assumed that the point of maximum thickness and maximum camber coincide. A circular arc is positioned to start at the origin of the co-ordinate system and end perpendicularly at the vertical line, the position of maximum camber. A circle with a given radius is positioned on this arc in such a way that the centre lies on the arc, the end of which lies on the circle. A new

A.1

arc is now positioned to be tangential to the circle and perpendicular at the vertical line. This is the suction surface. Ditto for the pressure surface. This completes the LE side of the blade profile. Figure A.3 shows an exaggerated but detailed semi-profile. The same procedure is followed for the trailing edge after which it is flipped about the vertical line and merged with the LE side to form the complete section. A complete analysis of the position and size of the camber line, nose radius, suction surface and pressure surface arc follows.

A point of discussion is the definition of the camber line. Surely the nose and tail radii are part of the first and last inscribed circles respectively. This raises the question of what happens to the camber line towards the end of the profile and essentially addresses the problem of where to position the LE and TE circles. In this analysis the camber is simply extended until it meets the chord somewhere on the nose circle. It should be mentioned that this arc under discussion does not satisfy the definition of a camber line except at the origin and at the point of maximum camber. This apparent camber line (the circular arc) is only used to define the point of maximum camber as well as to position the leading and trailing edge circles.

Calculation

At some stage in the design of a turbomachine the designer has to specify a blade profile for different positions along the span of the blade. The preferred parameters defining these profiles are:

c	Chord as defined above
α	Amount the LE section of the blade turns the flow
β	Amount the TE section of the blade turns the flow
a	Position of maximum camber
Θ	Camber angle
t	Maximum thickness
R_{LE}	LE nose radius
R_{TE}	TE nose radius

Notice that the camber is given in degrees and not as a height above the chord. This is convenient for the aerodynamicist but at the expense of programming ease as the maximum camber as a distance is needed to calculate the profile parameters. Refer to figure A.2.
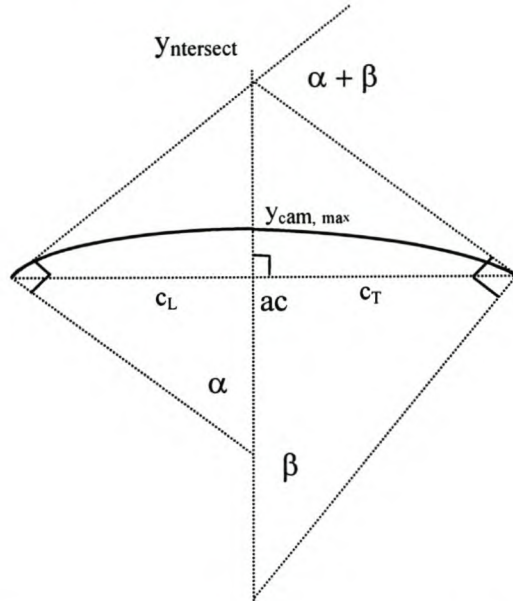
Figure A.2: Layout of the camber line in a MCA profile.

Two methods for calculating the camber line geometry are presented in this appendix:

Method 1:

The first method finds an analytical solution for α, β and $y_{cam, max}$ as a function of the camber and the position of maximum camber. This method is based on the assumption that the tangents of the LE and TE intersect on the vertical line passing through the point of maximum camber. In general this assumption is only valid for a symmetrical camber line, i.e. where a = 0.5. The error increases with an increase in camber and as the position of the maximum camber moves away from the middle of the chord, but is acceptable in the range of values used in fan blades ($Q < 50°$; $|a - 0.5| \leq 0.2$). For a blade with a 50° camber and the position of the maximum camber at 30%, the value of α differed from the exact solution by 0.6°.

The following relationships follow from the geometry.

$$\theta = \alpha + \beta \qquad\qquad A.1$$

$$y_{int\,er\sec} = ac \tan(\alpha) \qquad\qquad A.2$$

$$y_{int\,er\sec} = (1 - a)c \tan(\beta) \qquad\qquad A.3$$

A.3

Combine equations A.1 to A.3 to derive equation A.4.

$$c_L \tan(\alpha) - c_T \tan(\Theta - \alpha) = 0 \qquad \text{A.4}$$

Substitute the well-known tan rule (equation A.5) into equation A.4 and simplify.

$$\tan(\Theta - \alpha) = \frac{\tan(\Theta) - \tan(\alpha)}{1 + \tan(\Theta)\tan(\alpha)} \qquad \text{A.5}$$

$$c_L \tan(\Theta)\tan^2(\alpha) + (c_L + c_T)\tan(\alpha) - c_T \tan(\Theta) = 0 \qquad \text{A.6}$$

Equation A.6 is a simple quadratic equation that can be solved to find α and therefore also β.

$$\tan(\alpha) = \max\left[\frac{-c \pm \sqrt{c^2 + 4c_L c_T \tan^2(\Theta)}}{2c_L \tan(\Theta)} \right] \qquad \text{A.7}$$

The maximum camber is subsequently known from the geometry in figure A.3.

$$y_{cam,max} = \frac{ac}{\tan\left[\frac{1}{2}(\pi - \alpha)\right]} \qquad \text{A.8}$$

Method 2:

The second method is based on the fact that the two arcs forming the camber line, meet at the point of maximum camber. The designer specifies α and Θ and calculates β from equation A.1. The camber is calculated using equation A.9 and from this relationship equation A.10 follows.

$$y_{cam,max} = R_L(1 - \cos \alpha) = R_T(1 - \cos \beta) \qquad \text{A.9}$$

$$\frac{R_L}{R_T} = \frac{(1 - \cos \beta)}{(1 - \cos \alpha)} \qquad \text{A.10}$$

From the geometry shown in figure A.2 the chord sections (c_L and c_T) follow:

$$c_L = R_L \sin \alpha \qquad \text{A.11}$$

$$c_T = R_T \sin \beta \qquad \text{A.12}$$

Equations A.10, A.11 and A.12 are combined to find the chord section ratio as a function of α and β as shown in equation A.13. The symbol Γ is assigned to this quantity to simplify the formulation.

$$\frac{c_L}{c_T} = \frac{R_L \sin\alpha}{R_T \sin\beta} = \left(\frac{1-\cos\beta}{1-\cos\alpha}\right)\left(\frac{\sin\alpha}{\sin\beta}\right) = \Gamma \qquad\qquad \text{A.13}$$

From equation A.13 and the fact that $c = c_L + c_T$ the position of maximum camber can be calculated as shown in equation A.14.

$$\frac{c_L}{c} = \frac{\Gamma}{\Gamma+1} \qquad\qquad \text{A.14}$$

Solve for c_L and c_T and substitute into equations A.11 and A.12 to find R_L and R_T. The camber, $y_{cam, max}$, follows from equation A.9.

All the relevant parameters are now known and can be used to find the upper and lower surfaces of the blade profile. It has been mentioned that the LE and TE sides of the profile are generated in exactly the same way. For this reason a generic semi-profile, whether it is LE or TE, will be discussed in the following paragraphs.

A general circle has an origin at point (m,n). The equation describing this circle is:

$$(x-m)^2 + (y-n)^2 = R^2 \qquad\qquad \text{A.15}$$
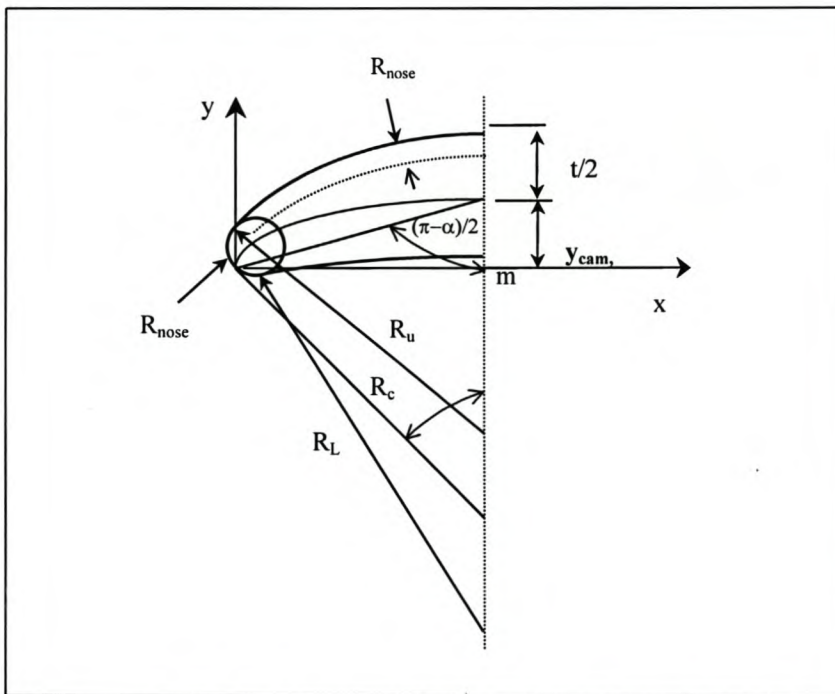
Figure A.3: Schematic drawing of the MCA configuration

The circles that contain the surface arcs are perpendicular to the vertical line passing through the point of maximum thickness/camber. This implies that the vertical is also a radius of the

circle and that the centre of the circle lies on this line. The parameter m, associated with the x-coordinate of the arc centre, is the distance from the origin of the co-ordinate system to the vertical line mentioned above. From equation A.15 it follows that the two remaining variables that have to be solved for, are n and R. The camber line is considered first. By definition, it has to pass through the origin as well as the point of maximum camber.

α can be used to find n_c, where the 'c' subscript refers to camber.

$$n_c = \frac{a.c}{\tan(\alpha)} \qquad \text{A.16}$$

$$R_c = \frac{a.c}{\sin(\alpha)} \qquad \text{A.17}$$

Once the camber line is known, the nose circle can be fitted so that the centre lies on the camber line, a distance R_{nose} from the edge. It is possible to find this point (x_0, y_0) with a simple geometric construction.

Place a circle with radius R_{nose} on the origin of the co-ordinate system and find the co-ordinates of the point where the two circles meet. This point is (x_0, y_0). Two circles overlapping have, in general, two solutions. However, in this case, the applicable one is obvious. Connect (x_0, y_0) and $(0,0)$. An isosceles triangle is formed with ψ being the opposite angle to the constructed line. Apply the cosine rule.
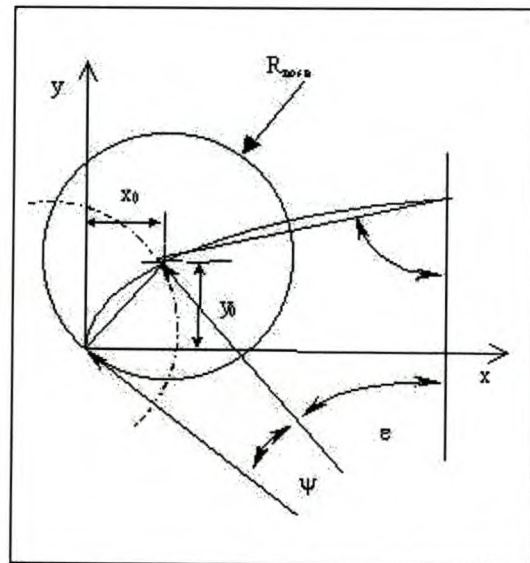
Figure A.4: Close-up of Nose of Section

$$\cos(\Psi) = 1 - \frac{R_{nose}}{2R_c^2} \qquad \text{A.18}$$

α is known either from equation A.7 or as a design choice. The relationship between ψ and ε is therefore:

A.6

$$\varepsilon = \alpha - \Psi \qquad\qquad\qquad\qquad\qquad \text{A.19}$$

Construct a line that spans the radii and is opposite to ε. From the resulting triangle:

$$\gamma = \frac{\pi - \varepsilon}{2} \qquad\qquad\qquad\qquad\qquad \text{A.20}$$

$$l^2 = 2R_c^2(1 - \cos\varepsilon) \qquad\qquad\qquad\qquad\qquad \text{A.21}$$

The problem is solved. The point (x_0, y_0) follows easily:

$$x_0 = m - l\sin\gamma \qquad\qquad\qquad\qquad\qquad \text{A.22}$$

$$y_0 = y_{cm} - l\cos\gamma \qquad\qquad\qquad\qquad\qquad \text{A.23}$$

The next step is to find the arc that is tangent to the nose circle and passes through a point on the vertical $t/2$ above the camber line. In order to find an analytical solution, a simple construction is made. Fit a concentric circle to pass through (x_0, y_0) and the point A as shown in Figure A.3. Construct a line that connects these two points. An isosceles triangle is formed. The included angle, δ, of this triangle follows from elementary geometry.

$$\delta = \pi - 2\tan^{-1}\left(\frac{m - x_0}{y_A - y_0}\right) \qquad\qquad\qquad \text{A.24}$$

Now the position of the centre of this arc is calculated.

$$n = \frac{m - x_0}{\tan(\delta)} - y_{nose} \qquad\qquad\qquad\qquad \text{A.25}$$

Where m (position of vertical along the x-axis) is known and y_A can be calculated geometrically.

$$y_A = y_{cm} + \frac{t}{2} - R_{nose} \qquad\qquad\qquad\qquad \text{A.26}$$

The radius of this constructed arc, R', follows from the same geometry. The sought arc is just a concentric arc to this one.

$$R' = \frac{m - x_0}{\sin(\delta)} \qquad\qquad\qquad\qquad\qquad \text{A.27}$$

$$R = R' + R_0 \qquad\qquad\qquad\qquad\qquad \text{A.28}$$

A similar construction can be done for the pressure surface. The next step is to find the point where the upper surface and the nose circle tangentially meet. The point (x_t, y_t) follows from simple trigonometric relationships.

$$x_t = x_0 - R_{nose} \sin(\delta) \qquad \text{A.29}$$

$$y_t = y_0 + R_{nose} \cos(\delta) \qquad \text{A.30}$$

The corresponding point for the pressure surface is calculated in the same way.

The nose radius has been positioned,
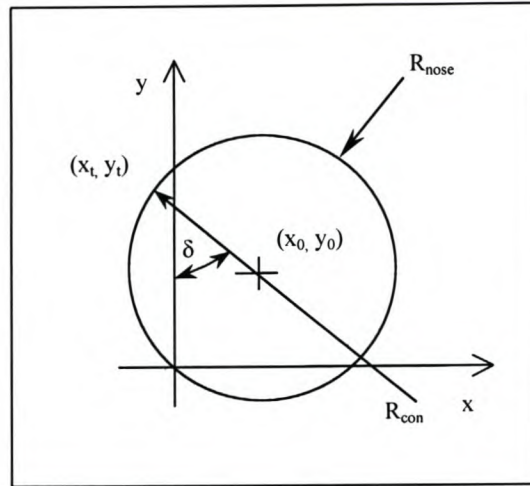
Figure A.5: Definition of the angle delta

the upper and lower surface calculated as well as the points where the arcs various arcs meet. The designer can now calculate both halves of the profile and merge them to form a complete section. This concludes the description of the general MCA blade profile.

Zero camber

It may be necessary in some cases to use a MCA blade with zero camber, i.e. the radius of curvature of the camber line goes to infinity. This special case has to be treated separately, but fortunately leads to simplification. The position of the nose radius is straightforward and needs no explanation, while the point on the nose arc where the pressure surface is tangential to the arc, is simply the point (x_0, y_0-R_{nose}). The rest of the profile is generated as is explained above.

APPENDIX B

DISCRETISATION FOR THE MATRIX THROUGH FLOW METHOD

The discretisation method used in this project, is the one by Greyvenstein (1981). This method discretises the differential equations for a finite difference solution on a non-uniform grid. A uniform grid is one where Δx and Δy are equal throughout the grid. In general, this is not true. Figure 4.1 is shown again for convenience. Note that the aim is to find ψ as a function of r and z.
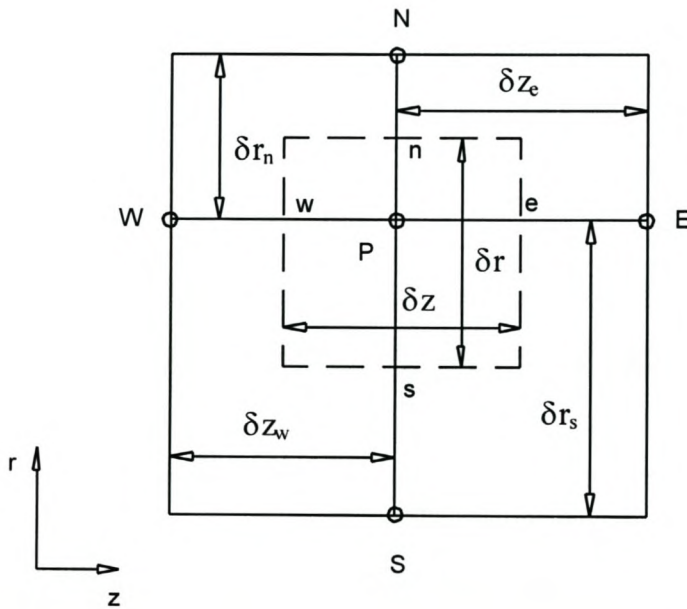
Figure B.1: Nomenclature for the discretisation grid of Greyvenstein (1981)

The gradient in the z direction is given by:

$$\left[\frac{\delta\psi}{\delta z}\right] = \frac{(\psi_P - \psi_W)}{\delta z_w} + \frac{\delta z_w}{2\delta z}\left[\frac{(\psi_E - \psi_P)}{\delta z_e} - \frac{(\psi_P - \psi_W)}{\delta z_w}\right] \qquad \text{B.1}$$

$$= ZG1(\psi_E - \psi_P) + ZG2(\psi_P - \psi_W)$$

B.1

where

$$ZG1 = \frac{\delta z_w}{2\delta z \delta z_e}$$

$$ZG2 = \frac{\delta z_e}{2\delta z \delta z_w}$$

B.2

Similarly, the gradient in the r direction is:

B.3

$$\frac{\delta \psi}{\delta r} = RG1(\psi_N - \psi_P) + RG2(\psi_P - \psi_S)$$

where

$$RG1 = \frac{\delta r_s}{2\delta r \delta z_n}$$

B.4

$$RG2 = \frac{\delta z_n}{2\delta z \delta z_s}$$

B.2

APPENDIX C

FINITE ELEMENT ANALYSIS OF THE MFF HUB

Despite the simplicity of the hub geometry, no analytical relationship between the applied load and induced stresses exists. A finite element analysis was done by J Steyn, a post-graduate student in Solid Mechanics at the Department of Mechanical Engineering at the University of Stellenbosch. The aim of the analysis was to find the distribution of stresses in the hub and subsequently find the limiting size at which the part would fail for a given load. Two types of loading were simulated. The first type assumed that all the blades were equally spaced and had the same mass, while the second type had an additional mass on one of the blades in order to test the effect of an unbalanced fan. Table C.1 gives a summary of the material, geometric and loading conditions common to all the cases.

Geometry

Axial length	212.6 mm
Large diameter	378.5 mm
Small diameter	133.0 mm

Material properties

Young's modulus	71 GN/m^2
Tensile strength	140 MN/m^2
Density	2750 kg/m^3
Poisson's ratio	0.33

Loading

Rotational speed	1500 rpm
Blade mass	0.2 kg

Table C. 1: A summary of the analysed MFF hub properties

Refer to the figure on page C.2 for the general geometry of the mixed flow fan hub design.

C.1

ITEM	BESKRYWING		GETAL	MATERIAAL		SPES	OPMERKINGS
SKAAL NTS							
MATE IN mm		TITEL:	FEM Modal				
STUDENTE No.	TEKENAAR JH du Toit	NAGESIEN	DATUM 09/02/00	VEL.No	VAN	VELLE	No.

UNIVERSITEIT VAN STELLENBOSCH

C.2
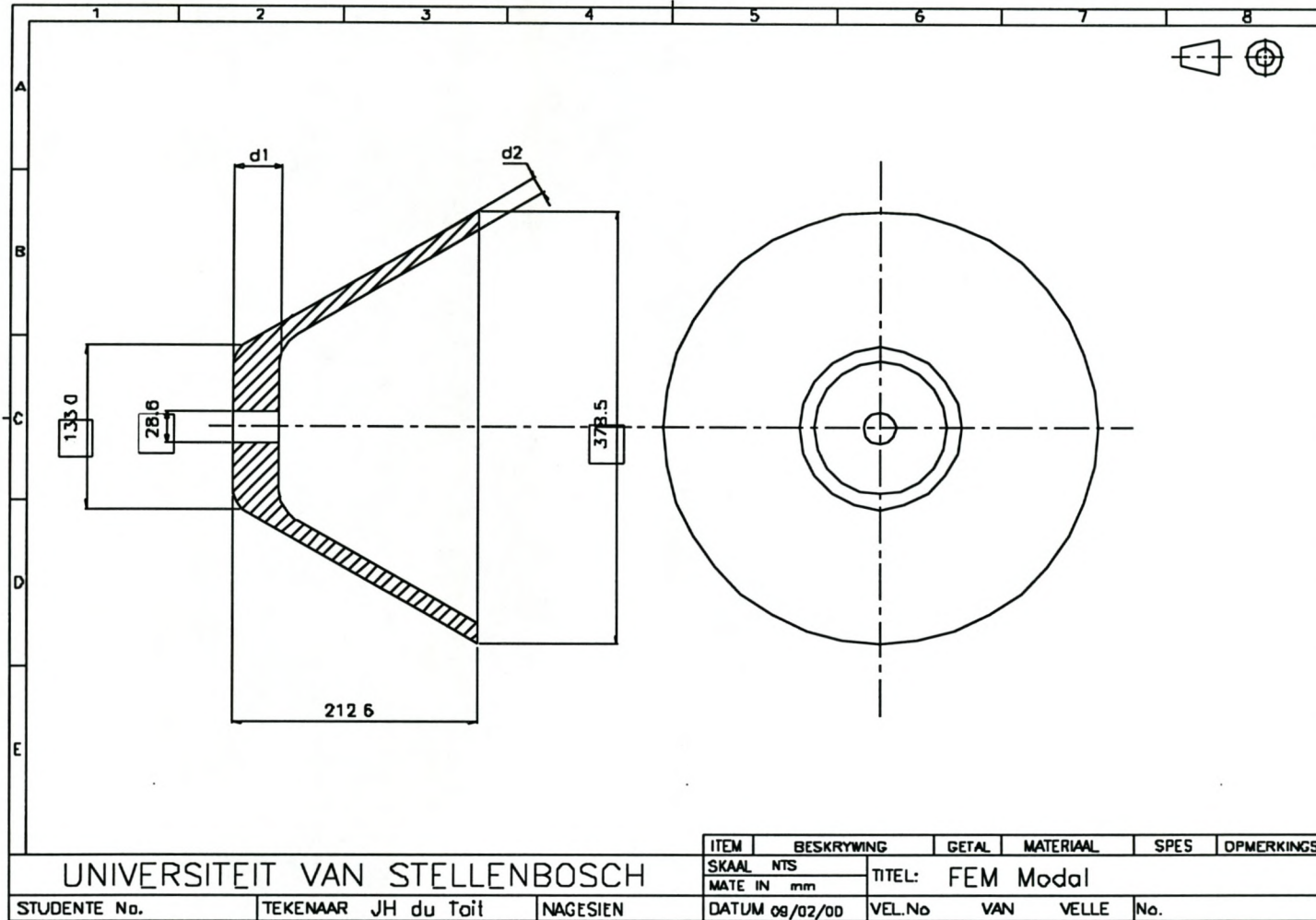
<u>Discussion of stress analysis</u>

The aim of the stress analysis was to find the most lightweight, practical hub that would be able to withstand an asymmetric load of 10 % (0.02 kg) at a speed of 1500 rpm. The first test case used a bulky design with $d_1 = 30$ mm and $d_2 = 25$ mm. From the stress analysis it was clear that the load on the hub is mainly due to the weight of the hub itself. The maximum load was 3.5 MN/m^2 and was distributed symmetrically about the axis of rotation. For the second case the amount of material used in the hub design was greatly reduced with $d_1 = 3.75$ mm and $d_2 = 3.13$ mm. It is clear from the result that the reduction in shell thickness (d_2) caused a reduction in load due to the weight of the hub itself and that the maximum load was due to the weight of the blades and the position of the maximum corresponded to the position of the blades. The maximum stress in test case two was 44.6 MN/m^2. Notice that the first two test cases did not induce a moment about the axis perpendicular to the axis of rotation because the load was balanced. The third and final test case was a stress analysis of the final hub design. In this case the shell thickness was 10 mm and the end thickness 15 mm. It was decided to simulate an unbalanced load in order to take possible inaccuracies in the blade manufacturing into account. The maximum stress was 0.152 MN/m^2 and in the region of the unbalanced blade. The designer decided to use more material in the final design than was necessary to make sure that the hub was stiff and the end section seated properly on the shaft.

APPENDIX D

SAMPLE CALCULATIONS

D.1 Instrument calibration

All transducers used in this project were linear. Therefore the relationship between the measured signal and the value of the property required the solution of two coefficients and subsequently two points that satisfy the calibration equation. Although only two points are needed to solve for the coefficients, three were used to validate the linearity of the instrument. The measured values were compared to a physical quantity that could be measured.

D.1.1 Pressure calibration

A Betz manometer gives the pressure as a height in millimeters of water which is translated to Pascal by the following equation.

$$P = \rho g h_{Betz} \qquad \text{D.1}$$

From equation D.1, with $\rho = 998$ kg/m^3 and $g = 9.81$ m/s^2 the calibration can be completed as in table D.1.

#	Betz [mm H$_2$O]	Pressure [Pa]	Pressure [mV]
1	0	0	0
2	10	97.90	984
3	20	195.81	1984

Table D. 1: Calibration data for the pressure transducer

The relationship between the measured signal in millivolts and the value of the property in Pascal is therefore given by equation D.2.

$$P = m_p V + c_P \qquad \text{D.2}$$

A linear regression is done on the data using the least squares method. This reduces the problem of finding the coefficients of the linear function the solution of the following equation.

$$\begin{bmatrix} \sum X_i^2 & \sum X_i \\ \sum X_i & \sum 1 \end{bmatrix} \begin{bmatrix} m_P \\ c_P \end{bmatrix} = \begin{bmatrix} \sum X_i Y_i \\ \sum Y_i \end{bmatrix} \qquad \text{D.3}$$

X_i is the definition set and Y_i the value set of the experimental data. Equation D.2 can now be solved for m_P and c_P.

$$\begin{bmatrix} 4904512 & 2968 \\ 2968 & 3 \end{bmatrix} \begin{bmatrix} m_P \\ c_P \end{bmatrix} = \begin{bmatrix} 484325.408 \\ 293.412 \end{bmatrix}$$

$$\begin{bmatrix} m_P \\ c_P \end{bmatrix} = \begin{bmatrix} 0.0985 \\ 0.2650 \end{bmatrix}$$

D.1.2   Torque calibration

The equation describing the relationship between the bridge amplifier reading and the measured torque is:

$$P = m_T V + c_T \qquad \text{D.2}$$

The torque transducer was calibrated a number of times using an arm of known length and test weights. The calibrated value agreed very well with the value specified by HBM on the transducer. This value was used to set up the bridge amplifier (which was also made by HBM) accurately with the following values for the parameters in the calibration equation.

$m_T = 0.01$

$c_T = 0.0$

D.2 Performance

#	P1 mV	P1 Pa	P2 mV	P2 Pa	P6 mV	P6 Pa	T mV	T N.m	qm kg/s	qv m^3/s	rho2 kg/m^3	rho6 kg/m^3	Pd2 Pa	Pd6 Pa	Pt2 Pa	Pt6 Pa	Pft Pa	Wtuit W	Win W	Eff, tot %	Pft,stand Pa	Win,stand W
1	-3297.2	-324.8	-3847.3	-379.1	202.3	20.2	541	5.41	2.171	1.90	1.140	1.145	319.595	21.2	-59.48	41.40	100.88	191.4	543.87	35.18	105.75	570.13
2	-3285.2	-323.7	-3737.8	-368.3	202.2	20.2	550	5.41	2.167	1.89	1.141	1.145	318.4	21.1	-49.89	41.31	91.20	172.7	543.87	31.75	95.60	570.13
3	-3183.7	-313.6	-3585.2	-353.2	293.8	29.2	526	5.26	2.134	1.86	1.141	1.145	308.5	20.5	-44.73	49.69	94.43	176.0	528.79	33.28	98.98	554.32
4	-2989.4	-294.5	-3366.3	-331.7	355.7	35.3	505	5.05	2.067	1.81	1.141	1.145	289.6	19.2	-42.06	54.54	96.61	174.5	507.68	34.37	101.27	532.19
5	-2819.8	-277.8	-3351.2	-330.2	413.0	41.0	500	5.00	2.008	1.75	1.141	1.145	273.1	18.1	-57.02	59.10	116.11	203.7	502.65	40.52	121.72	526.92
6	-2803.6	-276.2	-3114.0	-306.8	459.8	45.6	490	4.90	2.002	1.75	1.141	1.145	271.5	18.0	-35.27	63.61	98.88	172.9	492.60	35.11	103.65	516.38
7	-2553.5	-251.5	-2937.3	-289.3	594.1	58.8	490	4.90	1.911	1.67	1.141	1.145	247.2	16.4	-42.13	75.24	117.37	195.9	492.60	39.77	123.04	516.38
8	-2478.2	-244.1	-2772.5	-273.1	638.4	63.2	483	4.83	1.882	1.64	1.142	1.145	239.9	15.9	-33.22	79.13	112.35	184.7	485.56	38.04	117.77	509.01
9	-2235.7	-220.2	-2524.1	-248.6	699.0	69.2	465	4.65	1.788	1.56	1.142	1.146	216.3	14.4	-32.27	83.54	115.81	180.8	467.47	38.69	121.40	490.04
10	-2019.7	-198.9	-2285.8	-225.1	772.1	76.4	455	4.55	1.699	1.48	1.142	1.146	195.4	13.0	-29.76	89.36	119.11	176.8	457.42	38.65	124.86	479.50
11	-1859.0	-183.0	-2131.0	-209.8	847.9	83.9	430	4.30	1.630	1.42	1.142	1.146	179.8	11.9	-30.08	95.80	125.88	179.2	432.28	41.46	131.96	453.15
12	-1618.9	-159.4	-1828.7	-180.0	929.3	91.9	407	4.07	1.521	1.33	1.143	1.146	156.5	10.4	-23.58	102.28	125.86	167.2	409.16	40.87	131.94	428.91
13	-1356.8	-133.5	-1517.9	-149.4	997.7	98.6	380	3.80	1.392	1.22	1.143	1.146	131.1	8.7	-18.35	107.34	125.69	152.8	382.02	40.01	131.75	400.46
14	-1029.1	-101.2	-1176.9	-115.8	1072.1	106.0	345	3.45	1.212	1.06	1.143	1.146	99.3	6.6	-16.47	112.57	129.05	136.6	346.83	39.39	135.28	363.58
15	-760.1	-74.7	-841.3	-82.7	1160.8	114.7	300	3.00	1.041	0.91	1.144	1.146	73.3	4.9	-9.43	119.58	129.01	117.3	301.59	38.91	135.24	316.15
16	-492.2	-48.3	-546.5	-53.6	1242.8	122.8	260	2.60	0.837	0.73	1.144	1.146	47.3	3.1	-6.29	125.95	132.24	96.7	261.38	36.99	138.62	274.00
17	-264.4	-25.8	-292.1	-28.5	1378.8	136.2	220	2.20	0.612	0.53	1.144	1.146	25.3	1.7	-3.24	137.89	141.13	75.5	221.17	34.11	147.95	231.85
18	-189.1	-18.4	-192.1	-18.7	1454.8	143.7	195	1.95	0.516	0.45	1.145	1.146	18.0	1.2	-0.66	144.91	145.57	65.7	196.04	33.50	152.60	205.50

Table D.2: Performance data of the mixed flow fan

Table D.2 shows the experimental results of the overall performance of the mixed flow fan. Throttle possition number five (high lighted on table) is used as an example for the sample calculations.

Atmospheric conditions

Patm	29.5	" Hg	=>	99233.5	Pa
Tatm	89	°F	=>	31.7	°C
ρ_{atm}	1.134	kg/m^3	from Ideal Gas Law		

Table D.3: Atmospheric conditions

Pressure

#	Signal			Property	
1	-2819.8	mV	=	-277.5	Pa
2	-3351.2	mV	=	-329.8	Pa
6	412.96	mV	=	40.9	Pa

Table D.4: Pressure data

Torque

#	Signal			Property	
1	541	mV	=	5.41	N.m

Table D.5: Torque data

The next step was to find the relevant performance parameters of the fan, i.e the pressure rise, volume flow, power consumption and efficiency. These parameters were calculated according to the BS 848 standard on ducted fans.

D.4

D.2.1 Volume flow

The volume flow was calculated using a bell mouth inlet. Air was accelerated from stagnation (normal atmospheric) conditions into the inlet duct with a subsequent reduction in static pressure. The process of changing pressure energy into kinetic energy is not reversible and some loss factor, a property of the bell mouth shape, is used to find the volume flow.

$$Q = \alpha \pi D_1^2 \sqrt{\frac{\left(P_{stag} - P_1\right)}{8\rho_1}}$$ D.4

Position 1 (noted by the subscipt) was just after the belmouth. To find the volume flow it was necessary to know the diameter of the duct, the static pressure, density at that point and α. For point 5 of the experimental data set:

	Value	Unit	Comment
α	0.99	-	Calibrated value
D_1	0.315	m	Inlet diameter
D_2	0.630	m	Exit diameter
P_1	-277.8	Pa	From previous section
ρ_1	1.145	kg/m³	use Ideal Gas Law

Table D.6: Relevant experimental data for point 5 of the set

Substitute into equation D.4.

$$Q = 0.99\pi(0.315)^2 \sqrt{\frac{(277.8)}{8x1.145}}$$ D.5

$$= 1.75 m^3 / s$$

D.5

D.2.2 Pressure rise

Due to the fact that the diameter of the casing changes from the inlet to the outlet of the fan, the calculation of fan static pressure rise was not convenient and therefore the fan total pressure rise was calculated. According to BS 848, only the axial component of the flow is added to the static component of the flow and the whirl discarded as it is deemed useless. Equation D.6 expresses this quantity as the difference between the total pressure behind the fan (station 6) and the total pressure before the fan (station 2). All pressures are relative to atmosphere.

$$P_{ft} = P_{t6} - P_{t2} \qquad\qquad \text{D.6}$$

The total pressure is the sum of the static and dynamic pressures.

$$P_{t2} = P_2 + \frac{8\rho Q^2}{\pi^2 D_1^4} \qquad\qquad \text{D.7}$$

$$= -330.2 + \frac{8x1.145x1.75^2}{\pi^2 x0.315^4}$$

$$= -57.0 Pa \quad (\text{relative to atmosphere})$$

$$P_{t6} = 59.1 Pa$$

From equation D.7:

$$P_{ft} = 59.1 - (-57.0)$$

$$= 116.1 Pa$$

D.2.3 Absorbed power

The power absorbed by the fan is the product of the measured torque and the rotational speed as shown in equation D.9.

$$W = Tn \qquad\qquad \text{D.8}$$

$$= 5.0 \left(\frac{960.2\pi}{60} \right)$$

$$= 502.7 W$$

D.2.4 Efficiency

The total to total efficiency is the ratio of the total power delivered to the air and the power delivered to the fan by the electric motor.

$$\eta_{TT} = \frac{P_{ft}Q}{W}$$

D.9

$$= \frac{(116.1)(1.75)}{502.65}$$

$$= 40.5\%$$

D.3   Probe calculations

D.3.1   Pitch and yaw calculation

The five hole probe has a centre hole surrounded by four holes that are drilled at an angle to the axis of the probe. This axis coincides with the centre line of the centre hole.
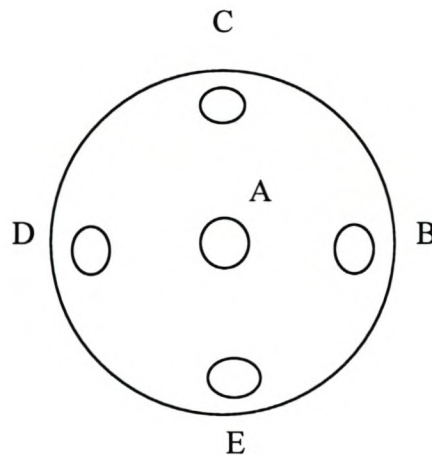
Figure D.1: Orientation and naming of the five holes of the probe.

The five hole probe was used to measure the flow field at the exit of the rotor at two different flow rates of the fan. A sample calculation is done on the fifth reading of the higher of the two

D.7

flow rates. The resulting millivolt output signal is converted into Pascal as shown in the previous section.

#	h		A		B		C		D		E	
	Meas	Real	mV	Pa	mV	Pa	mV	Pa	mV	Pa	mV	Pa
1	120	0	-86	-86.52	-80	-81.95	-97	-94.34	-96	-99.98	-79	-75.19
2	100	20	280	280.99	131	145.29	160	154.77	-49	-50.77	-55	-52.49
3	91	29	250	250.87	121	134.52	132	127.63	-42	-43.44	-45	-43.03
4	80	40	206	206.68	94	105.44	126	121.81	-45	-46.58	-46	-43.98
5	70	50	153	153.47	57	65.59	55	52.99	-48	-49.72	-29	-27.90
6	60	60	115	115.31	40	47.29	40	38.45	-40	-41.35	-20	-19.38
7	50	70	70	70.12	5	9.59	-22	-21.64	-47	-48.68	0	-0.47
8	35	85	30	29.96	-10	-6.56	-50	-48.79	-53	-54.96	20	18.45
9	21	99	22	21.92	-26	-23.79	-58	-56.54	-50	-51.82	40	37.37
10	4	116	-33	-33.30	-55	-55.03	-81	-78.83	-70	-72.76	54	50.61

Table D.7: Readings taken by five hole probe (Q = 1.83 m³/s).

Calculate the relevant coefficients.

$$Average = \frac{P_B + P_C + P_D + P_E}{4} \qquad \text{D.10}$$

$$= \frac{65.59 + 52.99 - 49.72 - 27.90}{4}$$

$$= 10.24\,Pa$$

$$C_{p,pitch} = \frac{P_D - P_B}{P_A - Average} \qquad \text{D.11}$$

$$= \frac{-49.72 - 65.59}{153.47 - 10.24}$$

$$= -0.805$$

$$C_{p,yaw} = \frac{P_E - P_C}{P_A - Average} \qquad \text{D.12}$$

$$= \frac{-27.90 - 52.99}{153.47 - 10.24}$$

$$= -0.565$$

The pitch and yaw coefficients are now used to find the pitch and yaw angles respectively. Figure D.1 is the calibration map taken from Strohmaier (1997) and shown for convenience.

The calculation of the angles was done with a 2D interpolation scheme in MATLAB, using the calibration map in the form of tabulated values. The exact alogorithm as such is not relevant, only that a 3rd order polinomial was used as the interpolating function. The vertical and horizontal line cross at the point where the pitch and yaw angle can be found.
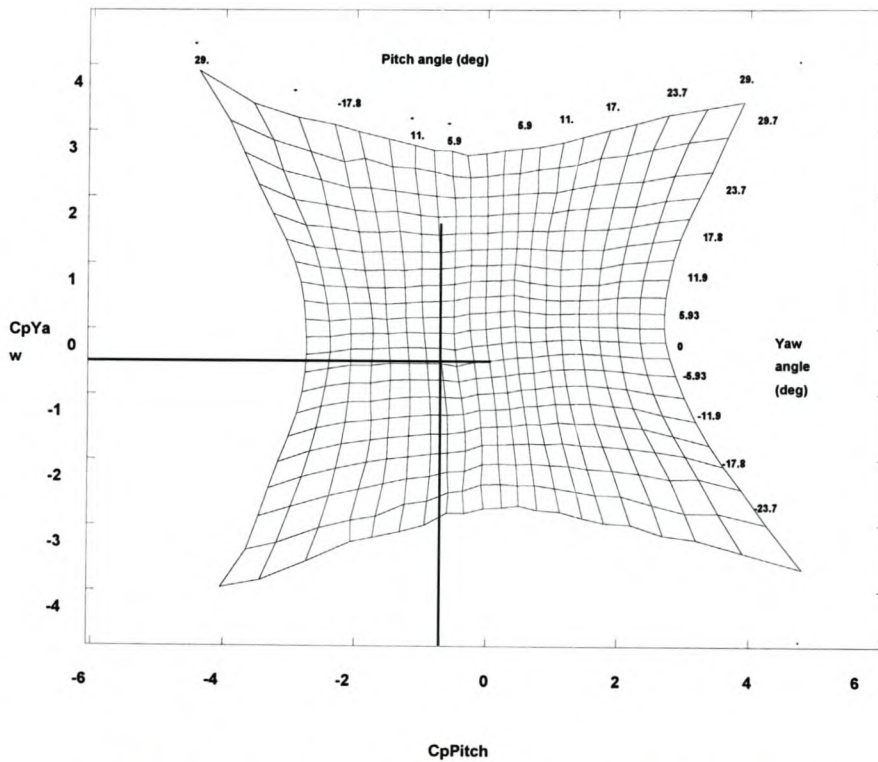
Figure D.2: Calibration map of the University of Stellenbosch five hole probe, taken from Strohmaier (1997)

The solution is:

$$\theta = -10.4°$$

$$\phi = -7.9°$$

From the probe verification tests it was found that the probe has a pitch offset of 7°. Apart from that, the calculated flow angles were relative to the probe, which was set at a nominal yaw angle of 40°. The adjusted values and therefore the real flow angles were:

$$\theta = -10.4° + 7.0° = -3.4°$$

$$\phi = -7.9° + 40° = 31.1°$$

D.9

D.3.2 Pressure and velocity components

Once the orientation of the flow was known, the pitch and yaw angles could be used to find the centre and average coefficient. From these relationships the static and stagnation pressure was solved as explained in Strohmaier (1997).

$$P_{stag} = 204.7 \text{ Pa}$$

$$P_{stat} = -70.3 \text{ Pa}$$

Using a simple Bernoulli relationship, the absolute velocity could be found and subsequently the velocity components.

$$V = 21.8 \text{ m/s}$$

$$V_u = 11.6 \text{ m/s}$$

$$V_r = 1.1 \text{ m/s}$$

$$V_m = 18.4 \text{ m/s}$$

The result was verified by calculating the absolute value of the resulting vector of the velocity components and comparing it with the originally calculated absolute velocity.

$$R = \sqrt{\left(V_u^2 + V_r^2 + V_m^2\right)} \qquad\qquad \text{D.13}$$

$$= \sqrt{\left(11.6^2 + 1.1^2 + 18.4^2\right)}$$

$$= 21.8 m/s = V$$

D.3.3 Absolute and relative flow angles

Once the velocity components were known, the absolute and relative flow angles for the exit follow from simple geometry.

$$\alpha = \cos^{-1}\left(\frac{V_m}{V}\right)$$

$$= \cos^{-1}\left(\frac{18.41}{21.77}\right) \qquad\qquad \text{D.14}$$

$$= 32.3°$$

$$\beta_2 = \tan^{-1}\left[\frac{\omega r_2 - V_u}{V_m}\right]$$

$$= \tan^{-1}\left[\frac{100.53x0.307 - 11.617}{18.41}\right]$$

D.15

$$= 46.3°$$

D.3.4 Specific work

The total specific work is derived from equation D.16.

$$\psi = \frac{\Delta h_0}{U_2^2}$$

D.16

$$= \frac{\left(\Delta P_{stag}/\rho\right)}{U_2^2}$$

$$= \frac{\left(194.1/1.161\right)}{31.44^2}$$

$$= 0.169$$

Soundranayagam et al. (1996) split the Euler turbomachinery term into its two parts and derived a non-dimensional form of the Coriolis term as shown in D.17.

$$\psi_{Cor} = 1 - \left(\frac{r_1}{r_2}\right)^2$$

D.17

$$= 1 - \left(\frac{0.258}{0.313}\right)^2$$

$$= 0.319$$

The aerodynamic specific work is then just the difference between the two.

$$\psi_{Aero} = \psi - \psi_{Cor} = -0.170$$

D.18

D.11

APPENDIX E

THE LEWIS METHOD

During the closing stages of this project, the author found a book by Lewis (1996) on general turbomachinery topics. The book contained a lot of work published by Lewis on a number of topics, including a chapter on mixed flow fan design. Although the timing of this discovery was unfortunate, it was useful to relate this to the rest of the thesis. Lewis presents a balanced approach to the problem that addresses most aspects of the design process and in some cases even work of fundamental importance. Appendix E aims to give an overview of the Lewis methology and presents a few ideas of how to implement them in a design process.

E.1   An overview of the Lewis approach

Lewis derived the Euler turbomachinery equation and, like his predecessors, split it into aerodynamic and Coriolis work terms. He did this not only to illustrate the working of MFFs, but also to define certain geometrical and aerodynamic limits. These limits will be discussed in more detail later in this section. In his design methology, he followed a classical dimensional analysis approach by anticipating the variables that would influence the machine's performance in general, from which he was able to generate a number of non-dimensional parameters (listed in table E.1) that determined the total-to-total efficiency. After some manipulation the following relationship was derived:

$$\eta_{TT} = 1 - f(\phi, \psi, r_2/r_1, A_2/A_1).\zeta \qquad\qquad \text{E.1}$$

This implies that the efficiency of the machine is a function of the profile loss coefficient and some weighting function f. The value of f is more sensitive to initial design parameters than the profile loss coefficient and subsequently has a more pronounced influence on the total efficiency. Therefore, as a first order approximation it is only necessary to minimise f in order to maximise the efficiency. An added advantage is that f is only a function of the duty and geometry and not influenced by the blade shape.

E.1

ϕ	$\dfrac{V_{m2}}{U_2}$	Flow coefficient
ψ	$\dfrac{\Delta h_0}{U_2^2}$	Head coefficient
RR	$r_2 \big/ r_1$	Annulus radius ratio
AR	$A_2 \big/ A_1$	Annulus area ratio
ζ	$\dfrac{(\Delta p_{0R})_{loss}}{\frac{1}{2}\rho w_\infty^2}$	Rotor loss coefficient
Re_2	$\dfrac{2r_2 U_2}{v}$	Machine Reynolds number

Table E.1: Definitions of the non-dimensional quantities influencing total-to-total efficiency. (Lewis, 1996)

Lewis chose to express the velocity triangle relationships as a function of these non-dimensional parameters, allowing him to avoid the difficult issue of geometrical design during the preliminary evaluation, as well as to reduce the number of variables that influenced the result. Despite this simplification, it is still difficult to decide on the correct values to satisfy the design problem. To overcome this, Lewis correctly postulated that the total specific work was the sum of two terms. Namely, the aerodynamic and Coriolis specific work terms, as given by equation E.2. The Coriolis term is derived from the Euler turbomachinery equation and is given in equation E.3.

$$\psi = \psi_{Aero.} + \psi_{Cor.} \qquad\qquad \text{E.2}$$

$$\psi_{Cor.} = 1 - \left(\frac{r_1}{r_2}\right)^2 \qquad\qquad \text{E.3}$$

$$\psi_{Aero} = \psi - 1 + \left(\frac{r_1}{r_2}\right)^2 \qquad\qquad \text{E.4}$$

Now substitute equation E.3 into equation E.2 and re-arrange to find equation E.4. Therefore, for a certain total specific work, a large radius ratio would lead to a large Coriolis specific work term that could require negative aerodynamic specific work. From this it was possible to limit the radius ratio in order to ensure positive aerodynamic specific work.

E.2

Limit 1: Positive aerodynamic work

$$\frac{r_2}{r_1} < \frac{1}{\sqrt{1-\psi}}$$
        E.5

Expressing the deflection of the flow through the rotor in terms of these non-dimensional parameters and solving to find the largest radius ratio that ensures a positive value derived the second limit.

Limit 2: Positive deflection

$$\frac{r_2}{r_1} < \frac{A_1}{A_2}\left(\frac{1}{1-\psi}\right)$$
        E.6

These limits are extremely useful because they give the designer some boundaries within which to design the MFF. It is especially important during the initial stages of the design to get some overall idea of the geometry and this can now be done without simulation or a large number of calculations.

The next step in the Lewis method was to transform rectangular cascade data onto a conical plane. The author also supplied an algorithm to implement these transformations. He proceeded to discuss the use of slip correlations in the design of MFFs, but failed to mention anything about deviation.
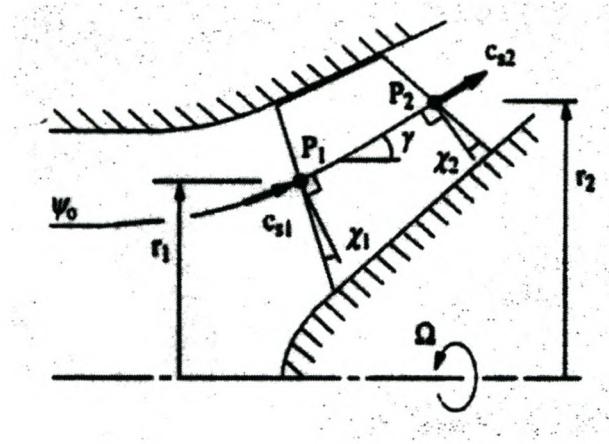
E.2   Implementation of these principles in the design process

Although the Lewis method was not implemented in this project, some aspects of the approach that were lacking previously will be discussed. A useful starting point is the Lewis equation to predict the total-to-total efficiency as seen in equation E.1. Equation E.7 defines the function f as given by Lewis and it is clear that for a given head and flow coefficient that f is only a function of area ratio (AR) and radius ratio (RR).

$$f = \frac{1}{8\psi}\left\{\phi^2\left(1+\frac{A_2}{A_1}\right)^2 + \left(\frac{r_1}{r_2}+1-\psi\right)^2\right\}$$
        E.7

By making some assumptions and through a bit of manipulation, this equation can be used to good effect. Firstly, a few derivations will follow, after which their implementation will be discussed. Figure E.1 describes the meridional annulus geometry from which an expression for AR can be derived as shown in equation E.8.

<div align="center">E.3</div>

$$\frac{A_2}{A_1} = \left(\frac{r_{t1}^2 - r_{h1}^2}{r_{t2}^2 - r_{h2}^2}\right)\left(\frac{\cos(\chi_2)}{\cos(\chi_1)}\right) \qquad \text{E.8}$$

Figure E.1: Meridional annulus geometry. (Lewis, 1996).

Express r_{hi} (the radius of a general point on the hub section of the blade) at both the leading and trailing edges in terms of r_{ti} (the radius of a general point on the tip section of the blade) to find:

$$\frac{A_2}{A_1} = \frac{\cos(\chi_2 + \gamma)}{\cos(\chi_1 + \gamma)}\left[\frac{\cos(\chi_1)}{\cos(\chi_2)}\right]^2 \left[\frac{2r_{t2} + h\dfrac{\cos(\chi_2 + \gamma)}{\cos(\chi_2)}}{2r_{t1} + h\dfrac{\cos(\chi_1 + \gamma)}{\cos(\chi_1)}}\right] \qquad \text{E.9}$$

The radius of any point at the tip, r_{ti}, can be related to r_1 as shown in figure E.1.

$$r_{ti} = r_i + \frac{h}{2}\cos(\gamma) \qquad \text{E.10}$$

$$= RR.r_1 + \frac{h}{2}\cos(\gamma) \quad \text{if } i = 2$$

$$= r_1 + \frac{h}{2}\cos(\gamma) \qquad \text{if } i = 1$$

Substitute equation E.10 into E.9 and simplify to find equation E.11.

E.4

The Lewis Method

$$\frac{A_2}{A_1} = \frac{\cos(\chi_2 + \gamma)}{\cos(\chi_1 + \gamma)} \left[\frac{\cos(\chi_1)}{\cos(\chi_2)}\right]^2 \left[\frac{2RRr_1 + h\left[\cos(\gamma) + \frac{\cos(\chi_2 + \gamma)}{\cos(\chi_2)}\right]}{2r_1 + h\left[\cos(\gamma) + \frac{\cos(\chi_1 + \gamma)}{\cos(\chi_1)}\right]}\right] \quad \text{E.11}$$

Substituting equation E.11 into equation E.7, with the values of ψ and ϕ known, f can be expressed as a function of AR and RR. One way of visualising this is through a contour plot as shown in figure E.2. This plot on its own is of no use, as the designer does not have an idea of the allowable area. Fortunately, there is a unique relationship between RR and AR as described in equation E.11, based on the assumed geometry of the fan. Superimposing this function on figure E.2 results in a line along which a solution may be sought. The relevant one is the optimum solution.
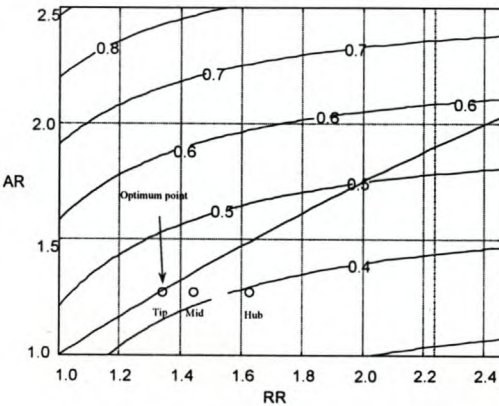
Figure E.2: Contour plot of the weighting function f with the optimum solution shown for $\psi = 0.8$ and $\phi = 0.6$.
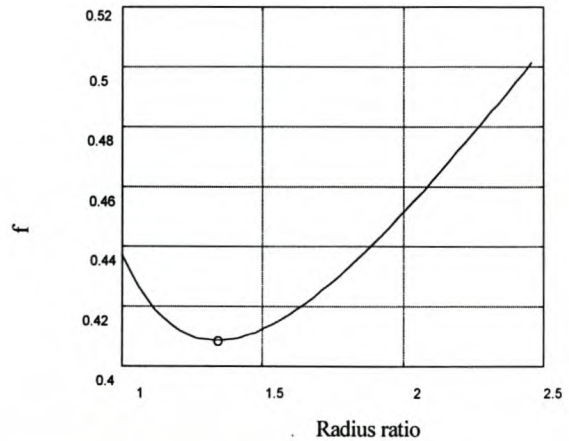
Figure E.3: The weighting function f along the line AR = AR(RR) as shown in Figure E.2.

In 3D, the value of f is described by a surface. Using the function AR = f(RR) as derived in equation E.11, it is possible to find the projection of this function as it cuts the surface. This projection is shown in Figure E.3. The minimum was found using a procedure, written in MATLAB by the author, for given values of χ_1 and χ_2.

E.5

E.3   Conclusion

The method presented by Lewis, although not complete, is based on fundamental principles that form a good basis for any design procedure. The most useful in the opinion of this author is the weighting function f. Lewis does, however, present some theory later in his book that enables the designer, through the use of numeric simulation, to predict the profile loss coefficient.

APPENDIX F

DERIVATION OF TWO-TERM EULER TURBOMACHINERY EQUATION

As a prelude to the derivation of the Euler two-term equation, two concepts have to be discussed: Coriolis work and blade-to-blade circulation.

Coriolis work[1]

In order to assess the significance of Coriolis work in a fluid field, the forces on a fluid particle as it passes through the mixed flow rotor were investigated. When viewed from a non-rotating point of reference, this path will be a spiral through the rotor, which, in general, will incorporate a change in radius. This change in radius of the fluid in the rotating field results in a Coriolis force being exerted on fluid:

$$F_{Coriolis} = 2m\frac{dr}{dt}\omega \qquad \text{F.1}$$

The subsequent shaft power is the product of the Coriolis force and the tangential velocity:

$$\frac{dW_{Coriolis}}{dt} = 2m\frac{dr}{dt}\omega.\omega r \qquad \text{F.2}$$

The specific work done on the fluid particles is found by integrating from r_1 to r_2:

$$\overline{W}_{Coriolis} = \frac{W_{Coriolis}}{m} = 2\omega^2\int_{r_1}^{r_2} r\,dr = \omega^2\left(r_2^2 - r_1^2\right) \qquad \text{F.3}$$

Circulation

Blade-to-blade circulation in a relative flow field, Γ, is defined as (Sayers, 1990):

$$\Gamma = \oint W ds = s_2 W_{u2} - s_1 W_{u1} \qquad \text{F.4}$$

The symbol, s, is the pitch of the rotor and is defined as:

$$s = \frac{2\pi r}{Z} \qquad \text{F.5}$$

_____

[1] This section, including equations F.1 to F3 was taken from Lewis (1996).

where r is radial distance from the rotor axis to the blade element. Substitute equation F.5 into F.4 to find:

$$\Gamma = \frac{2\pi}{Z}\left(r_2 W_{u2} - r_1 W_{u1}\right) \qquad \text{F.6}$$

It is useful to write equation F.6 in another form for later use:

$$\frac{\omega \Gamma Z}{2\pi} = \omega\left(r_2 W_{u2} - r_1 W_{u1}\right) \qquad \text{F.7}$$

Derivation of the two-term Euler equation.

The specific work rate of a turbomachine is described by the so-called Euler equation given in equation 3.3 and repeated here for convenience.

$$\overline{W} = W\,/\,\dot{m} = \omega\left(r_2 V_{u2} - r_1 V_{u1}\right) \qquad \text{F.8}$$

Equation F.8 can be written in an equivalent two-term form, the derivation of which requires that the swirl be expressed in terms of the tangential component of the relative velocity, W_u, and the tangential velocity, U, by noting that $U = \omega r$. The positive direction for the tangential components of the absolute and relative velocities is chosen in the direction of the tangential velocity.

$$V_u = W_u + U \qquad \text{F.9}$$

Substitute equation F.9 into equation F.8 and simplify.

$$\overline{W} = \omega\left[r_2\left(U_2 + W_{u2}\right) - r_1\left(U_1 + W_{u1}\right)\right] \qquad \text{F.10}$$

$$= \omega^2\left(r_2^2 - r_1^2\right) + \omega\left(r_2 W_{u2} - r_1 W_{u1}\right) \qquad \text{F.11}$$

From equation F.7 the second term on the right hand side of equation F.11 is expressed in terms of the blade-to-blade circulation.

$$\overline{W} = \omega^2\left(r_2^2 - r_1^2\right) + \frac{\omega \Gamma Z}{2\pi} \qquad \text{F.12}$$

From the derivation it is clear that the first term on the right hand side of equation F.12 represents the Coriolis specific work, while the second term on the right hand side is work done due to blade action and is therefore aptly called the aerodynamic specific work.

F.2

APPENDIX G

A COMPARISON OF THE CONFORMAL TRANSFORMATION TO THE METHOD USED BY LEWIS

A book, written by Lewis (1996), was discovered at the closing stages of this project. Among other things, the book contained a method of conformally transforming a rectangular cascade to a conical one. The aim of Appendix G is to relate the transformation proposed by the author in Chapter 3 to the one presented by Lewis (1996).

Lewis' transformation

Lewis formulated a transformation from a mixed flow (figure G.1) to a straight, rectangular cascade (figure G.2). The transformation was conformal, which means that it had two properties: the corner angles stay the same (i.e. the grid lines cross perpendicularly in both coordinate systems) and equivalent sides (such as ds and dξ or rdθ and dη) stay in a fixed ratio.
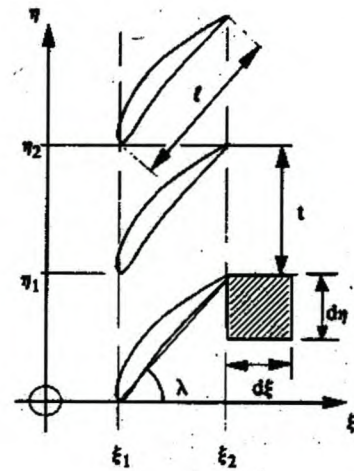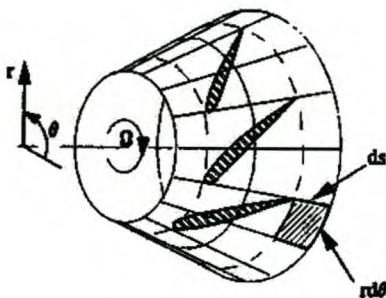
Figure G.1: Mixed flow cascade (Lewis, 1996)   **Figure G.2: Straight, rectangular cascade (Lewis, 1996)**

From the second requirement of conformality listed above, Lewis derived the following general relationship:

$$\frac{d\xi}{d\eta} = \frac{ds}{rd\theta}$$

G.1

G.1

Use equation G.1 to derive the following equations:

$$d\xi = \frac{ds}{r} = \frac{dr}{r \sin \gamma} \qquad \text{where } ds = \frac{dr}{\sin \gamma} \qquad \text{G.2}$$

$$d\eta = d\theta \qquad \text{G.3}$$

Integrating equations G.2 and G.3 for a constant cone angle (i.e. $\gamma \neq f(r)$).

$$\int_{\xi_1}^{\xi} d\xi = \int_{r_1}^{r} \frac{1}{\sin(\gamma)} \frac{dr}{r}$$

$$\xi - \xi_1 = \frac{1}{\sin(\gamma)} \ln\left(\frac{r}{r_1}\right) \qquad \text{G.4}$$

$$\int_{\eta_1}^{\eta} d\eta = \int_{\theta_1}^{\theta} d\theta$$

$$\eta - \eta_1 = \theta - \theta_1 \qquad \text{G.5}$$

An intelligent choice of coordinate systems for both the mixed flow and rectangular cascades, such that $\xi_1 = 0$ where $r = r_1$ and $\eta_1 = 0$ where $\theta_1 = 0$, simplifies equations G.4 and G.5 to:

$$\xi = \frac{1}{\sin(\gamma)} \ln\left(\frac{r}{r_1}\right) \qquad \text{G.6}$$

$$\eta = \theta \qquad \text{G.7}$$

The reverse transformation follows from simple algebra:

$$r = r_1 . e^{\xi \sin(\gamma)} \qquad \text{G.8}$$

$$\theta = \eta \qquad \text{G.9}$$

In Chapter 3, the author made a transformation from a rectangular cascade to a mixed flow cascade with the difference that the latter was a flat development of the cascade shown in figure G.1. The purpose of this appendix is to compare the transformation done by Lewis to the transformation independently derived by the author. For this comparison to be useful, a transformation is sought from the 3D to the 2D mixed flow cascades. Once this is done, the Lewis transformation is also from the 2D rectangular cascade to the 2D mixed flow cascade.
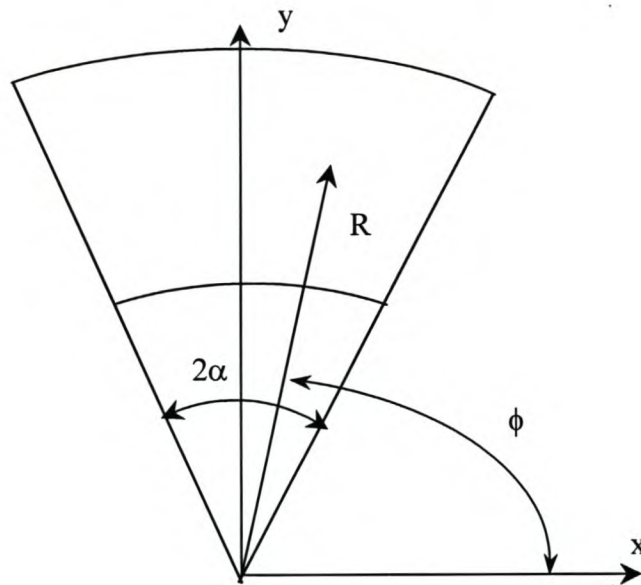
Figure G.3: 2-D mixed flow cascade

Figure G.3 shows the developed mixed flow cone. The angle is ϕ the so-called sweep angle and is the angle between the radius R and the positive x-axis. To transform from the 3D to the 2D mixed flow cascade, the relationship between the angle ϕ and the angle θ that is shown in figure G.1 has to be found. This relationship is linear and therefore requires two known points to solve for the two unknown coefficients. The two points (ϕ,θ) used are: $(0, \pi/2-\alpha)$ and $(2\pi, \pi/2+\alpha)$, resulting in equation G.11:

$$\phi = \frac{\alpha}{\pi}\theta + \frac{\pi}{2} - \alpha \qquad\qquad\qquad \text{G.11}$$

Express x and y in terms of R and ϕ.

$$x = R\cos\phi \qquad\qquad\qquad \text{G.12}$$

$$y = R\sin\phi \qquad\qquad\qquad \text{G.13}$$

If figure G.3 is just the development of the cone shown in figure G.1, a circle perpendicular to the axis of the cone in figure G.1 would result in a corresponding arc on the surface shown in figure G.3. This arc will have a constant radius and will have the same length as the circle drawn on the cone. Using this fact and equation 3.33, the relationship between r and R can be derived.

G.3

$$R = \frac{\pi}{\alpha} r = \frac{r}{\sin \gamma} \qquad \text{G.14}$$

Substitute equations G8, G.11 and G.14 into equations G.12 and G.13 and simplify. The resulting equations represent the equivalent of Lewis' transformation from a rectangular to a 2D mixed flow cascade.

$$x = A.e^{\xi}.\cos(\delta + \Delta) \qquad \text{G.15}$$

$$y = A.e^{\xi}.\sin(\delta + \Delta) \qquad \text{G.16}$$

$$\text{where } \delta = \frac{\alpha}{\pi}\eta \;,\; \Delta = \frac{\pi}{2} - \alpha \text{ and } A = \frac{r_1.e^{\sin \gamma}}{\sin \gamma}$$

As mentioned in Chapter 3, the coefficient in both equations (in this case, A) is simply a scaling factor – it does not influence the transformation, but depends on the chosen point of reference and the cone angle. In essence the shape of the transformed object will remain the same and its size vary in accordance to A. Another parameter that does not change the transformation is, Δ. From the derivation, it is clear that Δ is a function of the position of the origin of the set of axis. It is therefore possible to position the axes in such a way that Δ reduces to zero.

Du Toit's transformation

The transformation used in this project (Chapter 3) transforms a rectangular cascade to a 2D mixed flow one, i.e. from the geometry shown in figure G.2 to the geometry shown in figure G.3. Equations 3.34 and 3.35 are repeated for convenience. Note that a prime will be used to distinguish the Du Toit from the Lewis equations.

$$x' = \text{Re}^{\lambda_{cone}\xi} \cos(\lambda_{cone}\eta') \qquad \text{G.17}$$

$$y' = \text{Re}^{\lambda_{cone}\xi} \sin(\lambda_{cone}\eta') \qquad \text{G.18}$$

These equations can also be written in the form shown in equations G.15 and G.16.

$$x' = A' e^{\xi} \cos(\delta' + \Delta') \qquad \text{G.19}$$

$$y' = A' e^{\xi} \sin(\delta' + \Delta') \qquad \text{G.20}$$

G.4

where $\delta' = \dfrac{2\alpha}{Zt}\eta'$, $\Delta' = 0$ and $A' = R.e^{\lambda_{cone}}$

Select a coordinate system and a reference characteristic length for the Lewis transformation such that $\Delta = 0$ ($\Delta = \Delta'$) and $A = A'$. Equations G.15 and G.16 would then be similar to equations G.19 and G.20 in all respects but for the arguments, δ and δ'. Section 3.1.5 in Chapter 3 explains the significance of δ' (the argument in the Du Toit transformation) as the so-called sweep angle. It is also shown that this term varies between nil and 2α. In the Lewis transformation, η is an angle between nil and 2π (see equation G.7). From equations G.15 and G.16 it follows that δ is an angle between nil and 2α, which would correspond with δ' as these terms represent in both cases the sweep angle as defined in Chapter 3. The Du Toit and Lewis transformations are thus equivalent.